Analysis of fluid dynamics and heat transfer in pillow-plate heat exchangers

Zur Erlangung des akademischen Grades
DOKTOR DER INGENIEURWISSENSCHAFTEN (Dr.-Ing.)
von der Fakultät fur Maschinenbau
der Universität Paderborn

genehmigte
DISSERTATION

von
Dipl.-Ing. Mark Piper
aus Limassol (Zypern)

Tag des Kolloquiums: 07.09.2018
Referent: Prof. Dr.-Ing. habil. Eugeny Kenig
Korreferentin: Prof. Dr. Sc. Tatiana Gambaryan-Roisman

In loving memory of my father, Rolf Werner Piper.

Acknowledgment

The present work resulted in my time as a research assistant at the Chair of Fluid Process Engineering at Paderborn University from 2011 to 2016.

First and foremost, I want express my deep gratitude to my doctoral supervisor, Prof. Eugeny Kenig, for his invaluable support. He gave me the freedom to pursue my research interests with full enthusiasm. Moreover, he was always open and supportive to my desire to develop new ”small” experimental facilities for my research. I always enjoyed our discussions in the car, coming back from a conference, where we started with small talk and ended up with fascinating philosophical concepts.

I also sincerely thank Prof. Tatiana Gambaryan-Roisman for taking up the position of the second reviewer, Prof. Jadran Vrabec and Prof. Elmar Moritzer for their participation in the examination board.

Furthermore, I want to thank Astrid Bongard from the secretary’s office, who assisted me in numerous bureaucratic matters. I thank all my former colleagues from the Chair of Fluid Process Engineering in Paderborn, for their support and friendship. Special thanks go to Anna Chasanis, Anna Große-Daldrup, Nicole Hüser and Ömer Yildirim for their warm welcome when I started my work at the chair, and for the many funny moments, which enlivened the workplace. I also want to thank Prof. Reiner Numrich for the interesting and amusing discussions concerning heat exchanger design in practise. In particular, I want to thank my very good friend and former colleague, Roland Engberg, for his continuous support and for our many fascinating and fruitful discussions about fluid mechanics, music and the meaning of life over a bottle of single malt whisky.

Moreover, I want to thank Alexander Olenberg, Alexander Zibart and Christian Wecker for their support in the scope of their Bachelor/Master thesis. The close work led to friendships and later even to the business partnership with Alexander Olenberg and Alexander Zibart in the scope of our entrepreneurial venture “Flocess”.

I also thank the technical assistants, Franz Kapla and Mirko Fölling, for their continuous support in the development of the numerous ”small” experimental set-ups, constructed during my time at the chair.

Finally, I want to thank all my family and my friends, especially my mother Mary Piper, for her enduring support throughout difficult times in the past years. She never gave up on me. She was always there like a lioness. I want to thank my daughter, Elli Piper, who gives me strength and cheers me-up with her irresistible sweetness, and my wife, Daniela Piper, who supported and kept pushing me to finally finish writing this thesis.

Mark Piper
Paderborn, September 2018

Kurzfassung

Kissenplatten-Wärmeübertrager (KPWÜ) bestehen aus einem Paket von Kissenplatten, welche durch ihre wellige “kissenförmige” Oberfläche und vollständig verschweißte Konstruktion gekennzeichnet sind. Sie stellen eine vielversprechende Alternative zu konventionellen Apparaten für die Prozessindustrie dar, jedoch verhindert der Mangel an veröffentlichten Auslegungsgrundlagen ihre verbreitete Anwendung. Das Ziel dieser Arbeit ist es daher, diesen “Engpass” durch die Bereitstellung neuer Dimensionierungsgleichungen für die thermohydraulische Auslegung von KPWÜ zu überwinden.

Insbesondere werden die Fluiddynamik und der Wärmeübergang in KPWÜ im Detail mittels Computational Fluid Dynamics (CFD)-Methoden untersucht. Die komplexe Geometrie der Kissenplattenkanäle wird mit Hilfe von Verformungssimulationen, welche auf der Finite-Elemente-Analyse (FEA) basieren, erzeugt. Mit dieser Methode ist es möglich die reale wellenförmige Oberfläche von Kissenplatten genau nachzubilden. Im nächsten Schritt wird eine umfangreiche CFD-Studie zur Fluiddynamik und Wärmeübertragung in den inneren sowie in den äußeren Kanälen von KPWÜ durchgeführt. Die CFD Simulationen werden mit Hilfe von drei Versuchsanlagen, zwei für die Untersuchung der Strömung im inneren Kanal und eine für die Untersuchung der Strömung im äußeren Kanal, validiert. Die validierten numerischen Ergebnisse werden verwendet, um Auslegungsgleichungen für den Druckverlustbeiwert sowie für die Nusselt-Zahl für erzwungene turbulente Strömung in KWPÜ zu entwickeln.

Abstract

Pillow-plate heat exchangers (PPHE) comprise a stack of pillow plates characterized by their wavy “pillow-shaped” surface and fully welded construction. They represent a promising alternative to conventional equipment for the process industry; however, the lack of published design methods hinders their widespread application. This work aims at overcoming this “bottleneck” by providing new equations for the thermo-hydraulic design of PPHE.

In particular, fluid dynamics and heat transfer in PPHE is investigated in detail using Computational Fluid Dynamics (CFD) methods. The complex geometry of the pillow-plate channels is generated using forming simulations based on Finite Element Analysis (FEA). This method provides an accurate reconstruction of the real wavy surface of pillow plates. In the next step, a comprehensive CFD-study of fluid dynamics and heat transfer in the inner and outer channels of PPHE is performed. The CFD simulations are validated using three experimental facilities, two for the investigation of flow in the inner channel and one for the investigation of flow in the outer channel. The validated numerical results are then used to develop design methods for pressure loss and heat transfer for turbulent forced convection in PPHE.

List of Publications

Results of this work have partly been published in peer-reviewed international journals and proceedings of international conferences, listed below.

Journal articles

M. Piper, A. Olenberg, J.M. Tran, R. Goedecke, S. Scholl, E.Y. Kenig, Bestimmung charakteristischer Geomtrieparameter von Thermoblech-Wärmeübertragern, Chem. Ing. Tech. 86 (2014) 1214-1222.

M. Piper, J.M. Tran, E.Y. Kenig, Untersuchung der Fluiddynamik und des Wärmeübergangs bei einphasiger Strömung im welligen Spalt zwischen Thermoblechen, Chem. Ing. Tech. 87 (2015) 216-225.

M. Piper, C. Wecker, A. Olenberg, J.M. Tran, E.Y. Kenig, An experimental analysis of the topology and dynamics of a falling liquid film over the wavy surface of a vertical pillow plate, Chem. Eng. Sci. 130 (2015) 129-134.

M. Piper, A. Olenberg, J.M. Tran, E.Y. Kenig, Determination of the geometric design parameters of pillow-plate heat exchangers, Appl. Therm. Eng. 91 (2015) 1168-1175.

M. Piper, A. Zibart, J.M. Tran, E.Y. Kenig, Numerical investigation of turbulent forced convection heat transfer in pillow plates, Int. J. Heat Mass Transfer 94 (2016) 516-527.

M. Piper, A. Zibart, E.Y. Kenig, New design equations for turbulent forced convection heat transfer and pressure loss in pillow-plate channels, Int. J. Therm Sci 120 (2017) 459-468.

J. M. Tran, M. Piper, E.Y. Kenig, Experimental investigation of convective heat transfer and pressure drop in pillow plates under single-phase through-flow condition, Chem. Ing. Tech. 87 (2015) 226-234.

J. M. Tran, S. Sommerfeld, M. Piper, E.Y. Kenig, Investigation of pillow-plate condensers for the application in distillation columns, Chem. Eng. Res. Des. 99 (2015) 67-74.

Conference proceedings

M. Piper, A. Zibart, J.M. Tran, E.Y. Kenig, A numerical study on turbulent single-phase flow and heat transfer in pillow plates, in: Proceedings of the 15th International Heat Transfer Conference, Kyoto, Japan, 2014.

M. Piper, J.M. Tran, E.Y. Kenig, A CFD-study of the thermo-hydraulic characteristics of pillow-plate heat exchangers, in: Proc. ASME 2016 Summer Heat Transfer Conference, Washington DC, USA, 2016.

Oral presentations

M. Piper, J.M. Tran, E.Y. Kenig, Untersuchung von Druckverlust und Wärmeübergang der einphasigen Strömung im welligen Kanal zwischen Thermoblechen, ProcessNet-Jahrestreffen der Fachgemeinschaft Fluiddynamik und Trenntechnik, Würzburg, 2013.

M. Piper, A. Zibart, J.M. Tran, E.Y. Kenig, Numerische Untersuchung der Strömungs- und Wärmeübergangscharakteristik von Thermoblechen, ProcessNet-Jahrestagung und 31. DECHEMA-Jahrestagung der Biotechnologen, Aachen, 2014.

M. Piper, A. Zibart, J.M. Tran, E.Y. Kenig, A numerical study on turbulent single-phase flow and heat transfer in pillow plates, 15th International Heat Transfer Conference, Kyoto, Japan, 2014.

M. Piper, A. Zibart, J.M. Tran, E.Y. Kenig, Ein strömungsorientierter Dimensionierungsansatz für Thermobleche, ProcessNet-Jahrestreffen der Fachgruppen Wärme- und Stoffübertragung, Leipzig, 2015.

M. Piper, A. Zibart, J.M. Tran, E.Y. Kenig, A design approach for pillow-plate heat exchangers and an analysis of their thermo-hydraulic performance based on numerical results, ACHEMA 2015, Frankfurt am Main, 2015.

M. Piper, J.M. Tran, E.Y. Kenig, A CFD-study of the thermo-hydraulic characteristics of pillow-plate heat exchangers, ASME 2016 Summer Heat Transfer Conference, Washington DC, USA, 2016.

S. Sommerfeld, J.M. Tran, M. Piper, E.Y. Kenig, R. Goedecke, S. Scholl, A. Wetzel, U. Femmer, Experimentelle Untersuchungen von Thermoblech-Wärmeübertragern als Naturumlaufverdampfer und Kondensator im technischen Maßstab,Jahrestreffen der Fachgruppen Mehrphasenströmungen und Wärme- und Stoffübertragung, Fulda, 2014.

J.M. Tran, S. Sommerfeld, M. Piper, E.Y. Kenig, Investigation of pillow-plate condensers for the application in distillation columns, 10th International Conference on Distillation and Absorption 2014, Friedrichshafen, 2014.

J.M. Tran, M. Piper, E.Y. Kenig, Modelling of heat transfer and fluid dynamics in pillow-plate condensers based on experimental investigations, ACHEMA 2015, Frankfurt am Main, 2015.

J.M. Tran, M. Piper, E.Y. Kenig, Experimental Investigation of Heat Transfer and Pressure Drop in Pillow-Plate Condensers, AIChE Spring Meeting 2015, Austin (USA), 2015.

J.M. Tran, S. Sommerfeld, M. Piper, E.Y. Kenig, Experimentelle Untersuchungen zum Kondensationsverhalten von Thermoblech-Wärmeübertragern im Labor- und Technikumsmaßstab, Jahrestreffen der Fachgruppen Extraktion und Fluidverfahrenstechnik, Fulda, 2014.

Posters

M. Piper, A. Olenberg, J.M. Tran, R. Goedecke, S. Scholl, E.Y. Kenig, Bestimmung des hydraulischen Durchmessers für die Auslegung von Thermoblech-Wärmeübertragern, ProcessNet-Jahrestagung 2012, Karlsruhe, 2012.

M. Piper, A. Olenberg, J.M. Tran, R. Goedecke, S. Scholl, E.Y. Kenig, Untersuchung der Fluiddynamik und des Druckverlusts der einphasigen Strömung im welligen Kanal zwischen benachbarten Thermoblechen, ProcessNet-Jahrestreffen der Fachgemeinschaft Wärme- und Stoffübertragung, Baden-Baden, 2013.

M. Piper, A. Zibart, J.M. Tran, E.Y. Kenig, Numerische Untersuchung von Fluiddynamik und Wärmeübergang der einphasigen turbulenten Strömung in Thermoblechen, ProcessNet-Jahrestreffen der Fachgruppen Extraktion und Fluidverfahrenstechnik, Fulda, 2014.

M. Piper, C. Wecker, A. Zibart, E.Y. Kenig, Experimentelle Untersuchung der Strömung in einem transparenten Kissenplattenkanal vom laminaren bis zum turbulenten Zustand, ProcessNet-Jahrestreffen der Fachgruppe Fluidverfahrenstechnik, Köln, 2016.

J.M. Tran, M. Piper, E.Y. Kenig, Innenseitiger Druckverlust und Wärmeübergang in einem einphasig durchströmten Thermoblech, ProcessNet Jahrestagung 2012, Karlsruhe, 2012.

J.M. Tran, M. Piper, E.Y. Kenig, Wärmeübertragung und Fluiddynamik in Thermoblech-Kondensatoren: Modellierung basierend auf experimentellen Untersuchungen, Jahrestreffen der Fachgruppen Membrantechnik und Fluidverfahrenstechnik, Bremen, 2015.

Patents

M. Piper and E.Y. Kenig, inventor; Paderborn University, assignee. Pillow-plate heat exchangers. German patent DE1020160059999A1. 2016 May 18.

Contents

List of Figures

List of Tables

Nomenclature

Latin Symbols

Symbol	Description	Units
A	area	m^2
a, b, c	dimensionless geometrical parameters (Egs. (7.2) - (7.4))	
$\widetilde{a}$	thermal diffusivity	$m^2 s^{-1}$
α, f	empirical coefficients (Eq. (4.25), (4.26) and (4.27))	
b_D	free diagonal distance between welding spots	m
B	total width of a pillow plate	m
C, C_μ	proportionality factors in Eqs. (3.37), (3.38) and (3.54)	
c_p	specific heat capacity	$Jkg^{-1}K^{-1}$
d	diameter	m
$\widetilde{d}$	normal distance to the wall	m
Fr	Froude number	
$\mathbf{g}$	gravitational acceleration vector	ms^{-2}
$\mathbf{g}^*$	dimensionless gravitational acceleration vector	
h	heat transfer coefficient	$Wm^{-2}K^{-1}$
k	turbulent kinetic energy	$m^2 s^{-2}$
$l_{char}, \mathcal{L}$	characteristic length	m
l_R	free longitudinal distance between welding spots	m
L	total length	m
$\mathbf{n}$	unit normal vector	
n_1 to n_7	adjustment parameters in Eqs. (7.1), (7.5) and (7.11)	
Nu	Nusselt number	
p	pressure	Nm^{-2}
$\overline{p}$	time-averaged pressure	Nm^{-2}
p^*	dimensionless pressure	
P	wetted perimeter	m
Pr	Prandtl number	
$\dot{q}$	heat flux	Wm^{-2}

Symbol	Description	Units
$\overline{q}$	time-averaged heat flux	Wm^{-2}
Q	source of Φ (Eq. (3.1))	
$\dot{Q}$	heat transfer rate	W
Re	Reynolds number	
s	welding spot pitch	m
$s(x)$	sine curve function	m
s^*	ratio of arc-length of zone 1 and longitudinal pitch	
$\overline{\mathbf{S}}$	time-averaged strain-rate tensor	s^{-1}
s_r	reduced welding spot pitch	
S_h	volume source in energy equation (Eq. (3.13))	Wm^{-3}
S_φ	volume source of φ (Eq. (3.2))	
t	time	s
T	temperature	K
T^*	dimensionless temperature	
u	velocity	ms^{-1}
U	overall heat transfer coefficient	$Wm^{-2}K^{-1}$
$\mathbf{u}$	velocity vector	ms^{-1}
$\overline{\mathbf{u}}$	time-averaged velocity vector	ms^{-1}
$\lvert\overline{\mathbf{u}}\rvert$	magnitude of time-averaged velocity	ms^{-1}
$\mathbf{u}'$	fluctuation of velocity vector	ms^{-1}
$\mathbf{u}^*$	dimensionless velocity vector	
$\mathcal{U}$	characteristic velocity	ms^{-1}
u_τ	shear stress velocity	ms^{-1}
V	volume of pillow-plate channels	m^3
$\dot{V}$	volumetric flow rate	m^3s^{-1}
$\dot{W}$	pumping power	W
$\tilde{y}$	coordinate normal to the wall	m
$\mathbf{x}$	position vector	m
$\mathbf{x}^*$	dimensionless position vector	
x, y, z	Cartesian coordinates	m
x^+, y^+, z^+	dimensionless wall coordinates of inner layer	

Greek Symbols

Symbol	Description	Units
α	elliptic blending factor in Eq. (3.56)	
β	phase shift of sine curve describing the shape of zone 1	
Γ_φ	diffusion coefficient of φ (Eq. (3.2))	
δ	boundary layer thickness	m
δ_p	thickness of metal sheets	m
δ_P	max. distance between adjacent pillow plates	m
δ_i	inflation height	m
Δp	pressure loss	Nm^{-2}

Symbol	Description	Units
ΔT	temperature difference	K
ε	turbulent dissipation rate	m^2s^{-2}
ϵ	thermo-hydraulic efficiency	
ϵ^*	normalized thermo-hydraulic efficiency	
ζ	friction factor	
ζ_f	Fanning friction factor	
η_w	dimensionless distance to the wall	
Θ^+	dimensionless temperature difference	
κ	Von Kármán constant	
λ	thermal conductivity	$Wm^{-1}K^{-1}$
μ	dynamic viscosity	$kgm^{-1}s^{-1}$
μ_t	turbulent eddy viscosity	$kgm^{-1}s^{-1}$
ν	kinematic viscosity	m^2s^{-1}
ρ	density	kgm^{-3}
$\overline{\tau}$	time-averaged shear stress	Nm^{-2}
$\overline{\tau}^R$	Reynolds stress	Nm^{-2}
τ_w	wall shear stress	Nm^{-2}
$\lvert\tau_{\mathbf{w}}\rvert$	magnitude of wall shear stress	Nm^{-2}
ψ	dimensionless "two-zone" parameter	
φ	random intensive quantity	
$\overline{\varphi}$	time-averaged random intensive quantity	
φ'	fluctuation of random intensive quantity	
ϕ	dimensionless welding spot parameter	
Φ	random extensive quantity	
ψ	dimensionless "two-zone" parameter	
ω	specific dissipation	s^{-1}
$\overline{\mathbf{\Omega}}$	time-averaged rotation rate tensor	s^{-1}

Superscripts and Subscripts

Symbol	Description
0	projection area
∞	value in core flow
A	area
amp	amplitude
B	bulk
C	circular
cf	control face
$char$	characteristic
cs	cross-section
D	drag
δ	thickness of viscous sub-layer
Δ_p	pressure loss (for Darcy friction factor)

Symbol	**Description**
E	elliptic
exp	experiment
f	face
HT	heat transfer
h	hydraulic
$h0$	reference hydraulic
ϑ	temperature
i	inner
i, j, k	indices
L	longitudinal
m	mean
$m0$	reference mean
max	maximum
n	normal
mc	meandering core
min	minimum
n	normalized
o	outer
P	plate
pow	power
PE	periodic element
Q	heat
R	friction
Re	Reynolds
ref	reference
RZ	recirculation zone
SP	welding spot
sim	simulation
sym	symmetry
t	tangential
T	transverse or temperature
tot	total
$tube$	tube
V	volume
Vn	volume normalized
u	velocity
w	wetted or wall
wn	wetted normalized
x, y, z	Cartesian coordinates
$z1$	zone 1
$z2$	zone 2

1 Introduction

Increasing the energy efficiency of production processes in the process industry (energy, chemical, pharmaceutical, steel, etc.) represents one of the key measures to reduce anthropogenic greenhouse gas emissions, especially of carbon dioxide (CO_2). According to a report from the German federal environment agency (www.umweltbundesamt.de), in the year 2014, the energy sector was responsible for about 39% and the industrial sector for about 21% of the total CO_2 emissions in Germany. The total energy demand of the German chemical industry amounted to 185 TWh in 2009, which corresponded to approximately 8% of the national energy consumption and to approximately 30% of the consumption of the manufacturing industry (Fig. 1.1 (right)). An estimated 44% of this demand was related to evaporation processes. Consequently, thermal processes can be considered as the most energy-intensive. Therefore, an increase in heat transfer efficiency in such processes has a high saving potential for energy and resources.

Figure 1.1 shows a photo of a typical chemical production plant. It consists of a number of so-called "unit operations", which represent the building elements of such a plant. These units may be distillation columns, reactors, membrane modules and so on, but most of them are heat exchangers. The latter account for 30 – 60% of all apparatuses in thermal production plants.

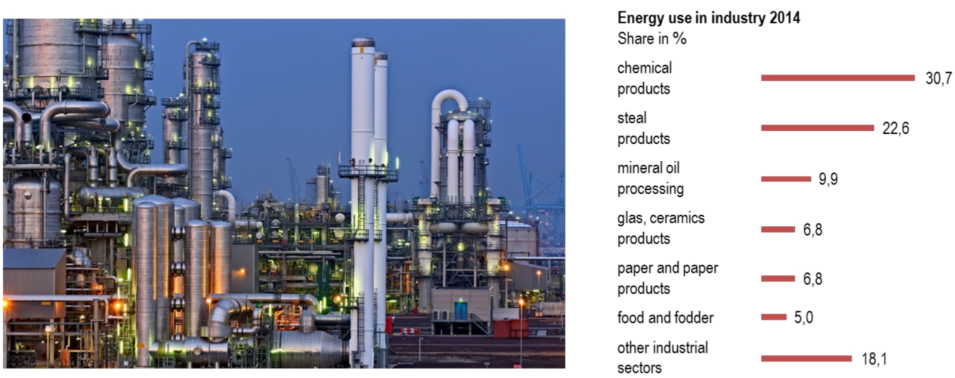

Figure 1.1: Photo of a chemical production plant (photo: www.quora.com/what-jobs-do-chemical-engineers-do, accessed 26.09.2018) and breakdown of energy usage according to the different industry sectors in Germany for the year 2014 (adjusted from [1]).

Consequently, improvement of thermal efficiency through, e.g. innovative equipment designs, offers an enormous potential for increasing the energy efficiency in the process industry.

Many new heat exchanger types have been proposed over the years, whereas pillow-plate heat exchangers (PPHE) represent one of the most promising designs for the future. The problem most new technologies, such as PPHE, face when entering the market is the lack of proven (thermal) design methods as well as reference applications proving their performance. The development of such design methods requires knowledge (data) of fluid flow and heat transfer in the new equipment for a large range of operating conditions and geometrical variations. While such data is commonly obtained by experimental methods, experiments are costly, time consuming and potentially dangerous in cases where measurements must be performed at high temperatures, high pressures or with hazardous media. An alternative to experiments are numerical methods involving Computational Fluid Dynamics (CFD) simulations. CFD is faster, more flexible and cheaper than experiments and provides detailed information on flow fields not easily obtainable experimentally. It is a method that can tackle complex flows in complex geometries, such as in the channels of PPHE. This insight led to the topic of this work, namely, the utilization of CFD methods for the study of fluid dynamics and heat transfer in PPHE, with the aim of developing accurate design methods for this promising equipment.

1.1 Motivation and structure

A major part of this work was performed during the joint project InnovA^2 (www.innova2.de) funded by the German Federal Ministry of Education and Research. It was focused on the promotion of innovative heat exchanger technologies with a high energy saving potential, such as PPHE and finned tubes. The project involved 17 partners, from 5 universities (including Paderborn University) and 12 industrial partners (Bayer AG, Linde AG, Evonik AG and Lanxess AG, just to name a few). The Chair of Fluid Process Engineering at Paderborn University was responsible for the experimental investigation of the thermo-hydraulic characteristics of pillow-plate condensers (used as top condensers in distillation columns). The aim of these studies was the development and dissemination of first design methods for PPHE. As mentioned above, experimental methods are often time consuming, costly and inflexible. Therefore, CFD simulations were used complementary to the experiments to expand the acquired knowledge (from the experiments) over a greater range of operating conditions and geometrical variations.

Since the chapters in this thesis are strongly coupled, it is not recommended to skip sections and start reading somewhere in the middle. The reader is advised to read the thesis from beginning to end. A short overview of the structure of the chapters is given below for the readers convenience.

Chapter 2 presents a literature review on PPHE, which shows the state of the art and the motivation for this work. Background information needed for understanding the CFD methods used in this thesis are shown in Chapter 3.

Since the prerequisite for the realistic description of the fluid dynamics in pillow-plates is an accurate reconstruction of the complex pillow-plate channel, Chapter 4 deals with the generation of the wavy PPHE surface using forming simulations. In Chapter 5, fluid flow and heat transfer in the inner channels of PPHE are investigated for a wide range of geometrical parameters, Reynolds numbers and Prandtl numbers, while the CFD simulations are validated against experiments. In Chapter 6, the fluid dynamics and heat transfer in the outer channels of PPHE are discussed, while again validating the CFD simulations against experiments. The results gathered in Chapters 5 and 6 are used in Chapter 7 to develop design equations for the determination of pressure loss and heat transfer coefficients in PPHE.

2 State of the art

This chapter provides an outline of the state of the art in heat transfer equipment. This is followed by the introduction of pillow-plate heat exchanger (PPHE), including a short literature review concerning the most important findings preceding this work.

2.1 Heat exchanger construction

Heat exchangers form the basis of most thermal process; they are encountered in many different industry sectors, such as, energy, chemical, pharmaceutical, food, transportation etc. Many different types of heat exchangers are available on the market. Some of them are summarized in Fig. 2.1 according to their construction.

The most common designs found in process industry are: tubular and plate-type heat exchangers. From the tubular-type constructions, shell-and-tube heat exchangers (STHE) represent the most popular design. They have been the "work-horse" of the process industry for decades. Figure 2.2 shows a cross-section of a simple STHE, and illustrates the flow configuration.

Shell-and-tube heat exchangers are built of a bundle of tubes, which are inserted into a cylindrical mantle. The tubes are fixed by welding in a tube sheet. One fluid flows through the tubes (tube

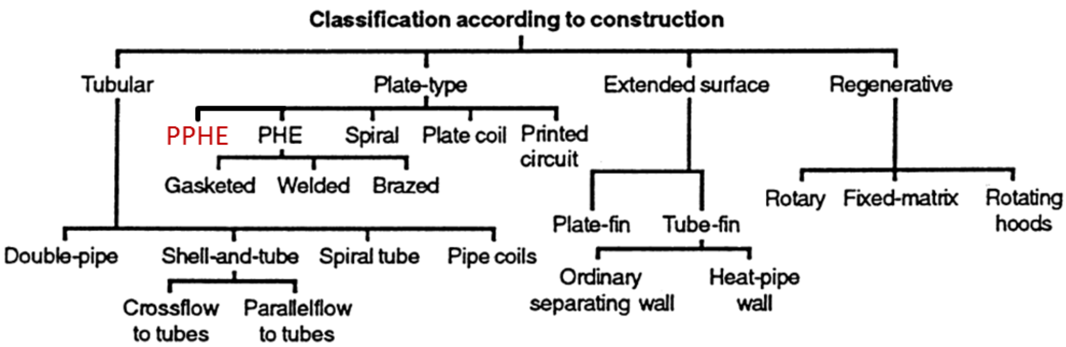

Figure 2.1: Classification of heat exchangers with respect to construction [2].

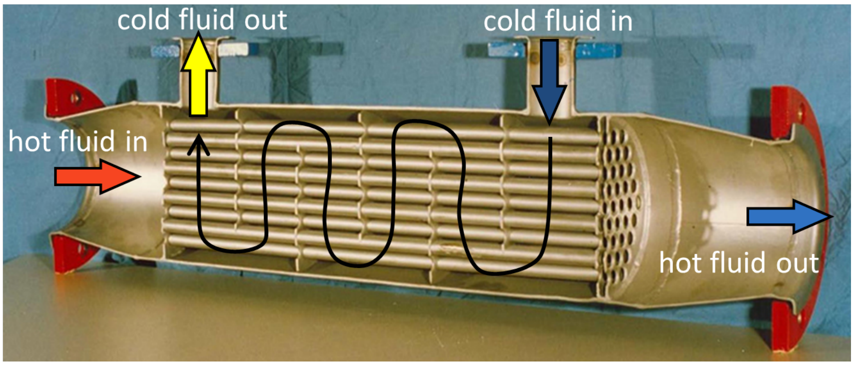

Figure 2.2: Photo of a cross-section of shell-and-tube heat exchanger showing the tubes, baffles and inlet and outlet ports. Photo: www.vdldelmas.com (accessed on 28.06.2017).

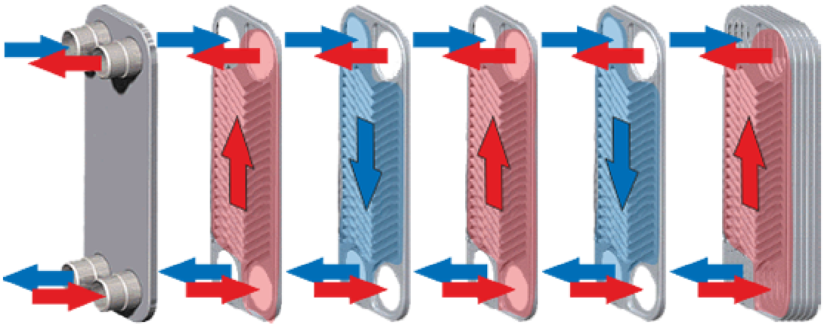

Figure 2.3: Illustration and operating principle of plate heat exchangers [3].

side), while the other flows across and along the tubes (shell side). A front- and a rear-end head is used for evenly distributing the tube-side fluid over all tubes. The shell-side fluid enters and exits the mantle via shell ports, while the fluid is commonly distributed using baffles. STHE are versatile; they are used for a wide range of applications, from single-phase heat transfer (e.g. fluid/fluid, gas/fluid) to heat transfer with phase change (e.g. condensation, falling-film evaporation and pool boiling).

Various different internals are employed in STHE. They are used to influence heat transfer and pressure drop, to reduce thermal stresses, to facilitate cleaning, to improve fluid distribution, to protect the tube bundle from abrasion, etc. STHE have a simple design, they are easy to manufacture and very robust, especially for high pressure and temperature applications.

The second major heat exchanger construction in process industry is the plate heat exchanger (PHE) with cross-corrugated channels (Fig. 2.3). PHE can be classified as gasketed, welded or brazed. They consist of multiple thin rectangular metal plates with corrugated surface patterns (e.g. chevron pattern). These patterns are shaped into the plates using an embossing tool. The plates are stacked together to a "sandwich", whereby the corrugations of opposing plates contact and cross each other. Each plate has four corner ports; in pairs, they provide access to the flow passages on either side of the plate. The flow passages between the plates, which contain the hot-side or cold-side fluid, are very narrow and highly interrupted, leading to intensified fluid mixing. In gasketed PHE, the metal plates are sealed around the edges by gaskets, while in welded or brazed PHE, the edges are welded or brazed to ensure leak tightness. Consequently,

Table 2.1: Assessment of shell-and-tube (plain tubes) and plate heat exchangers (cross-corrugated channels) (cf. [2, 10]).

Criterion	STHE	PHE
Compactness (m^2/m^3)	up to 200	up to 600
U-value[a](W/m^2K)	150-1200 [b]	1000-4000 [b]
Pressure loss	low	high
Temperature range ($^\circ C$)	limited only by materials used	$-35 < T < 200$
Maximum pressure (bar)	300	25
Design experience;	extensive	less than for STHE;
Proven design methods	available	less accurate than for STHE
Scale-up (flexibility)	costly (new design required)	simple[c]
Cleanability	good	only possible for gasketed PHE
Leak tightness	good	poor for gasketed PHE
Cost ($\$/(UA) = \$/(W/K)$)	0.18[d]	0.054[d]

[a] Heat transfer coefficient.
[b] Liquid to liquid.
[c] Numbering-up of channels to reach desired heat transfer area.
[d] Valid for $UA = 6.3\text{x}10^4 (W/K)$.

gasketed PHE can be disassembled to add or remove metal plates, thus varying the heat transfer area, or to facilitate cleaning. Welded-type and brazed-type PHE are less flexible, and cannot be cleaned once assembled. Similar to STHE, PHE can be used for numerous applications ranging from single-phase heat transfer to heat transfer with phase-change.

Table 2.1 summarizes some key aspects of standard shell-and-tube and plate heat exchangers. It shows that the latter are more compact with higher overall heat transfer coefficients U. However, the very narrow and highly interrupted channels in PHE lead to higher pressure losses, compared to STHE. Furthermore, PHE are far less robust than STHE. Especially gasketed PHE cannot be used for high operating pressures, because of leak tightness problems. Moreover, materials commonly used for the gaskets (e.g. rubber) have low resistance to high temperatures and aggressive chemicals. This problem can be avoided in welded or brazed PHE; however, this construction cannot be disassembled, hence, cleaning of the plates is not possible. Also scale-up flexibility is an important aspect. Since fluid flow and heat transfer characteristics are the same in every channel of a PHE, regardless of the number of successive channels used, a variation of the heat transfer area of PHE can be achieved by simply adding or removing plates. Enlarging heat transfer area in STHE requires increasing number or length of the tubes, which consequently involves a new design calculation. Also, PHE are usually significantly cheaper than STHE. The manufacturing of PHE is largely automated. In contrast, STHE are custom made equipment manufactured to specification. Their production includes numerous steps, which are difficult to automate, such as the welding of each individual tube into the tube sheet.

Along with constructive aspects of STHE and PHE, design experience and the availability of proven design methods play an important role regarding costs, efficiency and reliability of the

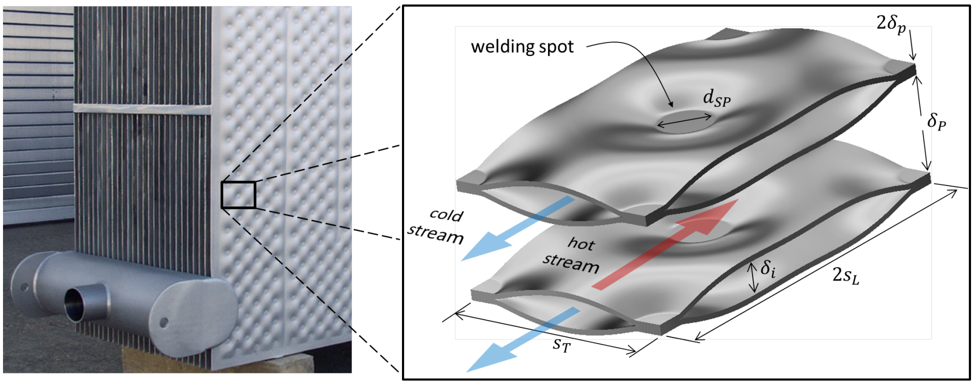

(a) (b)

Figure 2.4: Photo (www.lob-gmbh.de, accessed on 08.01.2016) of a pillow-plate heat exchanger (a) and representation of the characteristic geometry parameters (b). Adjusted from [4].

equipment. These aspects reduce the risk of under-sizing, help to avoid unnecessary over-sizing and allow for efficient design. Design experience is more extensive for STHE than for PHE, since the former represent one of the oldest and most frequently used heat exchanger types in process industry. Also design methods available in literature (e.g. [2] and [10]) are generally more accurate for STHE compared to PHE.

2.2 Pillow-plate heat exchangers (PPHE)

Pillow-plate heat exchangers (PPHE) have gained increased attention in the process industry as a promising alternative to conventional heat transfer equipment. They are assembled as a stack of pillow plates arranged in parallel (Fig. 2.4(a)), whereas the term *pillow* originates from the characteristic three-dimensional wavy surface. The channels formed between adjacent pillow plates are denoted as *outer pillow-plate channels* and the channels inside pillow plates as *inner pillow-plate channels*. The inner channels commonly facilitate the cold fluid (e.g. cooling water) of the heat exchanger, while the outer channels contain the hot fluid (e.g. hot steam). In situations where the fluid in the inner channels has a low heat capacity rate, "baffle weldings", which guide the flow (cf. Fig. 2.5(a)) are introduced, leading to increased mean stream velocity and improved flow distribution.

Figure 2.5 illustrates the broad range of applications areas and geometrical constructions of pillow-plate equipment. They can be used as top condensers in distillation columns (Fig. 2.5(b)), they can be arranged concentrically in a tank (Fig. 2.5(c)), and they can be used for cooling the mantle of stirred tanks (Fig. 2.5(d)), e.g. in dairy industry.

Pillow plates are manufactured by an "inflation" process. It involves superimposing two sheets of metal, which are sealed at the edges by welding (laser welding or resistance welding), while the inner faces of the sheets are joined by spot-welding. The sheets are then expanded ("inflated") and separated between the spot welds by hydro-forming (cf. [12]). The spot pattern is regular, commonly triangular or equidistant. Figure 2.4(b) shows the most important characteristic

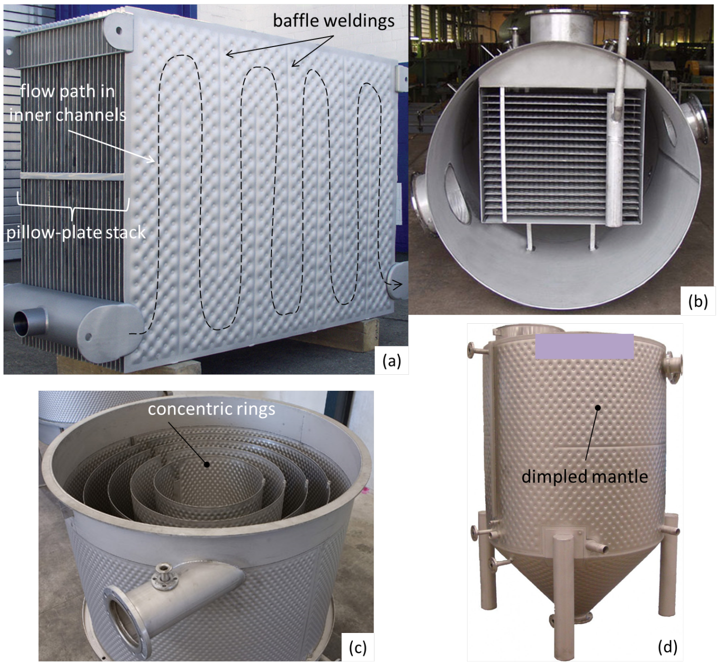

Figure 2.5: Illustration of the geometrical flexibility of PPHE. Plate stack arrangement (photo: www.lob-gmbh.de, accessed on 28.06.2017) (a), top-condenser (photo: www.lob-gmbh.de, accessed on 28.06.2017) (b), concentric pillow-plate rings (photo: www.deg-engineering.de, accessed on 28.06.2017) (c) and mantle cooling of tank (photo: www.keppels.nl, accessed on 26.06.2017) (d).

geometry parameters of PPHE: the welding spot diameter d_{SP}, the transversal welding spot pitch s_T, the longitudinal welding spot pitch $2s_L$, the maximum inflation height δ_i of the inner pillow plate channels, the maximum distance between adjacent pillow plates δ_P, and the thickness of the metal sheets δ_p. These parameters can be varied according to requirements on thermo-hydraulic performance and on structural stability. Table 2.2 summarizes some key features of PPHE.

Pillow plates offer several design advantages, such as a fully welded and hermetically sealed construction, a high structural stability, compactness and light weight. The manufacturing is simple and cheap. Overall heat transfer coefficients in PPHE lie between those in STHE and in PHE. However, PPHE can operate in a much wider temperature and pressure range than PHE. Considering costs, it is currently difficult to obtain representative values.

Some important reasons for using PPHE are listed below.

- High geometrical flexibility. In principal, they can be adapted to any geometry to form double-walls for cooling or heating.
- Use in applications concerning high viscosity fluids, gas cooling (where the gas has a high heat capacity rate) and condensation. PPHE offer low pressure loss in the outer channels.
- Use in applications concerning dirty media. PPHE offer easy cleaning of the outer channels.
- Use in applications concerning large differences between the heat capacity rates of the hot and cold fluids. PPHE allow a variation of the distance between adjacent pillow plates δ_P

Table 2.2: Assessment of pillow-plate heat exchangers.

Criterion	PPHE
Compactness (m^2/m^3)	up to 400[e]
U-value (W/m^2K)	higher than for STHE but lower than for PHE
Pressure loss	low in the outer channels
Temperature range ($°C$)	up to 800[f]
Maximum pressure (bar)	> 100 bar[g]
Design experience	moderate
proven design methods	not available in literature
Scale-up (flexibility)	similar to PHE
Cleanability	good in the outer channels
Leak tightness	very good (fully welded)

[e] Theoretical consideration based on the equations shown in Chap. 4.
[f] According to [13].
[g] According to [14].

(independent of the inner channels). The distance δ_P can be adapted to accommodate the fluid with the larger heat capacity rate, so as to avoid extreme flow velocities and excessive pressure loss.

A key problem with PPHE today is the lack of publicly available, reliable design methods and the absence of reference applications in industry. This hinders their wide spread application. In contrast to conventional equipment, literature on PPHE is scarce.

Mitrovic and Peterson [15] were the first to publish experimental results on forced convection heat transfer in a pillow plate. Based on the measured data, they developed an empirical Dittus-Boelter type correlation (cf. [16]) for heat transfer coefficients. This correlation rested on measurements of only one pillow-plate geometry. However, variability of the characteristic geometry parameters of pillow plates shown in Fig. 2.4 is practically unlimited.

Mitrovic and Maletic [17] tried to develop more universal design methods for pillow plates and to gain a more detailed understanding of fluid dynamics and heat transfer in pillow-plate channels. They performed a comprehensive CFD study over a wide range of pillow-plate geometries. Similar to [15], they developed an empirical Dittus-Boelter type Nusselt correlation, which was able to approximate their numerical data with an accuracy of $\pm 10\%$. However, they used certain simplifications regarding both the geometrical representation of the wavy pillow-plate surface based on trigonometric functions, and flow description.

Furthermore, in [17] a laminar model was used for the investigation of fluid flow and heat transfer, even at Reynolds numbers at which the flow was turbulent. As mentioned by Maletic [18], the use of the laminar model resulted in an underestimation of pressure loss and especially heat transfer coefficients, as compared to the measurements carried out in [15]. Maletic [18] also performed simulations with the standard $k - \epsilon$ turbulence model; however, this resulted in a significant over-prediction of heat transfer coefficients. Moreover, the Prandtl number was kept constant in the simulation studies in [17], and thus, the dependency of the Nusselt number on the Prandtl number in pillow plates could not be captured.

2.3 Conclusions and objectives

While STHE have been treated intensively and their design methods are freely available in literature, PPHE represent an innovative heat exchanger design, for which many open questions exist. The lack of design principles is a major obstacle for the widespread application of PPHE in process industry. In fact, it acts as an obstacle to innovation, since engineers in process industry are not able to estimate the potential benefits of PPHE compared to conventional heat exchangers. This forces them to almost automatically prefer the "safer", more conventional solution. Although manufacturers are capable of designing PPHE, their knowledge is a company secret not available to the public. Furthermore, it is estimated that PPHE are currently being over-sized by as much as $30\% - 50\%$, due to uncertainties in the design methods. A more accurate design would lead to considerable savings in energy, resources, weight and costs, thus revealing the true potential of PPHE.

The aim of this work is to close the current knowledge gap on PPHE design, by developing accurate methods for the thermo-hydraulic design of such equipment. Since the variability of the geometry parameters of PPHE shown in Fig. 2.4 is extremely high, an experimental investigation of the thermo-hydraulic characteristics of PPHE could be too costly and time consuming. Computational fluid dynamics (CFD) offer an efficient and flexible alternative for studying flow and heat transfer in PPHE.

3 Theoretical background

In this work turbulent fluid dynamics and heat transfer in the channels of pillow-plate heat exchangers are investigated mainly using Computational Fluid Dynamics (CFD) methods, whereas CFD is accompanied by experimental studies. Therefore, background information related to CFD and turbulent heat transfer is presented in this chapter elucidating the concepts utilized in this thesis.

3.1 Governing equations of fluid mechanics

Consider an arbitrarily shaped volume of fluid V with a closed surface A subjected to a velocity field $\mathbf{u}$ with a fluid density ρ, as illustrated in Fig. 3.1. Further, consider some extensive quantity Φ (e.g. mass, momentum or energy), which is defined in V and can vary with time t. The rate of change of Φ in V is represented by [19]:

$$\frac{d\Phi}{dt} = \frac{d}{dt}\int_{V(t)} \rho\varphi dV = Q \tag{3.1}$$

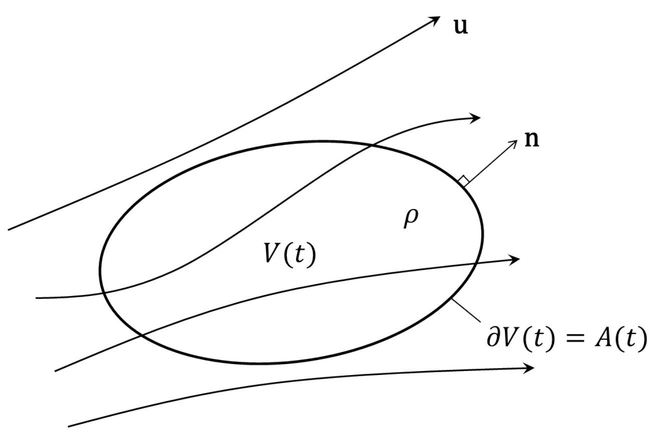

Figure 3.1: Arbitrary control volume of fluid V subjected to a velocity field $\mathbf{u}$.

Equation (3.1) represents a conservation equation for Φ, in which Q denotes its sources. The "density" of Φ is represented by φ (e.g. $\varphi = 1$ for mass and $\varphi = \mathbf{u}$ for momentum), which is continuous in time and space (see [7]). The source Q generally comprises of surface and volume sources. Hence, Eq. (3.1) leads to the following balance (see [20] for sign convention):

$$\frac{d}{dt}\int_{V(t)} \rho\varphi dV = -\oint_{\partial V(t)} (\rho\varphi\mathbf{u})\cdot\mathbf{n}dA - \oint_{\partial V(t)} (-\Gamma_\varphi\nabla\varphi)\cdot\mathbf{n}dA + \int_{V(t)} S_\varphi dV \tag{3.2}$$

The first and second terms on the right-hand-side (RHS) of Eq. (3.2) represent the net convective and diffusive transport of φ across the surface A of the fluid volume V. The volume source of φ is denoted by S_φ.

Equation (3.2) applies to a material control volume of fluid, which can move in space (Langrangian framework), as can be seen by the derivative d/dt in the left-hand-side (LHS) of Eq. (3.2). In fluid mechanics, it is more convenient to describe flow using fixed coordinates in space (Eulerian framework). Hence, consider now that V in Fig. 3.1 represents a control volume fixed in space, then by applying Leibniz integral rule to the time derivative on the LHS of Eq. (3.2), one obtains:

$$\int_{V(t)} \frac{\partial(\rho\varphi)}{\partial t}dV + \oint_{\partial V(t)} (\rho\varphi\mathbf{u_b})\cdot\mathbf{n}dA = -\oint_{\partial V(t)} (\rho\varphi\mathbf{u})\cdot\mathbf{n}dA + \oint_{\partial V(t)} (\Gamma_\varphi\nabla\varphi)\cdot\mathbf{n}dA + \int_{V(t)} S_\varphi dV \tag{3.3}$$

In case the control volume V is fixed in space, the velocity of its boundary is $\mathbf{u_b} = 0$, thus leading to:

$$\int_{V(t)} \frac{\partial(\rho\varphi)}{\partial t}dV = -\oint_{\partial V(t)} (\rho\varphi\mathbf{u})\cdot\mathbf{n}dA + \oint_{\partial V(t)} (\Gamma_\varphi\nabla\varphi)\cdot\mathbf{n}dA + \int_{V(t)} S_\varphi dV \tag{3.4}$$

Furthermore, the surface integrals in Eq. (3.4) can be rewritten as volume integrals by applying Gauss's theorem:

$$\int_{V(t)} \frac{\partial(\rho\varphi)}{\partial t}dV = -\int_{V(t)} \nabla\cdot(\rho\varphi\mathbf{u})dV + \int_{V(t)} \nabla\cdot(\Gamma_\varphi\nabla\varphi)dV + \int_{V(t)} S_\varphi dV \tag{3.5}$$

Eq. (3.5) can also be written as follows:

$$\underbrace{\frac{\partial(\rho\varphi)}{\partial t}}_{\text{Transient term}} + \underbrace{\nabla\cdot(\rho\varphi\mathbf{u})}_{\text{Convetion term}} = \underbrace{\nabla\cdot(\Gamma_\varphi\nabla\varphi)}_{\text{Diffusion term}} + \underbrace{S_\varphi}_{\text{Source term}} \tag{3.6}$$

Equation (3.6) represents the differential form of the generic transport equation ([7]), which forms the basis of most CFD software tools. Using Eq. (3.6) it possible to derive the conservation equations of mass, momentum and energy in a straightforward way, by replacing φ by the corresponding quantity.

3.1.1 Mass conservation

The mass conservation equation is obtained by implementing $\varphi = 1$ into Eq. (3.6):

$$\frac{\partial \rho}{\partial t} + \nabla \cdot (\rho \mathbf{u}) = 0 \tag{3.7}$$

The RHS of Eq. (3.7) is equal to zero since total mass cannot be created or destroyed. In many engineering applications the fluid velocity is significantly lower than the speed of sound. The ratio of these two velocities is expressed by the Mach number $Ma = u/u_c$. If $Ma < 0.3$, then the flow can be assumed to be incompressible ($\rho = const$), and Eq. (3.7) simplifies to:

$$\nabla \cdot \mathbf{u} = 0 \tag{3.8}$$

Equation (3.8) is commonly referred to as the continuity equation, and it states that the velocity field $\mathbf{u}$ is divergence-free.

3.1.2 Momentum conservation

The conservation equation for linear momentum of incompressible fluids[1] is obtained by inserting $\varphi = \mathbf{u}$, $\Gamma_\varphi = \mu$ (Newtonian fluid) and $S_\varphi = \rho \mathbf{g} - \nabla p$ in Eq. (3.6):

$$\rho \left(\frac{\partial \mathbf{u}}{\partial t} + (\mathbf{u} \cdot \nabla) \mathbf{u} \right) = \nabla \cdot (\mu \nabla \mathbf{u}) + \rho \mathbf{g} - \nabla p \tag{3.9}$$

Equation (3.9) is the known Naviers-Stokes equation. It is useful to transform Eq. (3.9) into dimensionless form. This is done by choosing appropriate scales for the variables in the Navier-Stokes equation:

$$\mathbf{x}^* = \frac{\mathbf{x}}{\mathcal{L}}, \qquad \mathbf{u}^* = \frac{\mathbf{u}}{\mathcal{U}}, \qquad t^* = \frac{t}{\mathcal{L}/\mathcal{U}}, \qquad p^* = \frac{p}{\rho \mathcal{U}^2}, \qquad \mathbf{g}^* = \frac{\mathcal{L}}{\rho \mathcal{U}^2} \mathbf{g} \tag{3.10}$$

[1]Only incompressible flows of Newtonian fluids are considered in this work

where $\mathcal{L}$ and $\mathcal{U}$ represent characteristic length and velocity scales, respectively. Inserting the normalized variables into Eq. (3.9), assuming $\mu = const$, and rearranging, gives:

$$\frac{\partial \mathbf{u}^*}{\partial t^*} + (\mathbf{u}^* \cdot \nabla)\, \mathbf{u}^* = \frac{1}{Re}\nabla^2 \mathbf{u}^* + \frac{1}{Fr^2}\mathbf{g}^* - \nabla p^* \tag{3.11}$$

The dimensionless parameters Re and Fr in the RHS of Eq. (3.11) are the well-known Reynolds and Froude numbers[2], respectively. The Reynolds number, which is given by:

$$Re = \frac{\mathcal{U}\mathcal{L}}{\nu} \tag{3.12}$$

represents the ratio of inertial to viscous forces. As Re increases, inertial effects cannot be damped out effectively by viscous forces, thus causing the flow to become unstable and eventually turbulent.

3.1.3 Energy conservation

The energy equation can be written in various forms, depending on the choice of the physical variable φ. The total energy of a fluid is defined as the sum of internal energy, kinetic energy and gravitational potential energy. The last term can be neglected in closed systems or systems with no change in potential energy due to altitude differences. The most useful form of the energy equation is the one in which the temperature appears. Its basis is the equation of change for internal energy. It is obtained by subtracting the mechanical energy equation from the equation for the total energy [21]. Assuming incompressibility, the temperature form of the energy equation is given by:

$$\rho c_p \left(\frac{\partial T}{\partial t} + (\mathbf{u} \cdot \nabla)\, T \right) = \nabla \cdot (\lambda \nabla T) + S_h \tag{3.13}$$

The first term in the right-hand side of Eq. (3.13) represents transport of energy by heat conduction, i.e. Fourier's law [5] (cf. Eq. (3.17)). The source term S_h includes different contributions, such as dissipation (conversion of mechanical energy to inner energy through viscous dissipation). By introducing the dimensionless temperature [8],

$$T^* = \frac{T - T_{ref}}{T_w - T_{ref}} \tag{3.14}$$

[2]The Froude number is not discussed, since it was not relevant for this thesis.

in addition to the dimensionless quantities given by Eq. (3.10), the dimensionless form of the energy equation can be obtained (assumption $\lambda = const$).

$$\frac{\partial T^*}{\partial t^*} + (\mathbf{u}^* \cdot \nabla)\, T^* = \frac{1}{RePr} \nabla^2 T^* \tag{3.15}$$

Here, the dissipation term S_h is omitted for simplicity. The dimensionless parameter Pr in the right-hand side of Eq. (3.15) is the well-known Prandtl number,

$$Pr = \frac{c_p \mu}{\lambda} = \frac{\nu}{\tilde{a}} \tag{3.16}$$

It expresses the ratio of momentum and thermal diffusivities in a fluid. The Prandtl number is of great importance in turbulent boundary layers with heat transfer; this will be shown later in Sec. 3.3.3.

3.2 Heat transfer

Heat is energy, which is transferred across the boundary of a system due to a temperature difference between the system and its surroundings. Heat is always transferred in the direction of falling temperature, as stated by the second law of thermodynamics. Two basic mechanisms are responsible for heat transfer, namely, heat conduction and heat radiation. The latter involves transport of thermal energy by electromagnetic waves. Further information on heat radiation can be found in [5].

In heat conduction, energy is transferred between neighboring molecules in a substance due to a temperature gradient. The rate at which this heat is transferred is described by Fourier's law [21]:

$$\dot{\mathbf{q}} = -\lambda \nabla T \tag{3.17}$$

Equation (3.17) states that the heat flux $\dot{\mathbf{q}}$ is proportional to the temperature gradient ∇T, whereby the thermal conductivity λ represents the constant of proportionality. In gases and liquids heat conduction can be accompanied by convection, which describes energy transfer by the macroscopic movement of the fluid. This combined effect is known as *convective heat transfer*; it generally leads to higher heat transfer rates compared to pure heat conduction in a static fluid (cf. Eq. (3.17)).

Figure 3.2(left) shows the velocity profile in a fluid as a function of the wall distance y. Because of friction, the fluid directly at the wall ($y = 0$) has a velocity $u = 0$ (no-slip condition). With increasing distance from the wall the fluid velocity rises rapidly eventually reaching the velocity

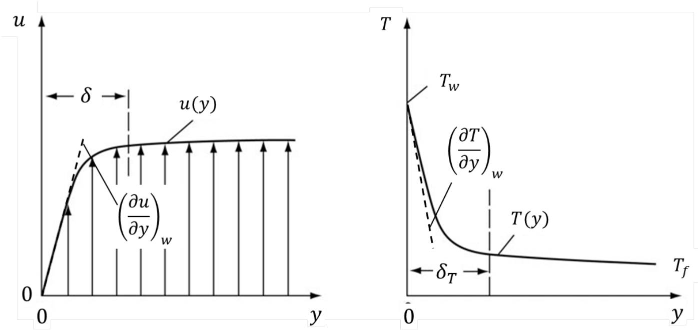

Figure 3.2: Schematic velocity (left) and temperature (right) profiles in a fluid in a wall-bounded (turbulent) boundary layer [5].

of the bulk fluid. Close to the wall there is a region where the change in velocity is greatest. This region is the well-known *boundary layer* (cf. [22]). The boundary layer thickness is represented by δ. The shape of the temperature profile (Fig. 3.2)(right) largely results from the shape of the velocity profile. Similar to the fluid velocity, the fluid temperature increases rapidly from the wall temperature T_w ($y = 0$) to the bulk temperature of the fluid T_f far from the wall. The greatest temperature increase occurs within the thermal boundary layer δ_T. A more detailed description of velocity and temperature profiles in boundary layers is given in Sec. 3.3.3.

The boundary layer represents the main resistance to heat transfer in wall-bounded flows. Therefore, the correct description of this layer is key in heat transfer calculations. Equation (3.17) can be used to determine the heat flux $\dot{q}_w$ transferred through the boundary layer normal to the wall surface, but it requires the evaluation of the wall-normal temperature gradient $(\partial T/\partial y)_w$, as shown in Fig. 3.2(right). In many complex flows the determination of $(\partial T/\partial y)_w$ poses a great challenge, because it requires detailed knowledge of the temperature profile. The heat flux $\dot{q}_w$ can also be calculated by Newton's law of cooling [5],

$$\dot{q}_w = h\,(T_w - T_f) \tag{3.18}$$

which is subsequently used to define the *heat transfer coefficient* h:

$$h \equiv \frac{\dot{q}_w}{(T_w - T_f)} \tag{3.19}$$

Equation (3.18) relates $\dot{q}_w$ linearly with the driving temperature difference $(T_w - T_f)$ using the heat transfer coefficient as the proportionality constant. Basically, h carries all complex physical information regarding the temperature profile in the thermal boundary layer. Combining Eq. (3.17) with Eq. (3.18) gives:

$$h = -\lambda \frac{\left(\frac{\partial T}{\partial y}\right)_w}{(T_w - T_f)} \tag{3.20}$$

Equation (3.20) shows that the heat transfer coefficient represents the ratio of the wall-normal temperature gradient to the driving temperature difference for heat transfer. It shows that with increasing h, the deviation of the temperature profile in the thermal boundary layer from linearity (e.g. pure heat conduction in static fluid over plane wall) increases.

The magnitude of the heat transfer coefficient depends on physical properties, wall-surface geometry and flow regime. It is usually determined using Nusselt number correlations commonly developed using either experiments or CFD simulations (as was done in this work). The Nusselt number Nu (cf. [5]) is a dimensionless number in heat transfer resulting from dimensional analysis:

$$Nu = \frac{hl_{char}}{\lambda} \tag{3.21}$$

In Eq. (3.21), l_{char} represents some characteristic length of the flow/geometry (in theory it is the thermal boundary layer thickness). The Nusselt number is a function of different other dimensionless numbers. In fully developed turbulent forced convection heat transfer, Nu is a function of the Reynolds number and of the Prandtl number:

$$Nu = f\left(Re, Pr\right) \tag{3.22}$$

Numerous researchers have published various forms[3] of this functionality. The most famous one is the power-law form proposed by Nusselt [23]:

$$Nu = cRe^{m}Pr^{n} \tag{3.23}$$

The coefficient c and the exponents m and n are functions of geometry and flow regime; they are evaluated empirically (e.g. regression analysis) using experiments or CFD simulations. For fully developed pipe flow during forced convection heat transfer, Nusselt [23] (cf. [24]) suggested the values $c = 0.024$, $n = 0.786$ and $m = 0.45$. Kraussold [25] determined the values $c = 0.024$, $n = 0.8$ and $m = 1/3$ and Dittus and Boelter [16] found $c = 0.024$, $n = 0.8$ and $m = 0.3$ (for cooling). In summary, the exponent of the Reynolds number is commonly represented by $n \approx 0.8$ and of the Prandtl number by $m \approx 1/3$. In comparison, for laminar fully developed flow, $Nu = const.$

Steimle [26] compared the exponents n and m in Eq. (3.23) for turbulent forced convection heat transfer for numerous different geometries, and found that the exponent of the Reynolds

[3] The focus here lies on Nusselt number correlations for turbulent forced convection heat transfer in hydrodynamically and thermally fully developed boundary layers.

number is often twice that of the Prandtl number:

$$Nu = c\left(Re^2 Pr\right)^n \tag{3.24}$$

Although empirical, power-law type correlations, such as Eq. (3.23) are quite simple, there is still some scepsis concerning their validity. Churchill [27] and Petukhov [28], demonstrated that the typical Nusselt power-law relation lacks physical background. Experimental data tend to scatter around this relationship, implying that there might be another functional interdependence between dimensionless numbers, $Nu = f(Re, Pr)$. This is in accordance to Gnielinski [29], who mentioned that in turbulent flow, the exponent of the Reynolds number depends on the Prandtl number.

The drawbacks of power-law type correlations can be overcome by utilizing the analogy between momentum and heat transfer to derive semi-analytical expressions for the heat transfer coefficient from solutions of the turbulent boundary layer equations. The great advantage of such analogies is that h can be determined directly from the Fanning friction factor ζ_f without the need of heat transfer experiments.

According to Prandtl, the turbulent boundary layer can be sub-divided into a thin, viscous sub-layer adjacent to the wall and a turbulent layer, where the turbulent fluctuations dominate momentum transfer (cf. Sec. 3.3.3). By integrating the boundary layer equations (cf. [22]) over these two layers, Prandtl derived his *two-layer* heat transfer model known as the *Prandtl-Analogy* [30]:

$$Nu = \frac{(\zeta_f/8)\, RePr}{1 + \frac{u_\delta}{u_m}\,(Pr-1)} = \frac{(\zeta_f/8)\, RePr}{1 + y_\delta^+\sqrt{\zeta_f/8}\,(Pr-1)} \tag{3.25}$$

In Eq. (3.25), $\frac{u_\delta}{u_m}$ represents the ratio of the flow velocity at the boundary of the viscous sub-layer to the velocity outside the boundary layer. This ratio is equivalent to $y_\delta^+\sqrt{\zeta_f/8}$, whereby y_δ^+ represents the dimensionless distance (in inner coordinates; see Sec. 3.3.3) from the wall surface, where the viscous sub-layer and the turbulent layer intersect. A common value for $y_{\delta,u}^+ = 10.8$.

In deriving Eq. (3.25), Prandtl assumed the thickness of the sub-layers for heat and momentum to be equal. This assumption holds only for $Pr \approx 1$, however, for large $Pr > 1$, e.g. oils, the thermal sub-layer lies deep within the viscous sub-layer (cf. Sec. 3.3.3). In such a case, (molecular) heat conduction is only significant in the conductive layer but not in the rest of the viscous sub-layer. In order to rectify this short-coming more accurate continuous models of the eddy diffusivity (cf. Sec. 3.3) were adopted by other researchers. A very popular continuous model is that of Petukhov and Popov [31]:

$$Nu = \frac{(\zeta_f/8)\, RePr}{1.07 + 12.7\sqrt{(\zeta_f/8)}\left(Pr^{2/3}-1\right)} \tag{3.26}$$

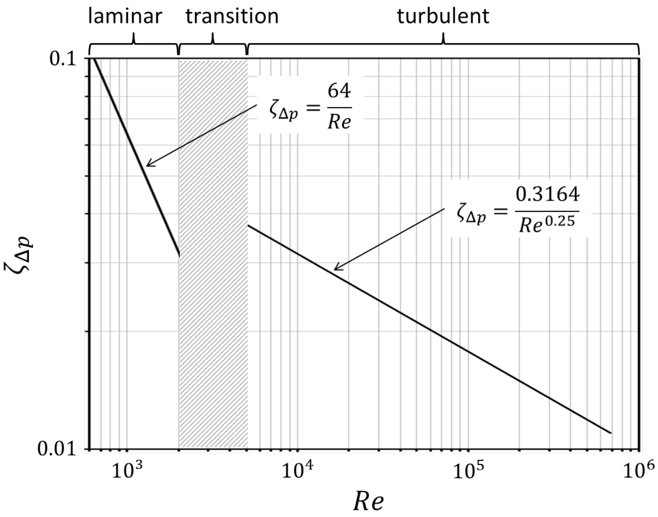

Figure 3.3: Plot of Darcy friction factor $\zeta_{\Delta p}$ against the Reynolds number for flow in pipes covering the laminar and fully turbulent regime.

Notice the similarity of Eq. (3.25) and Eq. (3.26). The major difference lies in the exponent of $Pr^{2/3}$ compared to Pr in the denominator. With the exponent 2/3, the dependency of Nu from Pr is corrected for large Prandtl numbers. Equation (3.26) is generally derived for fully developed turbulent boundary layers on solid walls and hence is not restricted to pipe flow.

As could be seen so far, the accurate determination of the heat transfer coefficient in turbulent boundary layers requires detailed information on turbulent transport mechanisms in the boundary layer. Such information can be gained by CFD simulations using sophisticated turbulence models. Therefore, the next sections involve background information on turbulence and turbulence modeling.

3.3 Turbulence

The majority of flows encountered in industrial applications are turbulent flows and are, therefore, of particular interest in engineering. When the Renyolds number substantially exceeds a critical threshold value, e.g. $Re_{crit} = 2300$ in technically smooth pipes, inertia becomes the dominating force. Consequently, perturbations in the flow caused by, e.g., pressure fluctuations, lead to instabilities in the flow, which cannot be damped by viscous forces. If these instabilities prevail, the flow becomes highly intermittent and chaotic. Turbulence is generally characterized by highly irregular and rotational fluid motion. It is inherently transient and 3-dimensional. Moreover, turbulent flow reveals a wide spectrum of spatio-temporal fluctuations and vortex dimensions. These fluctuations lead to rapid mixing in the fluid thus generating rates of momentum transfer far higher than those due to molecular diffusion.

The importance of turbulence in engineering can be illustrated by the example of pressure loss in a pipe. In Fig. 3.3, pressure loss is represented by the dimensionless Darcy friction factor

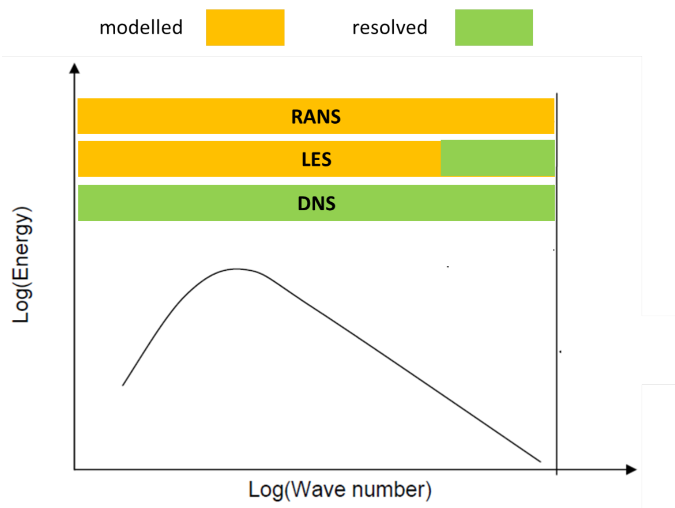

Figure 3.4: Illustration of the Kolmogorov energy cascade [6] and popular strategies for simulating turbulent flows.

$\zeta_{\Delta p}$, which is defined by the following expression:

$$\zeta_{\Delta p} = \frac{2d}{\rho u_m^2} \frac{\Delta p}{L} \tag{3.27}$$

In Eq. (3.27), d denotes the diameter of the pipe, L represents its length and u_m is the mean stream velocity in the pipe.

According to Fig. 3.3, the relation between $\zeta_{\Delta p}$ and Re in laminar flow regime is $\zeta_{\Delta p} \sim Re^{-1}$, whereas in the turbulent regime, this relation changes to $\zeta_{\Delta p} \sim Re^{-0.25}$. In terms of pressure loss (cf. Eq. (3.27)), the relation between Δp and the mean stream velocity u_m is linear in laminar flow, $\Delta p \sim u_m$, and follows the power law, $\Delta p \sim u_m^{1.75}$, in turbulent flow. Hence, pressure loss increases far stronger with rising velocity in turbulent flow than in laminar flow, due to turbulent mixing, which increases momentum transfer to the pipe wall by shear stress.

The simulation of turbulent flows poses a great challenge to engineering. Although it is possible to simulate any turbulent flow by solving the Navier-Stokes (NS) equations together with the continuity equation (*Direct Numerical Simulation* (DNS)), the computational effort required for such a simulation is enormous (cf. [6]), especially for widespread high-Reynolds number flows. This is because all scales must be resolved, from the smallest, *Kolomogorov microscale*, $\eta \sim \left(\nu^3/\varepsilon\right)^{1/4}$ [6], corresponding to dissipative motions, to the largest, corresponding to the dimensions of the physical domain. In addition, the time step chosen for the simulations, which depends on the Courant number [7], must be sufficiently small to resolve the fastest fluctuations. However, the details of turbulent motion provided by DNS are not particularly usefull for design purposes; rather, they influence gross (statistical) properties of the flow, such as time-averaged velocity field $\overline{\mathbf{u}}(\mathbf{x})$, pressure field $\overline{p}(\mathbf{x})$ and temperature field $\overline{T}(\mathbf{x})$. Moreover, the properties of the instantaneous velocity field $\mathbf{u}(\mathbf{x}, t)$ are highly disorganized, while its statistical properties are reproducible. Consequently, for the prediction of turbulent flows, statistical methods with different modeling depth have been developed. These are essentially *Large-Eddy Simulation*

(LES) and turbulence modeling using the *Reynolds-Averaged Navier-Stokes* (RANS) equations. Figure 3.4 shows a plot of energy spectrum over the wave number (frequency of fluctuating quantity). The curve is a schematical representation of the Kolmogorov energy cascade [6]. It shows the existence of large scale, energy-carrying eddies at low frequencies, and very small dissipative eddies at high frequencies. The different strategies for describing turbulent flows are also illustrates in Fig. 3.4. In DNS, all scales must be resolved. In LES, only the large scale eddies are resolved, while the small ones are modeled. In RANS, all scales are modeled.

LES simulations are always unsteady because low-frequency, energy containing fluctuations are resolved. Moreover, the computational effort required for LES is significantly larger than for RANS. Hence, LES simulations are commonly applied in situations where RANS turbulence models fail.

3.3.1 Reynolds Averaged Navier-Stokes equations (RANS)

An arbitrary instantaneous variable $\varphi(\mathbf{x}, t)$ in turbulent flow can be decomposed into a time-averaged quantity $\overline{\varphi}(\mathbf{x})$ and a fluctuating component $\varphi'(\mathbf{x}, t)$, whereby this kind of decomposition is commonly referred to as *Reynolds decomposition.*

$$\varphi(\mathbf{x}, t) = \overline{\varphi}(\mathbf{x}) + \varphi'(\mathbf{x}, t) \tag{3.28}$$

For a statistically steady-state flow (Fig. 3.5(a)) the time-averaged value $\overline{\varphi}(\mathbf{x})$ can be determined by:

$$\overline{\varphi}(\mathbf{x}) = \lim_{\mathcal{T}\to\infty} \frac{1}{\mathcal{T}} \int_0^{\mathcal{T}} \varphi(\mathbf{x}, t)dt \tag{3.29}$$

where the time scale, $\mathcal{T}$, is large compared to that of turbulent fluctuations.

In transient problems (Fig. 3.5(b)), also referred to as *Unsteady-RANS* (*URANS*), time averaging cannot be used and must be replaced by *ensemble averaging*:

$$\overline{\varphi}(\mathbf{x}, t) = \lim_{N\to\infty} \frac{1}{N} \sum_{n=1}^{N} \varphi_n(\mathbf{x}, t) \tag{3.30}$$

where N is the number of elements of the ensemble which must be large enough to eliminate the effects of the fluctuations. The equations of the mean motion (RANS) are obtained by substituting the definitions of the instantaneous quantities Eq. (3.28) into the equations of the instantaneous motion (e.g. Eq. (3.8) and Eq. (3.9)), which are then averaged. For an incompressible turbulent flow, the averaged equations are [19]:

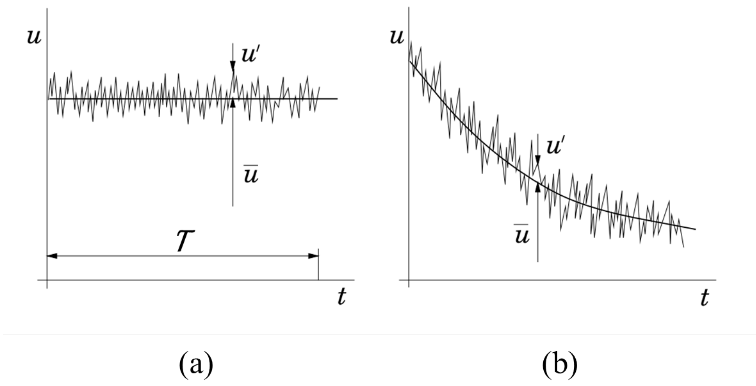

Figure 3.5: Time averaging for a statistically steady-state flow (a) and ensemble averaging for an unsteady flow (b) [7].

$$\nabla \cdot \overline{\mathbf{u}} = 0 \tag{3.31}$$

$$\rho \left(\frac{\partial \overline{\mathbf{u}}}{\partial t} + (\overline{\mathbf{u}} \cdot \nabla)\, \overline{\mathbf{u}} \right) = -\nabla \overline{p} + \nabla \cdot \left(\overline{\tau} - \rho \overline{\mathbf{u}'\mathbf{u}'} \right) \tag{3.32}$$

Equation (3.32) is similar to Eq. (3.9) apart from the last term $\rho\overline{\mathbf{u}'\mathbf{u}'}$ in the RHS of Eq. (3.32). Through the statistical averaging new unknown turbulent correlations appear in the mean flow equations. These new terms couple the mean flow to the turbulent fluctuations; they represent the well known *Reynolds stresses*:

$$\overline{\tau}^R = -\rho\overline{\mathbf{u}'\mathbf{u}'} \tag{3.33}$$

Viscous stresses are represented by $\overline{\tau}$ in the RANS equations and can be determined by:

$$\overline{\tau} = 2\mu\overline{\mathbf{S}} = \mu \left[\nabla\overline{\mathbf{u}} + (\nabla\overline{\mathbf{u}})^T \right] \tag{3.34}$$

In principle, it is possible to determine the unknown Reynolds stresses by multiplying the deterministic Navier-Stokes equations for u_i' and u_j' and then time-averaging this product to obtain an expression for $\overline{u_i'u_j'}$ [6]. However, this procedure leads to yet another set of unknown quantities, namely, $\overline{u_i'u_j'u_k'}$, leading to an underdetermined system with more unknowns than equations. This is the well-known *closure problem of turbulence* [6]. Alternatively, it is possible to close the system of equations by modeling the Reynolds stresses rather than determining them rigorously. Since the fluctuating quantities $\rho\overline{\mathbf{u}'\mathbf{u}'}$ represent stresses and it has been found that they tend to increase as the mean rate of deformation increases, Boussinesq (cf. [6]) suggested that the

Reynolds stresses be proportional to gradients of the mean flow:

$$\overline{\tau}^R = -\rho\overline{\mathbf{u}'\mathbf{u}'} = \mu_t\overline{\mathbf{S}} - \frac{2}{3}\rho k\delta_{ij} \tag{3.35}$$

Equation (3.35) represents the *eddy-viscosity theory* with μ_t being the turbulent or eddy viscosity and k the turbulent kinetic energy:

$$k = \frac{1}{2}\left(\overline{\mathbf{u}'}\right)^2 = \frac{1}{2}\left(\overline{u'_x u'_x} + \overline{u'_y u'_y} + \overline{u'_z u'_z}\right) \tag{3.36}$$

Boussinesq assumed that the turbulent fluxes are transported along the gradients $\nabla\overline{\mathbf{u}}$ of the mean flow in analogy to viscous transport. Since μ_t is a scalar, the conclusion is that turbulence is isotropic everywhere in space, while, in reality, turbulence is mostly anisotropic, thus, μ_t should have been a tensor. Nevertheless, the concept of a simple scalar eddy-viscosity has worked surprisingly well in numerous types of flow and has proven to be very useful in engineering applications. Basically, with the introduction of the eddy viscosity concept, the focus has shifted from the determination of the Reynolds stresses to the determination of the eddy viscosity and the turbulent kinetic energy. From dimensional analysis, μ_t can be expressed by:

$$\mu_t = \rho C V_s L_s \tag{3.37}$$

where C is an empirical constant, and V_s and L_s are turbulent velocity and length scales which characterize the large-scale turbulent fluctuations. In the majority of turbulence models, the velocity scale is preferably represented by $k^{1/2}$ and the length scale by $k^{3/2}/\varepsilon$ (cf. [6]), where ε denotes the turbulence dissipation rate. This leads to:

$$\mu_t = \rho C_\mu \frac{k^2}{\varepsilon} \tag{3.38}$$

Consequently, the aim of turbulence modeling is to develop appropriate equations (turbulence models), which link μ_t and k with quantities characterizing the mean flow only. The most common RANS turbulence models are classified on the basis of the number of additional transport equations that need to be solved alongside the RANS equations (Tab. 3.1).

Unfortunately, to the present day, there is no generic turbulence model applicable to all situations. The number of eddy viscosity models available in literature is large and Tab. 3.1 presents only some of the most popular eddy viscosity models used in engineering. Each turbulence model has its benefits and drawbacks, depending on the modeling depth, quality and the type of flows it has been developed for. Hence, the choice of the turbulence model to be used strongly depends on the type of flow under study.

Table 3.1: Classification of eddy viscosity models (cf. [11]).

Additional transport equations	Example	Ref.
Zero	Mixing length model	
One	Wolfshtein $k - l$ model	[32]
	Spalart-Allmaras model	
Two	Standard $k - \varepsilon$ model	
	Wilcox's $k - \omega$ model	
	Realizable $k - \varepsilon$ model	[33]
	SST $k - \omega$ model	
(Three)	$k - \varepsilon - v^2/k$ model	[34]
Seven	Reynolds stress model	

In zero-equation (algebraic) models, μ_t is determined directly from the mean flow variables by algebraic expressions. While such models are computationally economical, they are often restricted to one-dimensional shear flows and thus too simple for general situations. In contrast, one-equation models solve one turbulent transport equation, usually for the turbulent kinetic energy (e.g. Wolfshtein's [32] one-equation model). Their main advantage over algebraic models is the inclusion of turbulence history effects (e.g. convection and diffusion of turbulent energy), however, they are also limited to relatively simple flows. Two-equation models solve two transport equations, e.g. for k and ε. They are very popular in engineering, because they successfully predict a wide range of complex flows with acceptable computational effort. Reynolds stress models (RSM) are the most advanced eddy-viscosity models; they solve seven additional transport equations (six for the individual Reynolds stresses and one for the dissipation rate ε). They are capable of accurately capturing anisotropy of turbulence, e.g. in boundary layers. However, RSM are computationally very expensive. The focus in this work lied mainly on the application of two-equation turbulence models (with the exception of the $k - \varepsilon - v^2/k$ model) for capturing turbulence effects in PPHE.

The first and most widely used two-equation eddy viscosity model is the standard $k - \varepsilon$ model of Jones and Launder [35]. Two additional transport equations, namely one for k and one for ε, are solved alongside the RANS equations. The eddy viscosity is evaluated according to Eq. (3.38), where k is used to represent the turbulence velocity scale and ε the length scale. The standard $k - \varepsilon$ model is very popular, partially because it is simple to use and provides reliable results for simple shear flows. However, it fails in more complex configurations such as: stagnation-point flows [36], flows with large extra strains, boundary layers with strong adverse pressure gradient or large curvature, and highly anisotropic turbulence [6]. Moreover, it is known to be too dissipative, e.g. the turbulent viscosity in recirculations tends to be too high, thus damping out vortices.

Since the suggestion of the $k - \varepsilon$ model, there have been countless attempts to improve it. A very popular and successful alternative is the realizable $k - \varepsilon$ model by Shih et al. [33], which will be discussed in the following section.

3.3.2 Realizable $k-\varepsilon$ model

The realizable $k-\varepsilon$ model by Shih et al. [33] was the turbulence model of choice for studying fluid dynamics in the inner pillow-plate channels. This model is numerically robust and substantially better than the standard $k-\varepsilon$ model (see [33]). In contrast to the standard model, the realizable $k-\varepsilon$ model satisfies realizability. This means that the normal Reynolds stresses $(\overline{u_i'})^2$ must always be positive and Cauchy-Schwarz inequality for turbulent shear stresses must be satisfied. These conditions can be violated by the standard $k-\varepsilon$ model in flows with large mean strain rate. For example, taking the normal Reynolds stresses in the x-direction obtained by Eq. (3.35) and Eq. (3.38) gives:

$$\left(\overline{u'}\right)^2 = -C_\mu \frac{k^2}{\varepsilon}\left(2\frac{\partial \overline{u}}{\partial x}\right) + \frac{2}{3}k \geq 0 \tag{3.39}$$

Realizability is only satisfied if:

$$\frac{k}{\varepsilon}\frac{\partial \overline{u}}{\partial x} \leq \frac{1}{3C_\mu} \approx 3.7 \tag{3.40}$$

Hence, if the velocity gradient $\partial\overline{u}/\partial x$ exceeds a threshold value, Eq. (3.40) is no longer satisfied and realizability is violated. This happens because in the standard model C_μ is a constant. This assumption is not consistent with experimental observations, in which for example $C_\mu = 0.09$ in the inertial sub-layer of a channel boundary layer and $C_\mu = 0.05$ in homogeneous shear flow. In the realizable model, however, the critical coefficient C_μ (Eq. (3.38)) is expressed as a function of mean flow and turbulence properties (strain rate $\overline{\mathbf{S}}$ and the rotation rate $\overline{\boldsymbol{\Omega}}$).

Moreover, while the transport equations for the turbulent kinetic energy k are identical in the standard and in the realizable models, the latter contains an improved transport equation for the turbulent dissipation rate ε [33]. As mentioned in [33], the difference between the dissipation rate equation of the standard model and the realizable model is the "source" term (production of turbulent kinetic energy). The Reynolds stresses do not appear in the dissipation rate equation of the realizable model. Consequently, this model will be more robust than the standard model when it is used in conjunction with second-order closure schemes, since $\overline{\mathbf{S}}$ is easier to handle numerically than the Reynolds stresses, especially for cases with poor initialization.

Shih et al. [33] tested the realizable $k-\varepsilon$ model for different cases (rotating homogeneous shear flows, boundary-free shear flows including a mixing layer, planar and round jets, channel flow, and flat plate boundary layers with and without pressure gradient) and found that this model performed significantly better or at least as good as the standard $k-\varepsilon$ model in all studied situations.

3.3.3 Near-wall treatment

Many linear eddy viscosity models, including the realizable $k - \varepsilon$ model presented above, are *high-Re* models; they are valid for high Reynolds numbers (fully turbulent flow), when it can be assumed that the eddy viscosity is isotropic. However, in the near-wall region of wall-bounded turbulent flows, the Reynolds stresses become highly anisotropic. The wall normal ($\overline{u_n'^2}$) and shear ($\overline{u_n' u_t'}$) stresses are reduced stronger than the components tangential ($\overline{u_{t,i}' u_{t,j}'}$) to the wall, which is caused by the blocking/damping effect of the wall. Consequently, high-Re turbulence models can not readily be applied near the wall, but require the so-called *near-wall treatment*. These treatments are based on flow physics in turbulent boundary layers; an introduction to this topic will be given in the following sections.

Universal velocity and temperature profiles in turbulent boundary layers

In wall-bounded shear flows, the turbulent boundary layer represents the main resistance for momentum and heat transfer. Friction losses depend on the wall shear stress, which is a function of the wall-normal velocity gradient. Heat transfer is determined by the wall heat flux, which is a function of the wall-normal temperature gradient. Hence, these gradients need to be evaluated accurately in order to obtain the correct values for pressure loss and heat transfer coefficient. Consequently, when using CFD analysis to study transport phenomena in wall-bounded shear flows, it is necessary to properly resolve the turbulent boundary layer.

Figure 3.6(a) shows a typical velocity profile in a turbulent boundary layer. In principle, this profile can be subdivided into two regions:

- Inner region ($\eta_w = y/\delta < 0.2$)

  Close to the wall, turbulent fluctuations are damped; hence, the influence of viscosity on momentum transfer is significant. The variation of total shear stress is negligible: $\overline{\tau}_{tot} = (\overline{\tau} + \overline{\tau}^R) \neq f(y)$; consequently, it can be assumed that $\overline{\tau}_{tot} \approx \overline{\tau}_w$ [6]. The relative contributions of viscous and turbulent stresses to $\overline{\tau}_{tot}$ vary with the distance from the wall. This distance is commonly expressed by the dimensionless *wall coordinate*[4] y^+ [6]:

  $$y^+ = \frac{u_\tau y}{\nu} \tag{3.41}$$

  The parameter $u_\tau = \sqrt{\tau_w/\rho}$ represents the friction velocity.

- Outer region ($\eta_w = y/\delta > 0.2$)

  Far from the wall, viscous stresses are negligible. Momentum transfer is dominated by turbulent fluctuations ($\overline{\tau}^R \gg \overline{\tau}$) originating from large scale eddies. The velocity increases only

[4] The "wall coordinate" is used for scaling the inner region. The outer region usually scales with $\eta_w = y/\delta$.

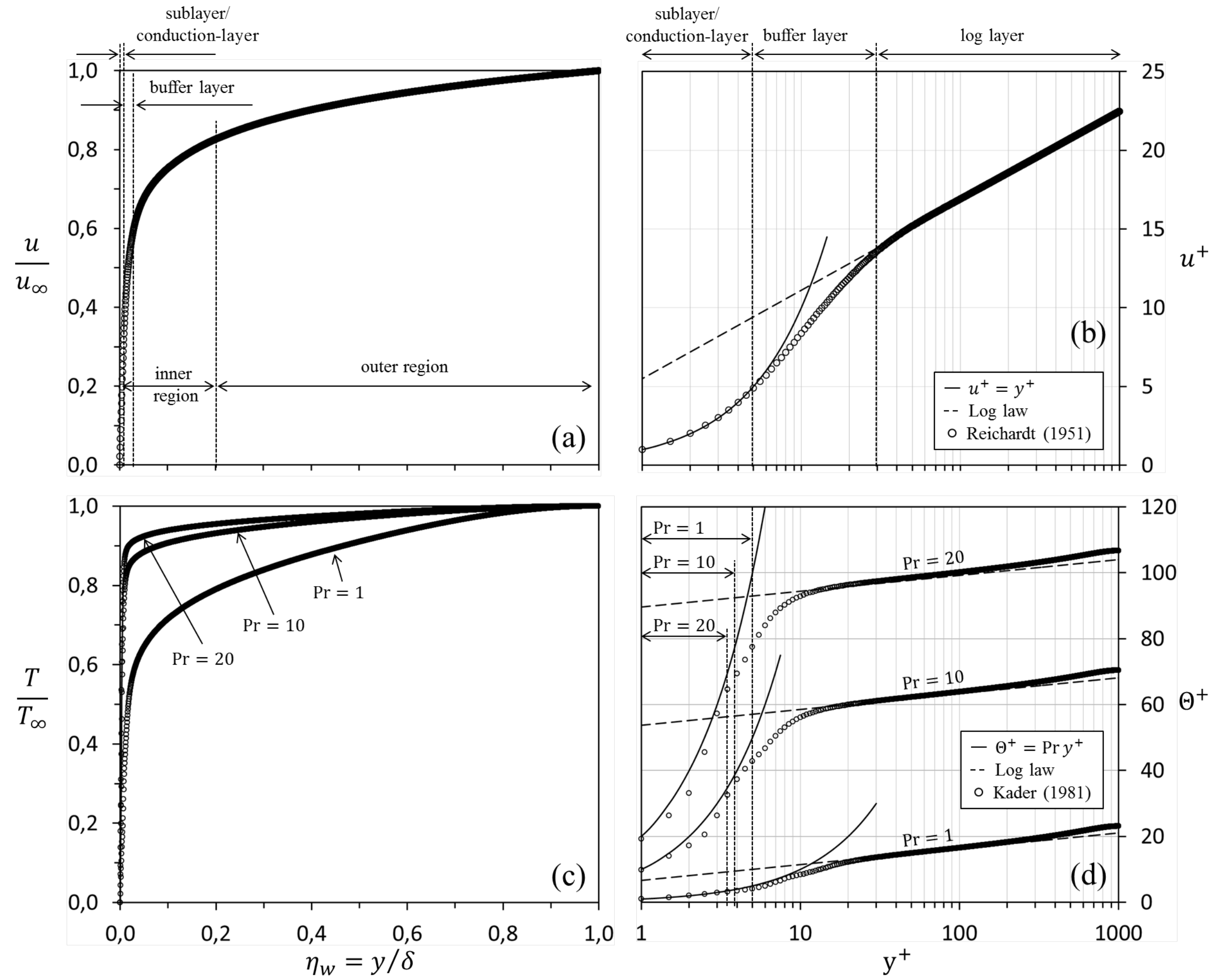

Figure 3.6: A typical velocity profile in a turbulent boundary layer (a); a universal velocity profile in "inner coordinates" for the inner region of a turbulent boundary layer (b); Typical temperature profiles in a turbulent thermal boundary layer for different Prandtl numbers (c); Temperature profiles in *inner coordinates* for the inner region of a turbulent, thermal boundary layer, for different Prandtl numbers (d).

gradually in this region and asymptotically approaches u_∞ (= center-line velocity in pipe flow).

The inner region can be subdivided into three further sublayers: the viscous sublayer, the buffer layer and the logarithmic layer (Fig. 3.6(b)).

- Viscous sublayer ($y^+ < 5$; $\mu \gg \mu_t$)

  Turbulent stresses are negligible in this layer ($\overline{\tau} \gg \overline{\tau}^R$), since $\mathbf{u}'$ falls to zero at the wall. Considering that $\overline{\tau}_{tot} \approx \overline{\tau}_w$ and that viscous transport is the dominating momentum transport mechanism in the viscous sublayer, the velocity profile is almost linear [6] and can be expressed by:

$$u^+ = \frac{\overline{u}(y)}{u_\tau} \approx y^+ \tag{3.42}$$

  Although this sublayer is extremely thin, e.g. $\eta_w \approx 0.005$ (see Fig. 3.6(a)), it represents the dominating resistance to momentum transfer. Hence, it is very important to adequately resolve this layer in CFD simulations, in order to obtain the correct wall-normal velocity gradient and, consequently, the correct wall shear stress.

- Buffer layer ($5 < y^+ < 30$; $\mu \approx \mu_t$)

  In this transition region, the damping effect of the wall is not very strong. Turbulent fluctuations increase and reach the order of viscous stresses $\overline{\tau}$. Hence, Eq. (3.42) is no longer valid and does not follow the true velocity profile, as shown in Fig. 3.6(b). The transition region holds up to a distance of $y^+ = 30$.

- Logarithmic layer ($y^+ > 30$ and $\eta_w < 0.2$; $\mu_t \gg \mu_t$)

  Far enough from the wall, but still in the inner region (where $\overline{\tau}_{tot} \approx \overline{\tau}_w$) of the boundary layer, turbulent stresses become dominant ($\overline{\tau}^R \gg \overline{\tau}$); hence, momentum transfer is significantly more effective in this region compared to the viscous sublayer. As it is clear from the name of the layer, the velocity profile can be represented by a logarithmic function:

$$u^+ = \frac{1}{\kappa}\ln(y^+) + B \tag{3.43}$$

  Equation (3.43) is the famous *log-law of the wall* [6]. The constant κ is von Kármán's constant. The parameter B in Eq. (3.43) represents the intercept on the u^+-axis and commonly has a value of 5.5.

Instead of using three separate functions for representing the complete inner region of a turbulent boundary layer, it is also possible to describe the universal velocity profile by one continuous function, as was done by Reichardt [37]:

$$u^+ = \frac{1}{\kappa}\left(1 + \kappa y^+\right) + 7.8\left[1 - \exp\left(\frac{-y^+}{11}\right) - \frac{y^+}{11}\exp\left(\frac{-y^+}{3}\right)\right] \tag{3.44}$$

The trend of Equation (3.44) is shown in Fig. 3.6(b).

Analogous to the arguments leading to the universal velocity profile, a universal temperature profile can be developed. However, in contrast to momentum transfer, which depends on μ and μ_t, heat transfer is also influenced by the Prandtl number. This is a very important aspect when dealing with heat transfer in turbulent boundary layer, because the appropriate resolution of the thermal boundary layer in CFD simulations depends on the magnitude of the Prandtl number. Consider Fig. 3.6(c), where typical temperature profiles for a turbulent, thermal boundary layer are shown for three different Prandtl numbers. While for $Pr = 1$, the shape of the temperature and velocity profiles is identical, with increasing Prandtl number, they deviate stronger. For $Pr = 20$, the centerline-temperature T_∞ is retained over almost the entire boundary layer height (analogous to plug flow). Consequently, the region in which the largest temperature variation occurs (inner region) becomes extremely thin; and much thinner than that of the velocity profile. Hence, the Prandtl number can be seen as a measure of the ratio of the thickness of the momentum boundary layer to the thickness of the thermal boundary layer.

The temperature profile can also be subdivided into three regions (Fig. 3.6(d)):

- Conduction layer ($\widetilde{a} \gg \widetilde{a}_t$)

  Heat conduction is the dominant transport mechanism in this layer, since $\widetilde{a}_t$ becomes negligible. Hence, the conduction layer represents the main resistance to heat transfer in the thermal boundary layer. The temperature profile can be described by a linear function [6]:

$$\Theta^+ = \frac{T_w - \overline{T}(y)}{T^*} \approx Pry^+ \tag{3.45}$$

  The denominator $T^* = \dot{q}_w / \left(\rho c_p u_\tau\right)$ in Eq. (3.45) has the units of temperature.

  In contrast to the thickness of the viscous sublayer ($y^+ < 5$), the thickness of the conduction layer depends on the value of Pr. For $Pr \approx 1$, the thicknesses of the two layers are roughly equal (cf. Fig. 3.6(a) and (c), or (b) and (d)). However, for $Pr < 1$, the near- wall conduction zone is thicker than the viscous sublayer, the ratio of the two thicknesses being Pr^{-1}. When $Pr \ll 1$, e.g. for liquid metals, the conduction layer spreads from the wall to the region where the logarithmic velocity distribution is valid, so that turbulence has little impact on the bulk heat transfer (see Fig. 3.7). Conversely, when $Pr \gg 1$, the heat conduction layer is deeply immersed in the viscous sublayer (cf. Fig. 3.7), the ratio of the two thicknesses being $Pr^{-1/3}$.

While Eq. (3.45) is valid up to $y^+ \approx 5$ for $Pr = 1$, as shown in Fig. 3.6(d), for $Pr = 20$, it is only valid up to $y^+ \approx 3.5$.

- Buffer layer ($\widetilde{a} \approx \widetilde{a}_t$)

  This transition region is similar to that of the momentum boundary layer. Turbulent heat transfer reaches the order of conduction. As for the conduction layer, the thickness of the buffer layer depends on the Prandlt number.

- Logarithmic layer ($\widetilde{a}_t \gg \widetilde{a}$)

  In the logarithmic region of the thermal boundary layer, turbulent heat transfer dominates over heat conduction. The temperature profile in this region can be described by:

$$\Theta^+ = \frac{1}{0.48}\ln(y^+) + A_T, \quad A_T \approx \frac{5}{3}\left(3Pr^{1/3} - 1\right)^2 \tag{3.46}$$

The temperature profile in the inner region, however, can also be approximated by a continuous function over the entire y^+-range, as was done by Kader [38]:

$$\Theta^+ = Pry^+ \exp(-\Gamma) + \left\{2.12ln\left[\left(1 + y^+\right)\frac{2.5\,(2 - \eta_w)}{1 + 4\,(1 - \eta_w)^2}\right] + \beta\,(Pr)\right\}\exp\left(-\frac{1}{\Gamma}\right) \tag{3.47}$$

The terms $\Gamma = 0.01\,(Pry^+)^4 / \left(1 + 5Pr^3y^+\right)$ and $\beta\,(Pr) = \left(3.85Pr^{1/3} - 1.3\right)^2 + 2.13lnPr$ are both functions of the Prandtl number.

Wall functions approach

Wall functions use algebraic expressions, such as Eqs. (3.42) and (3.43) to describe the velocity profile near walls [7]. They relate wall surface boundary conditions with the flow field far from the boundaries. Consequently, it is not necessary to resolve the turbulent boundary layer in fluid dynamics simulations, which consequently leads to a significant reduction of computational cost. However, wall functions are inappropriate for complex three-dimensional flows and unsteady and separated flows, as those encountered in PPHE.

Damping functions approach

With the damping functions approach (see Patel et al. [39]), the transport equation for ε is modified using algebraic "correction" functions to damp certain terms. These (empirical) functions are designed to correct the behavior of the eddy viscosity near the wall, e.g. $\mu_t = \rho f_\mu C_\mu k^2/\varepsilon$ (f_μ: damping function). Hence, they allow the transport equations for k and ε to be integrated to the wall without assuming a universal law for the velocity profile and equilibrium

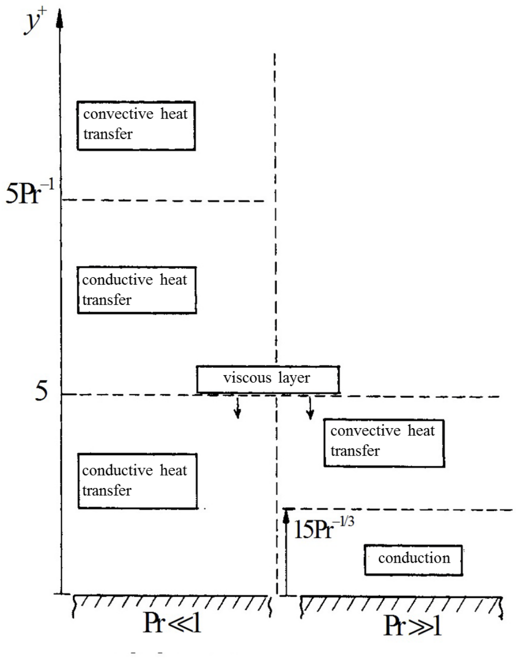

Figure 3.7: Illustration of the structure of the near-wall region depending on the Prandtl number [6].

conditions for k and ε, as is done for wall functions. However, as stated by Durbin [40], it is unreasonable to use a model (the $k-\varepsilon$ model) which is fundamentally incorrect near the wall, and then correct it by introducing an arbitrary function. The problem is that the $k-\varepsilon$ formula is isotropic, while near-wall turbulence is strongly anisotropic.

Two-layer approach

The two-layer approach [41, 42] is an alternative to the damping functions approach and it represented the wall-treatment of choice for the realizable $k-\varepsilon$ model used in this thesis. It allows the $k-\varepsilon$ model to be applied in the viscosity affected region near the wall. The whole domain is subdivided into a viscosity-affected region and a fully-turbulent region. The separation between the two regions is defined in terms of a wall-distance-based turbulent Reynolds number:

$$Re_d = \frac{\widetilde{d}\sqrt{k}}{\nu} \tag{3.48}$$

where $\widetilde{d}$ is the distance normal to the wall.

In the fully turbulent region ($Re_d > 200$), the full $k-\varepsilon$ model (e.g. realizable $k-\varepsilon$) is employed.

The viscosity-affected near-wall region ($Re_d < 200$) is resolved using the one-equation model of Wolfshtein [32]. In this model, the k equation is retained, however, the dissipation rate ε is determined from a prescribed length-scale distribution:

$$\varepsilon = \frac{k^{3/2}}{l_\varepsilon} \tag{3.49}$$

where the length scale l_ε in Eq. (3.49) is computed according to Chen and Patel [43]:

$$l_\varepsilon = \widetilde{d} C_l \left(1 - \exp^{-Re_d/2C_l}\right) \tag{3.50}$$

Also the eddy-viscosity relation is changed to:

$$\mu_{t,2L} = \rho C_\mu l_\mu \sqrt{k} \tag{3.51}$$

while the length scale l_μ in Eq. (3.51) is evaluated using

$$l_\mu = \widetilde{d} C_l^* \left(1 - \exp^{-Re_d/A_\mu}\right) \tag{3.52}$$

In contrast to the van Driest damping function [44], Eq. (3.52) does not involve the friction velocity u_τ and hence is applicable to separated flows too.

The values of the eddy viscosity determined in the near-wall region $\mu_{t,2L}$ are smoothly linked with those computed far from the wall $\mu_{t,k\varepsilon}$ (Eq. (3.38)), as proposed by Jongen [45]:

$$\mu_t = \lambda_\varepsilon \mu_{t,k\varepsilon} + (1 - \lambda_\varepsilon)\, \mu_{t,2L} \tag{3.53}$$

The blending function λ_ε is defined in such a way that it is equal to unity away from walls and to zero in the vicinity of walls (see STAR-CCM+ User Guide [46]).

3.3.4 Elliptic blending $k - \varepsilon$ model

The elliptic blending $k-\varepsilon$ model (EB-$k-\varepsilon$) is the turbulence model of choice for studying fluid dynamics in the outer pillow-plate channels, because of its capability for accurately predicting boundary layer separation over curved surfaces, and consequently, the correct pressure loss. In contrast to the concepts discussed above in Secs. 3.3.2 and 3.3.3, the EB-$k-\varepsilon$ represents a general low-Re $k-\varepsilon$ type turbulence model, that does not require using wall functions or damping functions, because it is valid up to solid walls.

Classical wall treatments are computationally efficient and sufficiently accurate for many engineering applications. However, they employ empirical, algebraic expressions for describing the reduction of eddy viscosity near walls. Moreover, they assume μ_t to be isotropic, whereas this assumption is rarely valid in complex flows. Consequently, these near-wall treatments are not generic and they fail in physical flows involving strong turbulence anisotropy.

Most near-wall treatments assume that damping of eddy viscosity near the wall is a local (viscous) effect. However, as discussed by Durbin [40], this suppression is not really a viscous effect, but is a result of the near-wall reduction of the normal fluctuations $\overline{u_n}^2$ (simply denoted as v^2) due to a pressure-strain mechanism, which must be accounted for globally.

Durbin [40] discusses that the standard $k-\varepsilon$ model fails near the wall because the functionality between k^2/ε (in Eq. (3.38)) and y^+ does not correspond to experimental observations. Moreover, he realizes that k/ε is the correct turbulent time scale in the flow, but k is not the appropriate turbulent velocity scale. The correct velocity scale is represented by v^2; accordingly, the eddy viscosity is given by

$$\mu_t = \rho C_\mu v^2 k/\varepsilon \tag{3.54}$$

Thus, if v^2 is modeled satisfactorily, the need for a damping function (correcting the profile of k/ε) can be avoided.

In [40], Durbin also discusses that the blocking effect of the wall is largely a kinematic rather than dynamic (viscous) effect, which brings the velocity component normal to the wall to zero without the action of viscosity. In fact, this inviscid blocking has an effect at significant distances from the wall ($y^+ \approx 100$) and can be described using an elliptic partial differential equation (i.e. Poisson's equation). Consequently, non-local effects in strongly non-homogeneous turbulent flow should be introduced by an elliptic relaxation.

Considering the above, Durbin developed a general low-Re $k-\varepsilon$ type turbulence model, that does not require using wall or damping functions, because it is valid up to solid walls. The popular v^2-f turbulence model, which is based on Durbin's model, solves transport equations for v^2 and for f together with the k and the ε equations. In principle, the v^2-f model is based on the Reynolds stress transport models, but retaining only the wall-normal fluctuating velocity variance v^2 and its source f, the redistribution of pressure fluctuations. Hence, the v^2-f model recovers turbulence anisotropy in turbulent-boundary and free shear-layers, and is capable of accurately capturing complex flow effects, such as boundary layer separation over curved surfaces, and heat transfer.

Unfortunately, most v^2-f variants suffer from numerical stiffness, which makes them unpractical for industrial or unsteady RANS applications. Furthermore, a key problem associated with eddy viscosity models near walls is posing the correct boundary conditions at the wall. In order to overcome these drawbacks, Billard and Lawrence [34] proposed a new, robust and more code-friendly version of the v^2-f model, which they called the BL-v^2/k (in STAR-CCM+ it is called the EB-$k-\varepsilon$ model). Instead of v^2 and f, this new model uses the variables $\varphi = v^2/k$ and α. The variable v^2/k represents the ratio of wall normal Reynolds stress to turbulent kinetic energy (thus being a measure of the near-wall turbulence anisotropy). The wall-proximity sensitive quantity α takes the value of 0 at a wall and 1 far from it (simple Dirichlet boundary conditions), thus alleviating the stiffness associated to the boundary condition of the elliptic variable f in the $v^2 - f$ model. Therefore, the choice of these variables yields and improved robustness.

In the EB-$k - \varepsilon$, the eddy viscosity is defined by:

$$\mu_t = \rho C_\mu k \varphi \mathcal{T} \tag{3.55}$$

while T represents the turbulent time scale (see [34, 46]). The elliptic blending factor α is determined using the following relationship:

$$\alpha - L^2 \partial_j \partial_j \alpha = 1 \tag{3.56}$$

The inclusion of α in the definition of f allows a blending between the near-wall and the homogeneous form in the φ equation [34].

The superior performance of the EB-$k - \varepsilon$ model in complex flows involving boundary layer separation over curved surfaces is shown in [34].

3.4 Computational fluid dynamics (CFD)

The governing differential equations and models presented so far are used to describe the transport of mass, momentum and energy in fluid flows. In principle, these equations can be solved analytically, but, only for simple physical systems (e.g. flows exhibiting smooth regular streamlines) with simple geometrical boundaries (e.g. such that align with Cartesian or polar coordinate systems, which allow a convenient definition of boundary conditions). For efficiently handling more complex flows (e.g. flow in the channels of PPHE), modern and advanced CFD (numerical) methods are required.

In CFD, the continuous, differential transport equations of fluid mechanics are solved for discrete points in time and space by methods of numerical analysis. The exact differential equations are *discretized* resulting in algebraic expressions, which represent only approximate solutions of the original equations. The system of algebraic expressions can then be solved by typical matrix operations. However, the process of discretization is accompanied by loss of information and, thus, accuracy.

Figure 3.8 shows an overview of standard discretization methods used in CFD based on their flexibility and accuracy. The Finite-Difference-Method (FDM) yields high accuracy, but because discretization is commonly limited to simple, orthogonal grids, its application to complex geometries is problematic. The Finite-Element-Method (FEM) on the other hand is very flexible

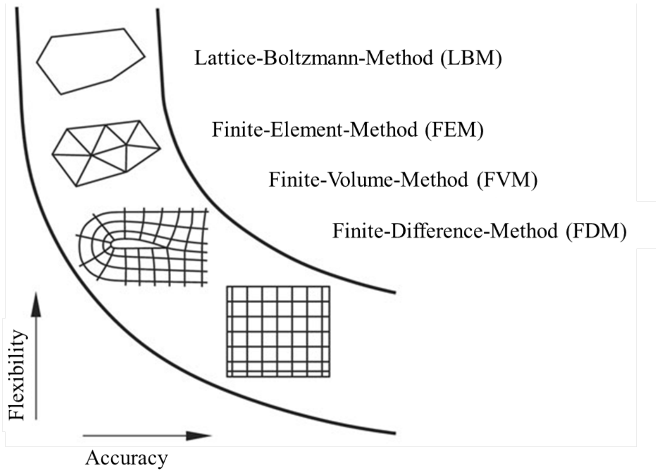

Figure 3.8: Classification of discretization methods with respect to flexibility and accuracy [8].

with regard to complex geometries, but lacks accuracy compared to FDM. The Finite Volume Method (FVM) offers a good balance between flexibility and accuracy, while also being simple and robust (for further details see also [7, 11]). It represents the method most often used in CFD solvers.

In FVM, the computational domain is sub-divided into a finite number of non-overlapping control volumes (CV). The differential conservation equations are integrated over the CV, whereas the computational node, at which the independent variables (ρ, $\mathbf{v}$, p, T, etc.) are calculated, is located at the centroid of such a CV [7, 11]. Taking the diffusion term in Eq. (3.5), for example, and integrating it over a volume V with surface area A, gives:

$$
\begin{aligned}
&\int_V \nabla \cdot (\Gamma_\varphi \nabla \varphi) dV = \\
&\oint_{\partial V = A} (\Gamma_\varphi \nabla \varphi) \cdot \mathbf{n} dA = \\
&\sum_i \int_A (\Gamma_\varphi \nabla \varphi) \cdot \mathbf{n} dA \approx \\
&\sum_i (\Gamma_\varphi \nabla \varphi \cdot \mathbf{n})_{i,cf} A_i
\end{aligned}
\tag{3.57}
$$

In the first step, Gauss's theorem is applied to transform the volume integral to a closed surface integral. In the second step, the closed surface integral is represented by the sum of a finite number of surface integrals. This sum is then approximated by a finite number of discrete surfaces A_i, whereas the values of $(\Gamma_\varphi \nabla \varphi \cdot \mathbf{n})$ are valid at the center-point of these faces, by using the mid-point rule. Hence, Equation (3.57) requires the values of $\nabla \varphi$ at the CV-faces cf. These values can be expressed in terms of the nodal values (of neighboring cells) by using interpolation (discretization scheme). The type of interpolation used strongly influences accuracy and stability of the solution.

In order to obtain high quality results with FVM, care must be taken regarding the mesh,

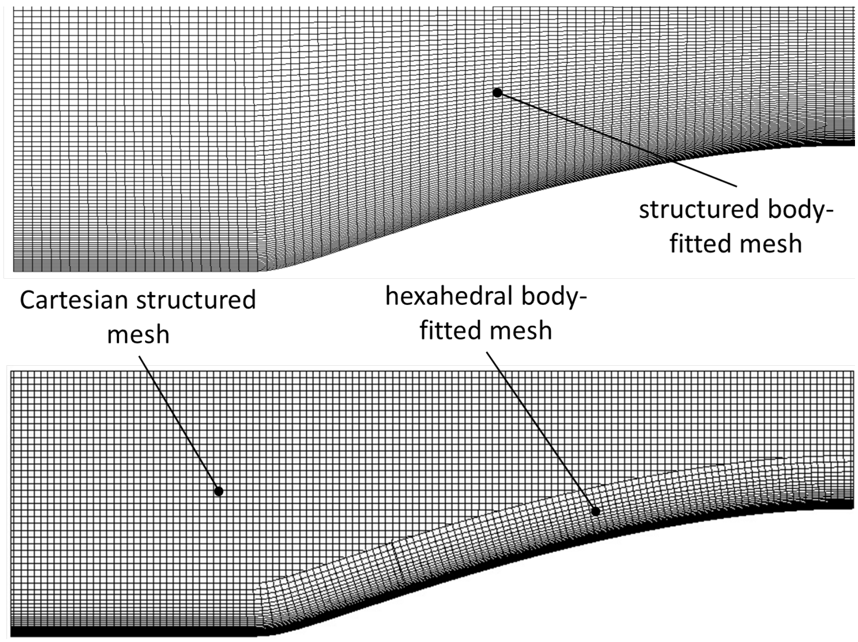

Figure 3.9: Illustration of a block-structured mesh (top) and a structured body-fitted mesh (bottom).

discretization schemes and matrix operations[5]. Flow in PPHX involves complex geometries and flow physics. In such cases, mesh quality is critical for reducing discretization errors. Therefore, in the discussion below only mesh-related aspects, which were considered during meshing of PPHX channels in this work, are described. They can be classified as follows:

- mesh resolution

  The mesh must be refined adequately in areas, where the solution varies rapidly, in order to properly resolve large gradients in ρ, $\mathbf{v}$, p, T, etc. Typical examples of such areas include wall-bounded layers and free-shear layers.

  If computational cost becomes a limiting factor, it is also sometimes possible (e.g. in turbulent boundary layers) to use sub-grid models, such as wall functions [7, 11], for the evaluation of the required quantities (e.g. wall shear stress).

- mesh structure

  The grids used in FVM can be classified as: structured (Fig. 3.9 (top)), unstructured and block-structured (Fig. 3.9 (bottom)). Structured grids can be Cartesian or curve-linear (body-fitted, as in Fig. 3.9 (top)). They commonly consist of hexahedral cells, which can be orthogonal or non-orthogonal. When properly constructed, structured meshes provide several advantages over unstructured ones, such as straightforward numerical implementation, simple cell-connectivity and matrices of fixed band-width. Their main disadvantage is related to lower adaptability to complex geometries.

  In contrast, unstructured meshes use polyhedral cells with typically 10 faces (i.e. 10 neighboring cells). They are far more flexible with respect to geometrical topology. However,

[5] Discretization schemes and matrix operations are not further discussed here and can be found in [7, 11].

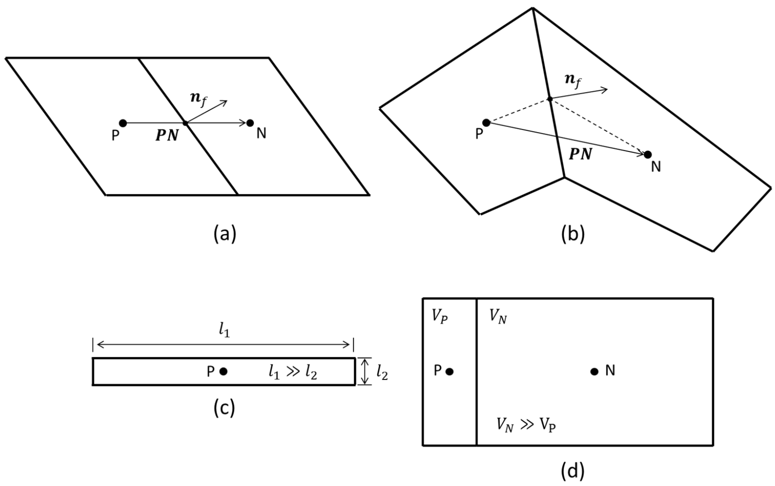

Figure 3.10: Typical criteria for assessing mesh quality. Non-orthogonality (a), skewness (b), aspect ratio (c) and volume ratio (d).

more neighbors means more storage and computing operations per cell, as compared to hexahedral cells. Moreover, cell quality is usually lower for polyhedral cells than for hexahedral ones; this consequently leads to larger numerical errors.

Block-structured meshes combine the advantages of the mesh structures mentioned above. They allow structured meshes to be used efficiently with complex geometries. The grid is sub-divided into different regions, while each region has a different type of mesh structure (Fig. 3.9 (bottom)) and can also have a different coordinate system. Hence, the most appropriate mesh can be applied to the corresponding geometrical topology (curvelinear mesh with curved surfaces, Cartesian mesh with rectangular geometries). Moreover, different blocks can be handled with required mesh refinement levels.

- cell quality (e.g. non-orthogonality, skewness, aspect ratio, volume ratio)

  In addition to the mesh resolution and mesh structure, the type and shape of cells used with FVM strongly influence the stability and accuracy of the solution. Typical criteria used to evaluate cell quality include: non-orthogonality (3.10(a)), skewness (3.10(b)), aspect ratio (3.10(c)) and volume ratio (3.10(d)).

  Non-othogonality error involves the angle between the center-to-center vector $\mathbf{PN}$ of adjacent cells and the normal vector $\mathbf{n}_f$ of the face that connects these cells. Equation (3.57) requires that $\nabla\varphi_{cf}$, which is obtained by interpolation using the nodal values P and N, is multiplied by the face normal vector $\mathbf{n}_f$. Both vectors must be co-linear, otherwise, solution accuracy is reduced or even un-boundedness can arise [47].

  Skewness error is a more serious numerical diffusion-type error. Considering Eq. (3.57), it requires the calculation of $\nabla\varphi_{cf}$ at the mid-point of the cell face. However, with skewed cells (according to Fig. 3.10(b)), an approximation of $\nabla\varphi_{cf}$ by linear interpolation using the points P and N will give the value of the gradient at a point on the face, which does not coincide with its mid-point. The result is again loss of solution accuracy (cf. [47]).

  Even orthogonal cells, which do not suffer from non-orthogonality or skewness error, can produce numerical errors. Examples are cells with high aspect ratios (Fig. 3.10(c)), i.e.

large length l_1 to height l_2 ratio, or also when the volume ratio V_N/V_P (Fig. 3.10(d)) between adjacent cells becomes to large.

4 Determination of PPHE geometrical design parameters

The thermo-hydraulic design of heat exchangers commonly involves geometrical design parameters, such as the heat transfer area, mean cross-sectional area and hydraulic diameter. For conventional equipment, determination of such parameters is usually straightforward; their simple geometry can be defined by basic forms, such as squares, circles, triangles and sine curves. The exact geometry of the wavy pillow-plate surface, however, cannot be fully pre-defined, since it results from the hydroforming process. Therefore, the prediction of geometrical parameters for PPHE is more challenging. Whereas they could be determined experimentally for existing pillow plates, a method for accurately predicting these parameters a priori was not available.

As mentioned in Sec. 2.2, Mitrovic and Maletic [17] were the first to publish a determination method for the geometrical design parameters of pillow plates. They adopted a three-dimensional trigonometric function for the description of the wall waviness and used a circular surface for the welding spots. As a consequence of this simple approach, the maximum channel height always appears at the intersection point between the longitudinal and transversal pitch of the welding spots, regardless of the welding spot pattern used. For a non-equidistant pattern, this results in channels with a local cross-section different from reality, where a local narrowing of the channel is observed (Fig. 2.4(b)). In [17], a method was proposed to calculate the inner hydraulic diameter of the pillow plate using an approximation of the wavy channel by a plane duct (plane parallel plates). This was done based on a representative channel height, selected in such a way that the flat channel volume is the same as the volume of a corresponding pillow-plate channel. The channel volume can be determined experimentally with an existing pillow plate; however, such an approach lacks predictiveness. Hence, a predictive method for the determination of the channel volume is required. Mitrovic and Maletic [17] calculated this volume by integrating their three-dimensional trigonometric function.

In this work, an alternative approach is presented, which is based on forming simulations providing accurately determined geometrical parameters required for the design of PPHE. This

A part of the material presented in this chapter has been published in Piper et al. [48].

"virtual manufacturing" method is flexible, predictive and capable of capturing all important geometrical features of pillow plates.

4.1 Definition of the geometrical design parameters

The evaluation of the geometrical design parameters - hydraulic diameter, heat transfer area and cross-sectional area - for pillow plates is not a straightforward task, because of their complex geometry. Since the cross-sectional areas of pillow plates are small, even insignificant calculation errors can cause large discrepancies in the mean stream velocity. Due to the waviness of the inner pillow-plate channel, the cross-section $A_{cs,i}$ and the wetted perimeter $P_{w,i}$ depend on the spacial coordinates. Hence, the local hydraulic diameter $d_{h,i}$ $(= 4A_{cs,i}/P_{w,i})$ varies periodically along the flow direction. A volumetric-mean hydraulic diameter is obtained by integrating the local hydraulic diameter over a periodic element of the pillow plate of length s_L (see Fig. 4.1):

$$\overline{d}_{h,i} = \frac{4}{s_L} \frac{\int_0^{s_L} A_{cs,i}\,(y)\,\mathrm{d}y}{\int_0^{s_L} P_{w,i}\,(y)\,\mathrm{d}y} = \frac{4V_i}{A_{w,i}} \tag{4.1}$$

The quantity V_i represents the inner volume of the periodic element of the pillow-plate channel and $A_{w,i}$ the wetted wall area. According to Eq. (4.1), the mean hydraulic diameter is independent of the flow direction. This means, that for a geometry with the same inflation height and subsequent rotation of the welding spot pattern by 90°, i.e. when s_L and s_T are interchanged, the hydraulic diameter remains the same.

As follows from Eq. (4.1), the calculation of the mean hydraulic diameter of the pillow plate requires the evaluation of only two geometrical quantities, V_i and $A_{w,i}$. An experimental determination is costly and time consuming due to the large number of possible geometrical variations of the pillow plate. Hence, an accurate and predictive method for the evaluation of these parameters is required.

Inner parameters

The mean hydraulic diameter of the inner pillow-plate channel is determined by Eq. (4.1). The inner mean cross-sectional area is evaluated by dividing the inner channel volume of a characteristic element (Fig. 4.1) by the longitudinal pitch:

$$\overline{A}_{cs,i} = \frac{V_i}{s_L} \tag{4.2}$$

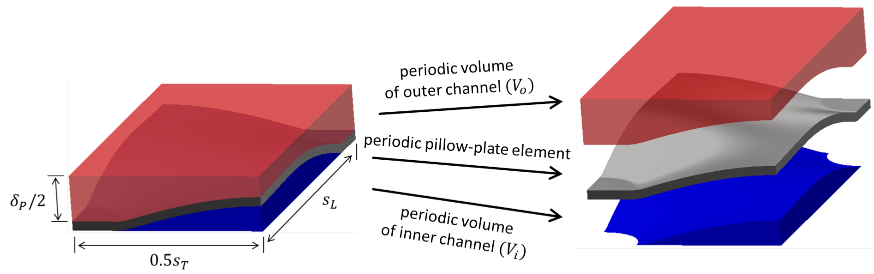

Figure 4.1: Characteristic periodic element of a PPHE for the evaluation of V_i and A_w.

The heat transfer area is assumed to be equal to the wetted area of the inner wall:

$$A_{HT,i} = A_{w,i} \tag{4.3}$$

The welding spot area is not considered within $A_{HT,i}$. Heat conduction in the welding spots possibly leads to an enlargement of the inner heat transfer area; however, their contribution to overall heat transfer is expected to be marginal. Furthermore, they cover usually only about $3-10\%$ of the pillow-plate surface area, and thus, neglecting the welding spots from $A_{HT,i}$ seems reasonable.

The equations for the inner parameters are derived for the periodic element shown in Fig. 4.1. The total cross-sectional area of the pillow plate is calculated by multiplying $\overline{A}_{cs,i}$ by the number of periodic elements disposed across the pillow plate width B (Fig. 4.2(a)):

$$\overline{A}_{cs,i,tot} = \overline{A}_{cs,i} 4 \left(\frac{B-2l_E}{s_T}\right) \tag{4.4}$$

The term $B-2l_E$ in Eq. (4.4), indicates that the edges l_E of the pillow plate (cf. Fig. 4.2(a)) are to be subtracted from the total width. The total inner heat transfer area is obtained in a similar way:

$$A_{w,i,tot} = A_{w,i} 4 \left(\frac{B-2l_E}{s_T}\right)\left(\frac{L-2l_E}{s_L}\right) \tag{4.5}$$

In Eq. (4.5), the edges of the pillow plate are subtracted from both the total width B and total length L of the pillow plate. The edges are not considered in the inner heat transfer area for the same reason as for the welding spots.

Outer parameters

The geometrical parameters for the channel between adjacent pillow plates can be determined directly from the inner parameters. The necessary information is extracted from a characteristic periodic element of a PPHE, as illustrated in Fig. 4.1.

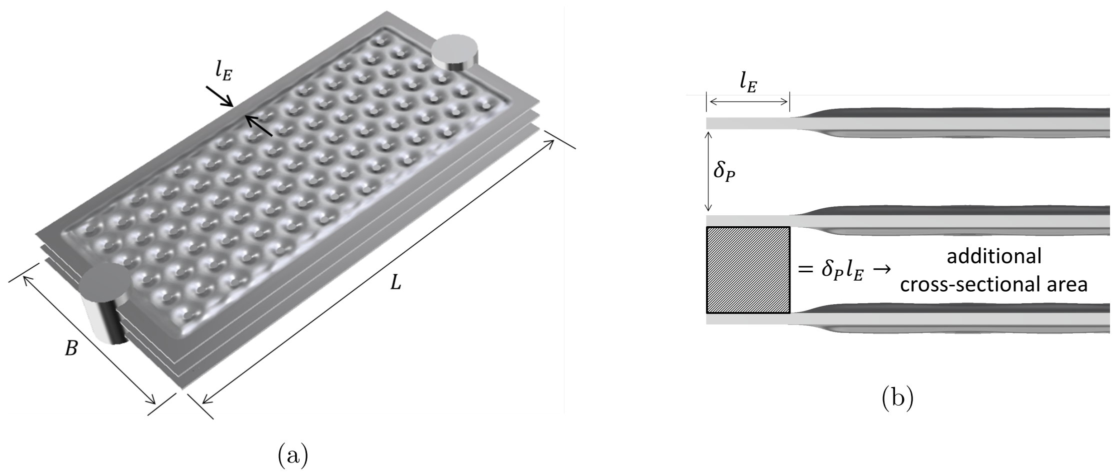

Figure 4.2: Global geometrical parameters of a pillow-plate stack (a) and additional cross-sectional area caused by the edges (b).

The outer channel volume is determined by subtracting the volumes of the metal sheet and the inner channel from the total volume:

$$\begin{aligned} V_o &= V_{tot} - V_i - V_P \\ &= \frac{1}{2} s_L s_T \left(\frac{1}{2}\delta_P + \delta_p \right) - V_i - A_{w,o}\delta_p \end{aligned} \tag{4.6}$$

The volume of the metal sheet is calculated by multiplying the outer surface area $A_{w,o}$ by the wall thickness. The outer surface area is equal to the inner surface area plus the surface area of the welding spots:

$$A_{w,o} = A_{w,i} + A_{SP} \tag{4.7}$$

The heat transfer area of the outer channel is set equal to the outer wall area:

$$A_{HT,o} = A_{w,o} \tag{4.8}$$

The mean hydraulic diameter of the outer channel is determined in the same manner as that of the inner one:

$$\bar{d}_{h,o} = \frac{4V_o}{A_{w,o}} \tag{4.9}$$

The mean cross-section of the outer channel is given by:

$$\overline{A}_{cs,o} = \frac{V_o}{s_L}. \tag{4.10}$$

The equations for the outer parameters are valid for the periodic element shown in Fig. 4.1. For the total cross-sectional area of the channel between two pillow plates, $\overline{A}_{cs,o}$ is multiplied by the number of elements along the total channel width B, including the cross-sectional areas of the edges (see Fig. 4.2(b)):

$$\overline{A}_{cs,o,tot} = \overline{A}_{cs,o} 4 \left(\frac{B - 2l_E}{s_T} \right) + 2l_E \delta_P \tag{4.11}$$

In most cases, the contribution of $2l_E\delta_P$ to the total cross-sectional area is negligible, e.g. for pillow-plate stacks of industrial dimensions. However, for smaller equipment, neglecting $2l_E\delta_P$ can result in an incorrect mean flow velocity. The total heat transfer area is obtained in a similar way:

$$A_{HT,o,tot} = 4A_{HT,o} \left(\frac{B - 2l_E}{s_T} \right) \left(\frac{L - 2l_E}{s_L} \right) \tag{4.12}$$

Notice that also in Eq. (4.12), the surface area of the edges is excluded. This is justified by the fact that in most cases, the edges contribute only marginally to overall heat transfer. Besides, in contrast to the welding spots, the edges have no characteristic dimensions, which may bring a larger uncertainty in their size evaluation. Similar to shell-and-tube heat exchangers, where the outer surface area of the tubes is used as the equipment characteristic area, here the use of $A_{HT,o,tot}$ is proposed as the characteristic heat transfer area for the thermo-hydraulic design of pillow plates.

4.2 Geometry generation by forming simulations

Forming simulations offer several important benefits. First, they imitate the hydroforming process during the real manufacturing of pillow plates and thus allow an accurate and predictive reconstruction of the wavy pillow-plate channels. This method can be used for all possible variations of the geometrical parameters. Second, information on local stresses and strains acting in the structure can be obtained. This permits the maximum allowable forming of the structure and subsequently the maximum height of the pillows to be determined for a given geometry and material properties. Structural changes in the material due to the manufacturing process are not accounted for by this method. The simulations were performed using the commercial Finite-Element-Analysis (FEA) tool Abaqus [49].

Since pillow plates represent a “shell-type” structure and it can be assumed that the stresses tangential to the pillow-plate surface are significantly larger than those in the direction normal to the wall, a thick shell approach was applied (Mindlin-Reissner-Theory, see Timoshenko [50]) to simulate the forming. Fig. 4.3(a) shows the choice of an appropriate periodic simulation element. In the shell approach, only the two-dimensional mid-surface ($z = 0$) is discretized by a numerical grid (cf. Fig 4.3(b)), while the stresses normal to this plane are modeled by a linear (first order) displacement variation according to the Mindlin-Reissner-Theory. Consequently, using the shell approach, the computational effort could be reduced by a factor of 8 compared to a full discretization (continuum approach) of the metal sheet in all three dimensions. As illustrated in Fig. 4.3(c), a structured grid was used in the vicinity of the welding spots and an unstructured grid in the remaining region. Local grid refinement was performed where necessary in order to resolve large gradients, e.g. in the vicinity of the welding spots. The total number of cells was approximately 10000. General purpose S4R large-strain elements were used, which are available in the Abaqus element library. These are quadrilateral elements with four integration points. These points are shifted using a linear displacement law. Furthermore, uniformly reduced integration is used to avoid shear and membrane locking. The simulation results obtained with the shell approach were compared with those obtained with the continuum approach; the differences in shear distribution and displacement were negligible.

The computational cost was further reduced by choosing the periodic simulation element in such a way that all possible planes of symmetry of the local stresses are utilized. Since the welding spots are fixed in space, a clamped support boundary condition with zero degree of freedom was applied (Fig. 4.3(c)). Symmetry boundary conditions were set at the edges. The forming is achieved by an evenly distributed area load, which imitates the hydroforming pressure. This load is applied to the surface of the simulation element, as indicated in Fig. 4.3(c).

In order to achieve quasi-steady-state and thus neglect visco-plastic effects, a very gradual slope was applied regarding the function of surface load vs. time. Consequently, the material behavior is modeled as elasto-plastic and isotropic. Hence, structural changes of the material, e.g. due to the welding process, were neglected. For the plastic part, the flow curves of various austenitic stainless steels (1.4301, 1.4404, 1.4541, 1.4571) were used. Differences in the forming behavior of the investigated materials proved to be negligible. This can be attributed to the fact that these alloys have the same elastic module and that their true stress-strain curves differ only slightly. Fig. 4.3(d) shows an example of a deformed pillow-plate element with the corresponding displacement magnitude in the z-direction.

4.3 Method validation and manufacturing limits

A validation of the method was carried out by comparing the simulated profiles at the symmetry planes with those of a real pillow-plate (see Fig. 4.4). The latter were measured using a contour gauge Contura G2 by Carl Zeiss AG. The deviation between the simulation and the measurement was less than 4%. The pillow profile at $x = 0$ in Fig. 4.4 illustrates the fact, that the maximum inflation height does not lie at the intersection between the longitudinal and transversal pitches (i.e. at $x = 0, y = 0$), but it is rather shifted towards the welding spot (y-direction) by a distance

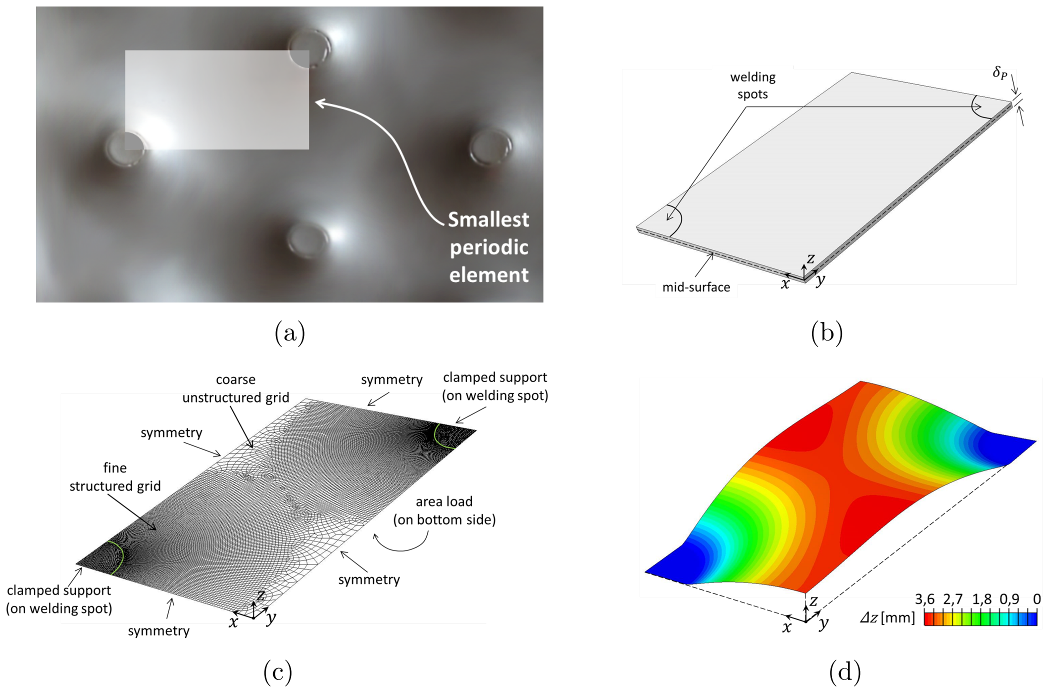

Figure 4.3: Choice of a periodic element for the forming simulations (a); illustration of the mid-surface for the shell approach (b); boundary conditions and grid types used in the simulations (c) and an example of the simulation result (d).

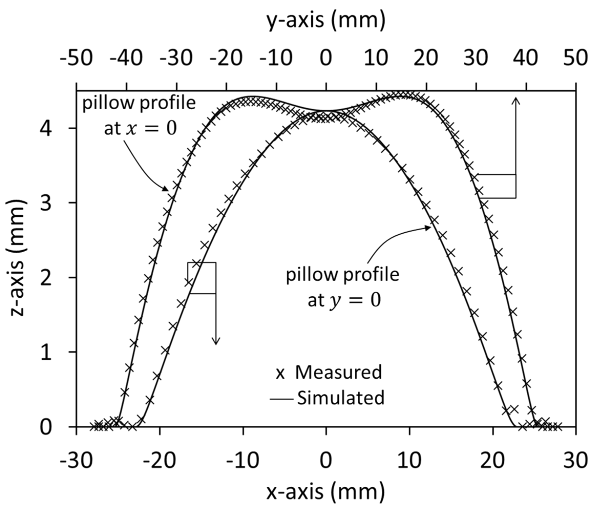

Figure 4.4: Comparison of numerical and measured cross-sectional profiles of the pillow-plate channel. Geometry: $s_T = 55\ mm$, $2s_L = 95\ mm$; $d_{SP} = 10\ mm$ and $\delta_i = 9\ mm$.

of $\approx s_L/3$ (center point of an equilateral triangle). The maximum inflation height of the pillows is limited by the value at which the metal sheets rupture. A crack in the pillows will be located in a region, where the local strain in the metal sheet exceeds the fracture strain.

To analyze the maximum allowable inflation height of pillow plates, forming simulations were performed using a continuum approach, instead of a shell approach, with second order shape functions and a clamped support boundary condition at the bottom surface ($z = -\delta/2$) of the welding spots. The result of these simulations is presented in Fig. 4.5. Fig. 4.5(a) shows the

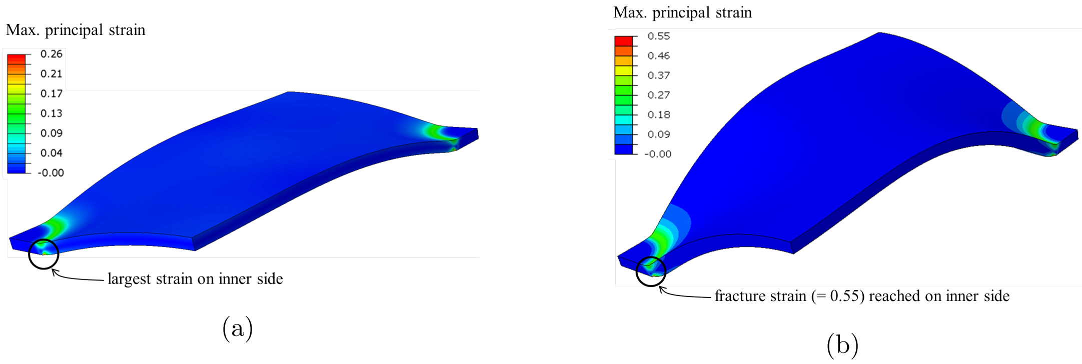

Figure 4.5: Local maximum principal strain field in the metal sheets of a pillow plate made of austenitic stainless steel (1.4301) for the pillow plate from the validation study with $\delta_i = 9$ mm (a) and with $\delta_i = 20$ mm (maximum inflation before rupture) (b).

field of the local strain in the metal sheets of the pillow plate, with the same geometry as the one used for the validation of the forming simulations (cf. Fig. 4.4). The pressure required to reach an inflation height δ_i of 9 mm was approximately 16 bar. The largest strain is located in the vicinity of the welding spots, which indicates the region, where the pillow plate could most likely rupture. This strain does not reach the fracture strain (= 0.55); however, it exceeds the uniform strain thus causing a necking of the metal sheet.

In Fig. 4.5(b), the pillow plate was further inflated up to the point of rupture, which occurred at the welding spots. The required pressure was approximately 24 bar, and the resulting critical inflation height δ_i was equal to 20 mm.

4.4 Geometrical design parameters

In this work, the essential parameters V_i and $A_{w,i}$ were determined based on forming simulations. These parameters are functions of the characteristic geometrical parameters d_{SP}, δ_i, s_T and s_L. In order to determine the dependence between V_i and $A_{w,i}$ and the characteristic parameters, a comprehensive numerical analysis was performed.

First, the influence of the inflation height δ_i was considered. In order to quantify the enlargement of the surface area due to the formation of pillows, the relative difference between the wetted wall area $A_{w,i}$ and the projection area $A_0 = 0.5 s_T s_L - \pi d_{SP}^2/8$ (plane surface) was considered. In Fig. 4.6 the inner volume and the wetted surface area enlargement are plotted against the inflation height, for different welding spot patterns. The simulation results show that the inner volume increases linearly and the wetted wall area increases quadratically with δ_i:

$$V_i \sim \delta_i \tag{4.13}$$

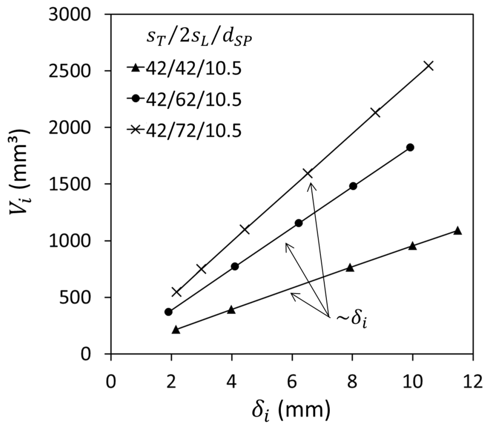

(a)

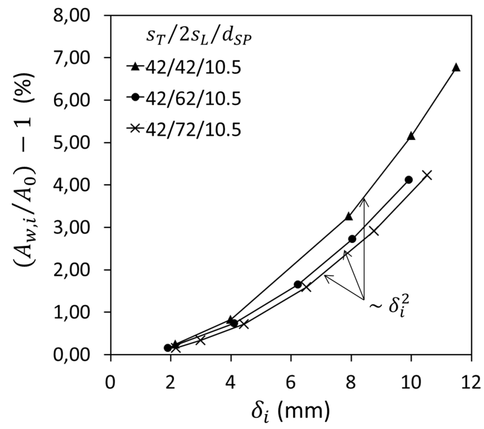

(b)

Figure 4.6: Inner volume (a) and inner wetted surface area enlargement (b) as functions of the inflation height for various welding spot patterns.

$$\left(\frac{A_{w,i}}{A_0} - 1\right) \sim \delta_i^2 \tag{4.14}$$

Fig. 4.6(b) shows that the surface area enlargement due to the surface waviness is marginal compared to the plane surface; it reaches values of only 7% even for large inflation heights. In Fig. 4.6(a), the slope of the lines (a_V) depends on s_L, s_T and d_{SP}. This dependence can be represented in a more convenient way by introducing dimensionless variables, such as the ratio $s_T/2s_L$. However, since this ratio delivers no information about the absolute value of the welding spot pitch, a further variable is required. This variable must account for up-scaling or down-scaling of pillow-plate geometries, i.e. in the case that s_T and s_L increase while the ratio $s_T/2s_L$ remains constant. A convenient scaling factor is represented by the diagonal welding spot pitch:

$$s_D = \sqrt{(0.5s_T)^2 + {s_L}^2} \tag{4.15}$$

The influence of the welding spot diameter can be represented by:

$$\phi_A = \frac{A_{PE} - A_{SP}}{A_{PE}} = \frac{0.5s_Ts_L - 0.125\pi d_{SP}^2}{0.5s_Ts_L} = 1 - \frac{\pi d_{SP}^2}{4s_Ts_L} \tag{4.16}$$

The quantity ϕ_A expresses the ratio of the base area of the periodic element in Fig. 4.7 excluding the welding spot areas ($A_{PE} - A_{SP}$) to the total base area A_{PE}.

The relationship between the inner volume V_i and s_D is derived by considering an example, in which a reference pillow plate with a volume $V_{i,ref}$, an inflation height $\delta_{i,ref}$, as well as a

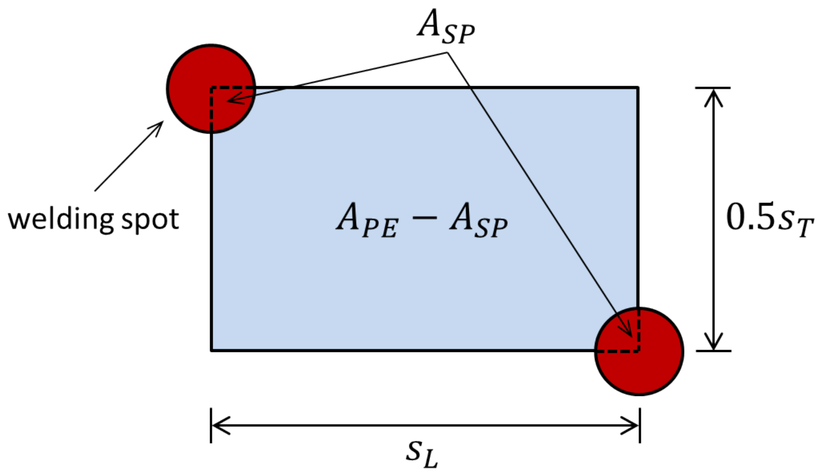

Figure 4.7: Illustration of the variable ϕ_A in Eq. (4.16)

welding spot arrangement $s_{L,ref}$, $s_{T,ref}$ and $d_{SP,ref}$, is up-scaled (stretched by central dilation) to a pillow plate with a volume V_i, an inflation height h_i and a welding spot arrangement s_L, s_T and d_{SP}. A central dilation yields:

$$\frac{V_i}{s_D^3} = \frac{V_{i,ref}}{s_{D,ref}^3} \tag{4.17}$$

$$\frac{\delta_i}{s_D} = \frac{\delta_{i,ref}}{s_{D,ref}} \tag{4.18}$$

Combining Eq. (4.17) and (4.18) gives:

$$V_i = \frac{V_{i,ref}}{\delta_{i,ref} s_{D,ref}^2} s_D^2 \delta_i = \alpha_{Vn,ref} s_D^2 \delta_i \tag{4.19}$$

Eq. (4.19) shows that $V_i \sim s_D^2$. The dimensionless coefficient $\alpha_{Vn,ref}$ is defined by $\alpha_{V,ref}/s_{D,ref}^2$. A similar analysis is also possible for the surface area enlargement:

$$\left(\frac{A_{w,i}}{A_0} - 1\right) = \left(\frac{A_{w,i,ref}}{A_{0,ref}} - 1\right) \tag{4.20}$$

$$\frac{\delta_i^2}{s_D^2} = \frac{\delta_{i,ref}^2}{s_{D,ref}^2} \tag{4.21}$$

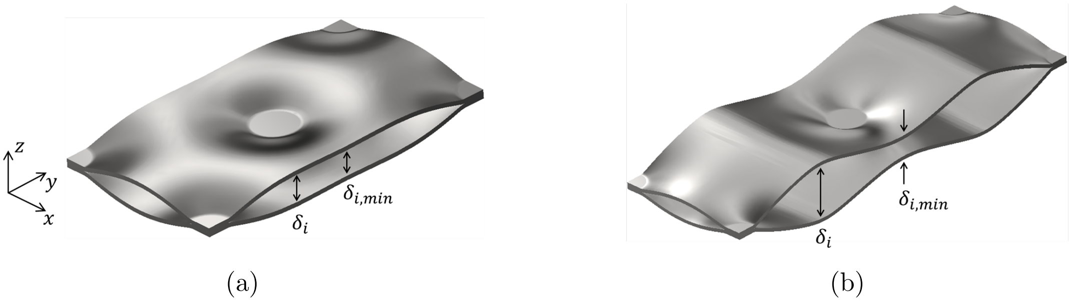

Figure 4.8: “Conventional” type I (a) and “untypical” type II (b) pillow-plate geometries.

The square of the inflation height is taken in Eq. (4.21), since the surface area enlargement is proportional to the square of δ_i (cf. Eq. (4.14)). Combining Eq. (4.20) and Eq. (4.21) gives:

$$\left(\frac{A_{w,i}}{A_0}-1\right)=\left(\left(\frac{A_{w,i,ref}}{A_{0,ref}}-1\right)\frac{s_{D,ref}^2}{\delta_{i,ref}^2}\right)\frac{\delta_i^2}{s_D^2}=\alpha_{wn,ref}\frac{\delta_i^2}{s_D^2} \tag{4.22}$$

From Eq. (4.22) it follows that the surface area enlargement is inversely proportional to the square of the scaling variable. For the factors $\alpha_{Vn,ref}$ and $\alpha_{wn,ref}$, expressions can be derived as functions of the welding spot ratio $s_T/2s_L$. The influence of the welding spot diameter in these functions is excluded by keeping ϕ_A constant. Furthermore, the limits of the ratio $s_T/2s_L$ should be considered while deriving the expressions for $\alpha_{Vn,ref}$ and $\alpha_{wn,ref}$. These limits are defined by the following conditions:

$$\frac{d_{SP}}{2s_L}<\frac{s_T}{2s_L}\leq 1 \tag{4.23}$$
$$\frac{d_{SP}}{s_T}<\frac{s_T}{2s_L}\leq 1 \tag{4.24}$$

The left inequality in Eqs. (4.23) and (4.24) follows from the condition at which the welding spots touch ($s_T = d_{SP}$), while the right inequality mirrors the symmetry condition ($s_T/2s_L = 1$). The range of the conditions in Eqs. (4.23) and (4.24) can further be reduced by considering Fig. 4.8.

Fig. 4.8(a) shows a typical pillow-plate section with a triangular welding spot pattern. On the other hand, Fig. 4.8(b) shows a pillow-plate section with an “untypical” surface waviness, which appears when the welding spots are moved too close to each other (in x-direction). In this case, the difference in the maximum and minimum inner inflation heights δ_i and $\delta_{i,min}$ becomes large. As a consequence, the variation of the cross-section along the y-coordinate is large, whereas it is almost constant along the x-direction. Technically relevant pillow-plate geometries are close to the type shown in Fig. 4.8(a). In order to identify the transition point between pillow-plate geometries of typical and untypical surface waviness, the factors $\alpha_{Vn,ref}$ and $\alpha_{wn,ref}$ were plotted over the welding spot ratio $s_T/2s_L$ (Fig. 4.9).

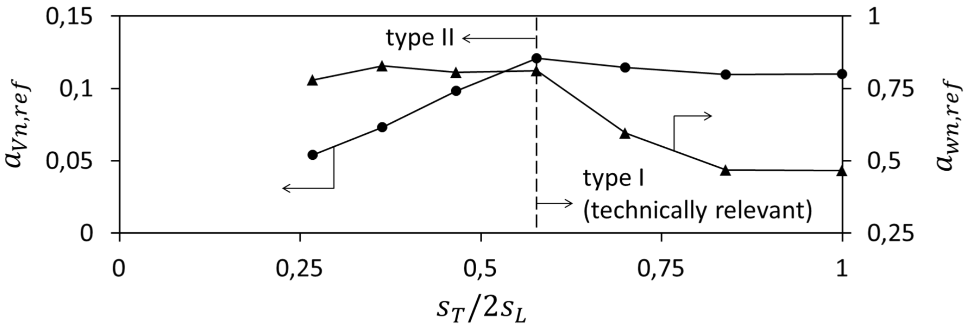

Figure 4.9: Identification of the critical ratio $s_T/2s_L$, where the pillow-plate geometry varies from type I to type II waviness. The diagram is valid for constant ϕ_A.

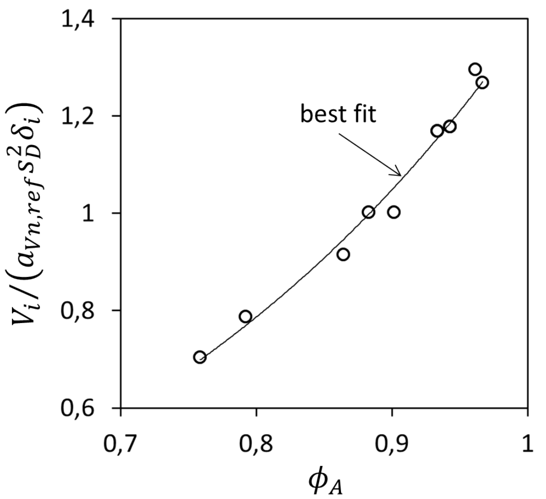

Figure 4.10: Influence of the welding spot diameter (represented by ϕ_A) on the inner volume V_i.

Notice the change in the curves at $s_T/2s_L \approx 0.57$, which corresponds to a triangular welding spot pitch. This change indicates the transition in the waviness of the pillow-plate surface from type I to type II, as can be seen in Fig. 4.8. When the ratio of $s_T/2s_L$ becomes smaller than that of the triangular pitch, the waviness of the pillow-plate surface becomes untypical. The range of interest is thus reduced to $0.57 \leq s_T/2s_L \leq 1$. This technically relevant range is described by the following polynomials obtained by fitting the factors $\alpha_{Vn,ref}$ and $\alpha_{wn,ref}$ to the results of the forming simulations:

$$\alpha_{Vn,ref} = 0.1\left(\frac{s_T}{2s_L}\right)^2 - 0.18\left(\frac{s_T}{2s_L}\right) + 0.19 \tag{4.25}$$

$$\alpha_{wn,ref} = 3.12\left(\frac{s_T}{2s_L}\right)^2 - 5.74\left(\frac{s_T}{2s_L}\right) + 3.08 \tag{4.26}$$

Now only the influence of the welding spot diameter on V_i and $A_{w,i}$ must be determined. This is done by plotting $V_i/\left(\alpha_{Vn,ref}s_D^2\delta_i\right)$ against ϕ_A (cf. Fig. 4.10).

The best fit of the data is given by the following power law:

$$f_{SP} = 1.37\,{\phi_A}^{2.58} \tag{4.27}$$

The factor f_{SP} is used in the following Equation to account for the welding spots:

$$V_i = \alpha_{Vn,ref}\delta_i s_D^2 f_{SP} \tag{4.28}$$

The simulation results show that variations in the welding spot diameter affect the ratio $A_{w,i}/A_0 - 1$ only marginally, so that the surface area enlargement can be evaluated from Eq. (4.22).

In summary, the inner hydraulic diameter of pillow plates can be determined by Eqs. (4.1), (4.22) and (4.28). The outer hydraulic diameter is evaluated by Eqs. (4.6), (4.7), (4.9), (4.22) and (4.28). The inner and outer hydraulic diameters determined using the above equations, show a maximal deviation of 5% from the values obtained by the forming simulations.

4.5 Conclusions

In this chapter, a novel method for accurately reconstructing the complex pillow-plate surface was presented. It is based on forming simulations (FEA), which imitate the hydroforming process during the real manufacturing of pillow plates. A validation of the method was carried out by comparing the simulated wavy profiles of the pillow plates with those of a real pillow plate, measured using a contour gauge. The deviation between the simulation and the measurement was less than 4%. Furthermore, the numerical results showed, that the surface area enlargement caused by the surface waviness is marginal compared to a plane surface ($2 - 7\%$).

The results from the forming simulations were then used to develop simple equations for the predictive, accurate determination of the geometrical design parameters: mean hydraulic diameter, mean cross-sectional area and heat transfer area for the inner channel of a pillow plate and for the channel between adjacent pillow plates.

5 Fluid dynamics and heat transfer in pillow plates

The study of the flow in the inner channels of pillow-plate heat exchangers is divided into two parts, namely, an experimental and a numerical (CFD simulation) part. The latter formed the bulk of this work, whereas the experiments were mainly used for validation purposes and for the investigation of flow regimes not easily resolvable with CFD (e.g. transitional flow regime).

5.1 Experimental study

The experimental study deals with two different aspects. The first focuses on flow visualization in pillow-plate channels. It enables a comparison between the flow patterns observed experimentally and obtained by CFD simulations. The second considers the measurement of pressure loss and heat transfer coefficients. With these experiments it becomes possible to validate the numerical model both qualitatively and quantitatively.

5.1.1 Flow visualization in a transparent pillow-plate channel

Flow visualization in heat exchangers by setting-up transparent replicas has been widely reported in literature. However, there are no publications on flow visualization in pillow-plate channels or even in some comparable geometry. Therefore, in this work, a unique experimental rig was developed, facilitating a transparent pillow-plate channel.

Fabrication of the transparent pillow-plate channel

The transparent test section of the experimental facility (Fig. 5.1 (top)) was composed of two-halves (Fig. 5.1 (middle)), which are combined to form a transparent pillow-plate channel. Each of these channel halves was fabricated by casting a resin into a specially designed aluminum

A part of the material presented in this chapter has been published in Piper et al. [51].

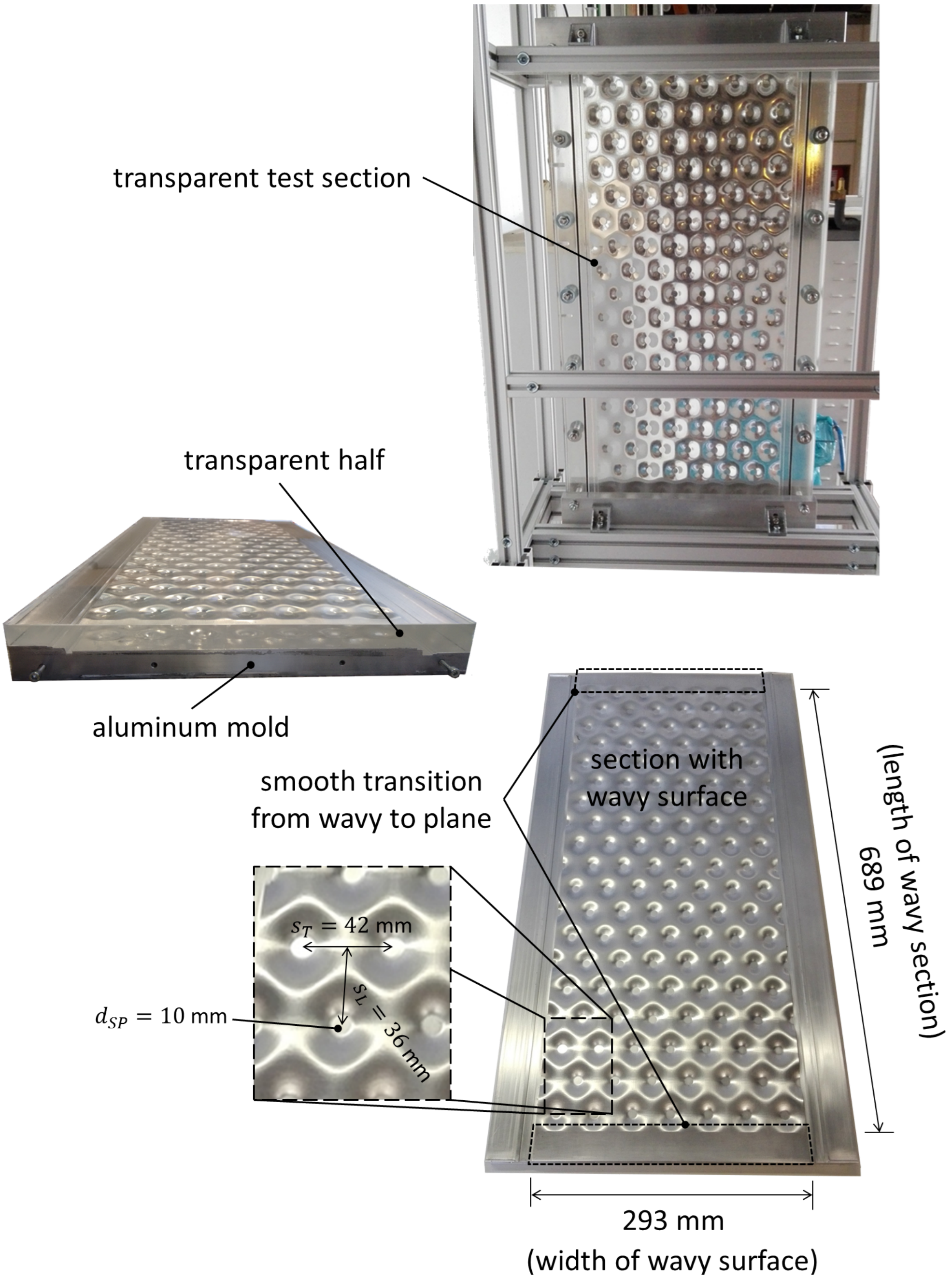

Figure 5.1: Photo of the transparent pillow-plate test-channel (top) and of the aluminum mold (middle and bottom) used to cast the transparent section.

mold. This mold is depicted in Fig. 5.1 (bottom). It was manufactured using a high precision CAD/CAM milling machine, which produced an accurate surface corresponding to the original geometry of the CAD image. The average surface roughness was $R_z = 3.2\mu m$ (peak-to-valley height). The CAD image was created using forming simulations (cf. Chap. 4) to accurately reproduce the real pillow-plate surface.

The wavy section of the channel has a length of 689 mm ($= 19s_L$) and a width of 293 mm ($= 7s_T$), as shown in Fig. 5.1 (bottom). It was chosen long enough to guarantee hydrodynamically fully developed flow, and wide enough to reduce the influence of side effects. The dimensions of the

Table 5.1: Physical properties of the saturated NaSCN aqueous solution (ca. 55 Mass%) at $20°C$.

ρ_{sol} (kg/m^3)	1340
μ_{sol} (Pas)	0.0075
refractive index	1.48 (same as polyurethane resin)

characteristic geometrical parameters of the transparent pillow-plate channel are: $s_T = 42$ mm, $2s_L = 72$ mm, $d_{SP} = 10$ mm and $\delta_i = 6$ mm. At the channel inlet and outlet, the surface smoothly transitions from wavy to plane. The channel height at the inlet and outlet regions was chosen in such a way that the resulting cross-sectional area is equal to the mean cross-sectional area of the wavy channel section. Extrusions were incorporated along the sides of the wavy section of the mold in order to create grooves in the cast resin. These grooves accommodate rubber gaskets for sealing the transparent channel at the sides.

The following requirements specification were chosen for the cast resin:

- full transparency
- high structural stability
- molding accuracy, i.e. high degree of reproducibility of geometrical features
- negligible contraction (volume reduction) after solidification
- low refractive index (favorable index-matching properties)
- thermal and chemical stability
- Resistance to ultraviolet light (UV)

All requirements were met by the polyurethane-based resin *Crystal Clear 204* (www.smooth-on.com). Its refractive index has a value of 1.48.

Experimental set-up

The closed-loop experimental facility used for flow visualization in a pillow-plate channel is shown in Figs. 5.2 and 5.3.

A NaSCN aqueous solution (Tab. 5.1) is promoted through the thermostat (TS), followed by the Coriolis flow meter (F; Emerson Micro Motion® CMF050), then the manual needle valve (NV) and finally to the flow distribution channel (DC), by the centrifugal pump (P). The specific working fluid was chosen because it had the same refractive index as the polyurethane resin, and also because it's viscosity was low enough for reaching high Reynolds numbers. The TS is used to keep the temperature of the solution at $T = 20°C$, while the NV is used to adjust the volumetric flow rate. The optimal angle γ of the DC was determined using CFD simulations. The DC is followed by the entry length channel (EC), in which the flow develops hydrodynamically before entering the transparent test section (TC). The width and height of the EC were perfectly adapted to the width and height of the plane entry section of the TC (cf.

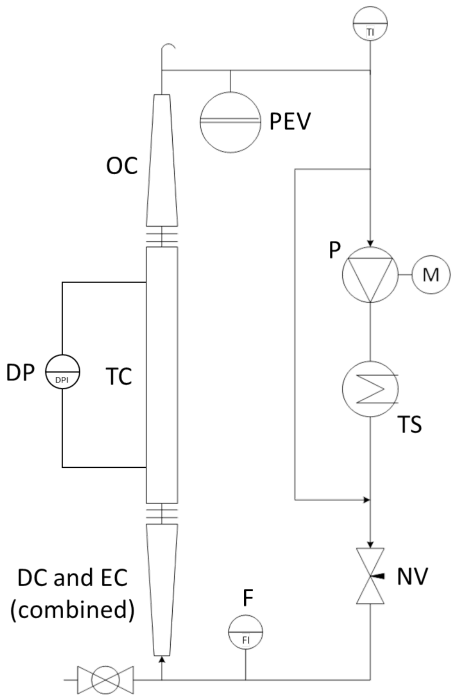

Figure 5.2: Process flow diagram of the experimental set-up housing the transparent test channel.

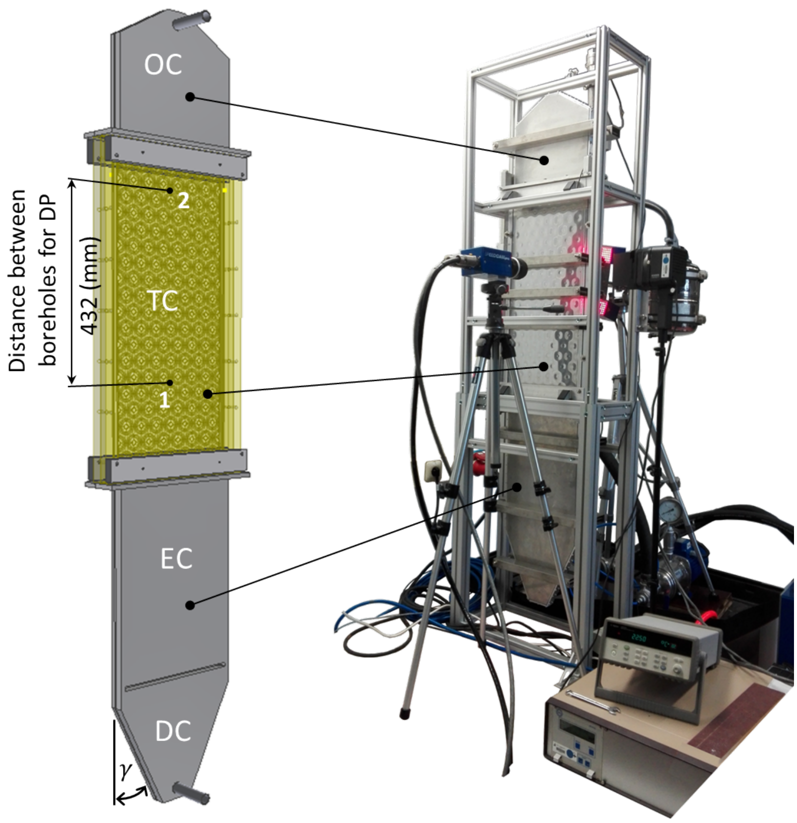

Figure 5.3: CAD image of the transparent test section (left) and photo of the experimental facility (right).

Table 5.2: Range of Reynolds numbers and corresponding volumetric flow rates and mean stream velocities, which were used in the experiments.

Re	$\dot{V}$	u_m
-	m^3/h	m/s
50	0.128	0.029
100	0.256	0.059
200	0.512	0.118
500	1.28	0.295
1000	2.56	0.59
1500	3.84	0.884

Fig. 5.1 (bottom)). Consequently, EC and TC have the same cross-sectional areas, thus avoiding flow acceleration. Subsequently, the flow passes through an outlet channel (OC) followed by the pressure equalization vessel (PEV), which is designed to damp any flow disturbances. After the PEV the flow goes back to the centrifugal pump, thus closing the loop.

The flow was visualized by adding Polymethylmethacrylate (PMMA) tracer particles with a mean diameter of $40\mu m$ to the NaSCN aqueous solution. Photos of the flow in the transparent test section were taken at a position $12s_T$ from the channel inlet using a digital, single-lens reflex camera. The exposure time of the camera was adjusted according to the fluid velocity, so that it was possible to capture streamlines of the flow. The range of Reynolds number used in the experiments is given in Tab. 5.2.

Results and discussion

Figure 5.4 shows a photo of the flow in the transparent pillow plate channel for $Re = 1500$. The flow pattern is sub-divided into two distinct regions, namely, recirculation zones, which arise in the wake of the welding spots, and a core flow, which follows a meandering path as it is deflected by the welding spots. The recirculation zones consist of two counter-rotating vortices, which together form a large, flame-like shaped region, approximately $4d_{SP}$ long and $3d_{SP}$ across. Boundary layer separation from the welding spot occurs at an angle of about $\beta \approx 50°$.

The development of the flow pattern in pillow plates with increasing Reynolds number is shown in the series of photos in Fig. 5.5. At the lowest Reynolds number, $Re = 50$, the flow is in the creeping regime. It fully follows the contours of the pillow-plate channel. The rise of recirculation zones in the wake of the welding spots is first observed at $Re = 100$. These zones grow in size with further increase of Re; they reach their final form and dimensions at $Re = 1500$. Up to $Re < 500$, the flow remains largely laminar, i.e. no strong fluctuations (high frequency) of the tracer particles lateral to the flow could be observed. A transition from laminar to turbulent could be seen around $Re = 500$, which was characterized by stronger oscillations of the recirculation zones as compared to the flow at other Reynolds numbers.

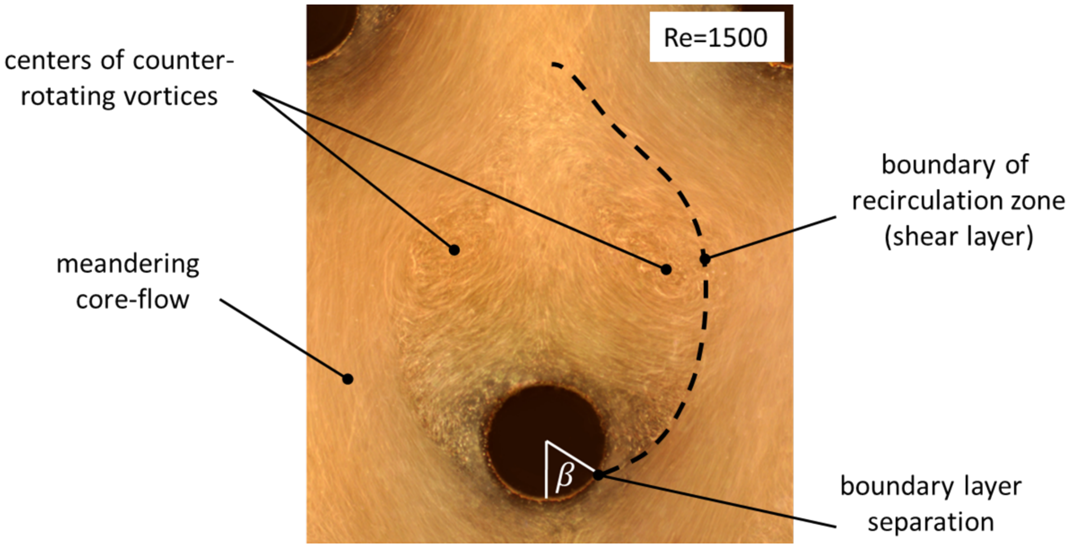

Figure 5.4: Photo of the flow in the transparent pillow-plate channel for $Re = 1500$.

5.1.2 Pressure loss and heat transfer measurements

Two different experimental facilities were used to measure pressure loss in pillow plates. The first one was described in Sec. 5.1.1 (Fig. 5.3). The second one is shown in Fig. 5.6(a). Its detailed description is given in [52, 9]. The pillow-plate used in the second test-rig (Fig. 5.6) has the characteristic dimensions 72/42/3/10 (cf. Tab. 5.3). It shares the same welding spot arrangement as the transparent channel in Sec. 5.1.1, but only half the inner inflation height. It was manufactured from austenitic stainless steel plates of material 1.4541 (AISI 321), with a surface finishing of quality 2B (DIN EN 10088-2), which has a typical mean roughness $R_a \approx 0.1 - 0.5\,\mu$m. This surface is technically smooth, hence the effect of surface roughness on frictional losses is assumed to be negligible.

In both experimental set-ups, pressure loss was measured between two measuring ports (ports 1 and 2 in Fig. 5.3 and 5.6) using differential pressure transmitters (DP; Emerson Rosemount 3051 CD2 and CD3). The measuring ports were placed far enough from the inlet and outlet. In this way, only the fully developed flow region was considered. The ports were made by drilling bore holes of 1 mm (2 mm for the test-rig in Fig. 5.6) in diameter through the pillows, directly at the center-point of the equilateral triangle formed by three neighboring welding spots in triangular arrangement (cf. Fig. 5.6(b,c)). The distance between the two ports was equal to twelve-fold the longitudinal welding spot pitch (i.e. 432 mm) for the test-rig described in Sec. 5.1.1, and 288 mm ($8s_L$) for the facility shown in Fig. 5.6. The pressure loss measurement was performed under isothermal conditions using water at $T = 25\,°C$ as a working fluid in both facilities.

Heat transfer coefficients were evaluated using the experimental set-up shown in Fig. 5.6. The procedure for evaluating the heat transfer coefficients is described in [9]. The total relative uncertainties for pressure drop are below 2% and for the heat transfer coefficients below 3%, at a confidence level of 95% (cf. [52]). Systematic uncertainties in temperature, pressure and flow measurements were minimized by calibration of the measuring chains, covering the whole range of operation.

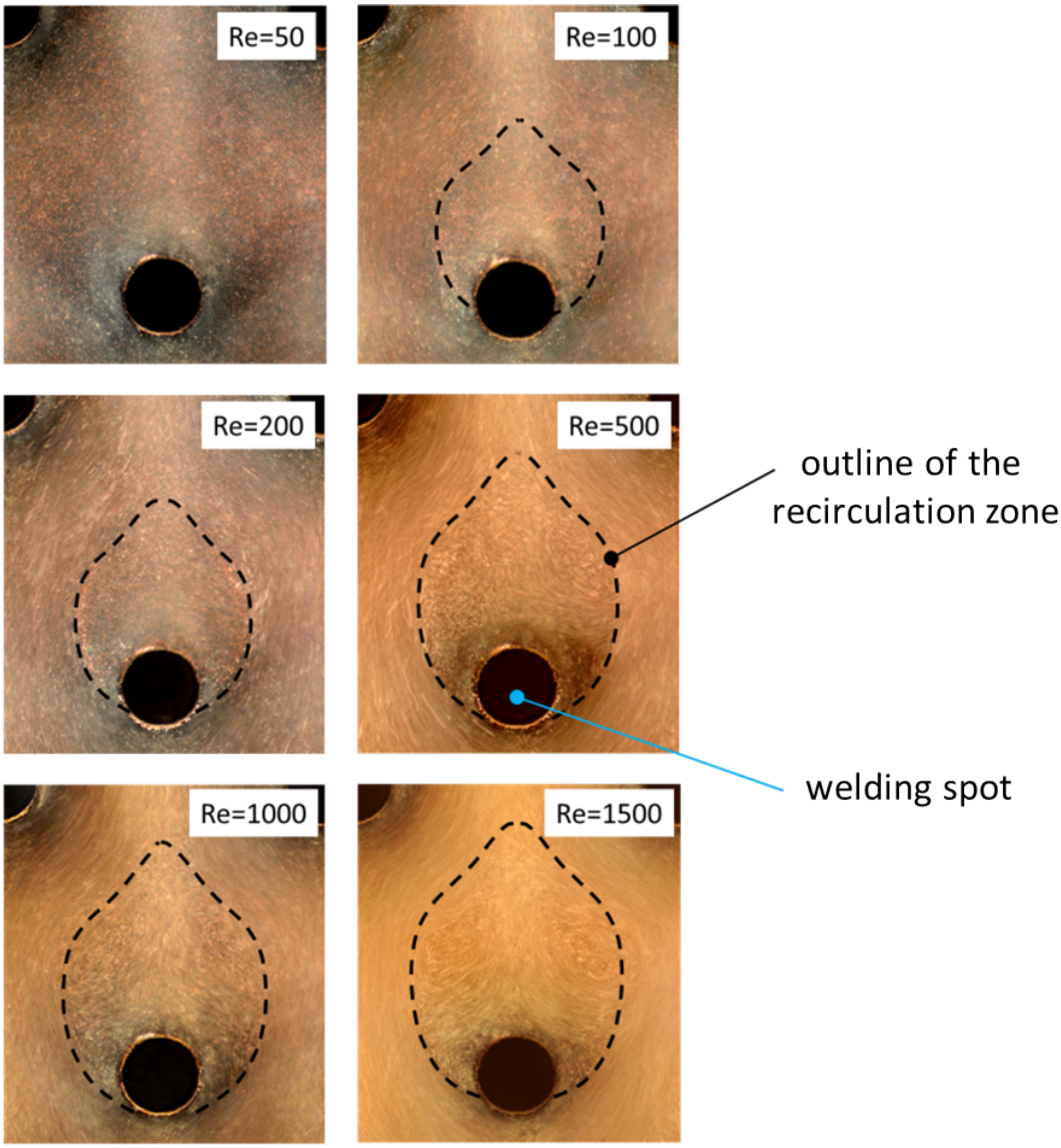

Figure 5.5: Photos of the flow in the transparent pillow-plate channel showing the development of the flow pattern with growing Reynolds number.

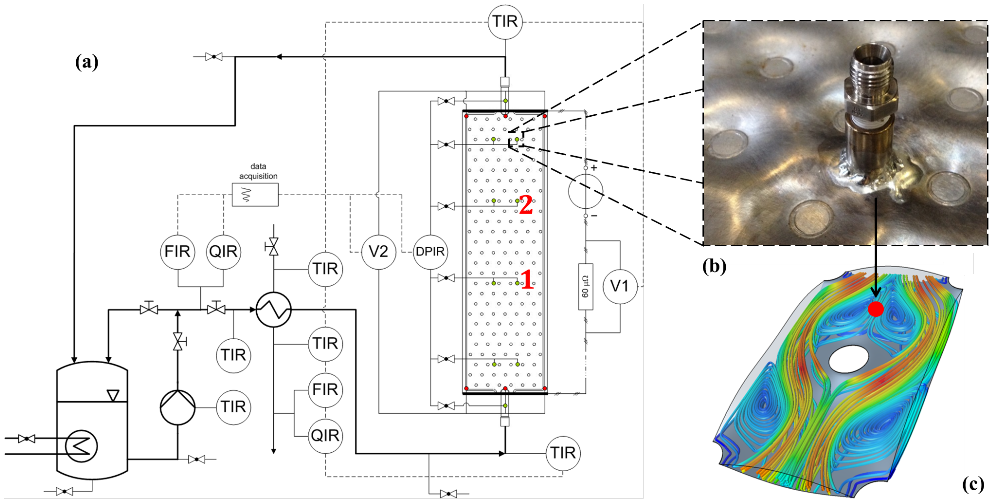

Figure 5.6: Flow sheet of the second experimental facility used for the measurement of pressure loss and evaluation of heat transfer coefficient inside pillow plates (a) (see also [9]). Photo of the pressure measurement ports (b), and ideal location of these ports as determined by CFD (c).

5.2 CFD study

Fluid flow and heat transfer in the inner pillow-plate channels was studied in detail using CFD simulations. They provide comprehensive flow information, which cannot be readily obtained in experiments. As mentioned in Sec. 3.4, CFD simulations also require significantly less time and costs compared to experiments, especially when considering that the variability of the characteristic geometry parameters (Fig. 2.4) of pillow plates is practically unlimited.

For the CFD simulations, a digital image of the pillow-plate geometry that defines the boundaries of the simulation domain is required. The prerequisite for the realistic description of the fluid dynamics in pillow plates is an accurate reconstruction of the pillow-plate channel. This was done by forming simulations described in Sec. 4.2.

The pillow plates generated and investigated in this work are summarized in Table 5.3. The welding spot pattern can be characterized in dimensionless form by the following parameter:

$$s_r = \frac{2s_L - d_{SP}}{s_T - d_{SP}} \tag{5.1}$$

This parameter is equal to one for an equidistant welding spot pattern ($2s_L - d_{SP} = s_T - d_{SP}$), smaller than one for a *transversal* pattern ($2s_L - d_{SP} < s_T - d_{SP}$) and greater than one for a *longitudinal* pattern ($2s_L - d_{SP} > s_T - d_{SP}$).

The hydraulic diameter d_h is determined according to the method proposed in Sec. 4. The pillow-plate 72/42/3/10 (cf. Tab. 5.3), used in the experimental set-up (see Fig. 5.6) represents the reference geometry in this work. It has a typical triangular welding spot arrangement, with $\arctan(2s_L/s_T) \approx 60°$, which is a pattern commonly found in industry. All other values of s_T,

Table 5.3: List of investigated pillow-plate geometries

$2s_L$	s_T	δ_i	d_{SP}	d_h	s_r	Abbreviation
mm	mm	mm	mm	mm	-	
42	72	3	10	4.43	0.52	42/72/3/10
42	72	4.5	10	6.55	0.52	42/72/4.5/10
42	72	6	10	8.57	0.52	42/72/6/10
42	72	6	8.6	8.89	0.53	42/72/6/8.6
42	72	6	7.2	9.13	0.53	42/72/6/7.2
42	57	3	10	3.84	0.68	42/57/3/10
42	57	6	10	7.31	0.68	42/57/6/10
42	42	3	10	3.37	1.0	42/42/3/10
42	42	6	10	6.32	1.0	42/42/6/10
42	42	6	7.2	7.18	1.0	42/42/6/7.2
50	42	6	10	6.72	1.25	50/42/6/10
57	42	6	10	7.31	1.47	57/42/6/10
60	42	3	10	3.99	1.56	60/42/3/10
60	42	6	10	7.52	1.56	60/42/6/10
64	42	3	10	4.24	1.69	64/42/3/10
64	42	6	10	8.07	1.69	64/42/6/10
68	42	3	10	4.38	1.81	68/42/3/10
68	42	6	10	8.36	1.81	68/42/6/10
72	42	3	10	4.43	1.94	72/42/3/10
72	42	4.5	10	6.55	1.94	72/42/4.5/10
72	42	6	10	8.57	1.94	72/42/6/10
72	42	6	8.6	8.89	1.90	72/42/6/8.6
72	42	6	7.2	9.13	1.89	72/42/6/7.2

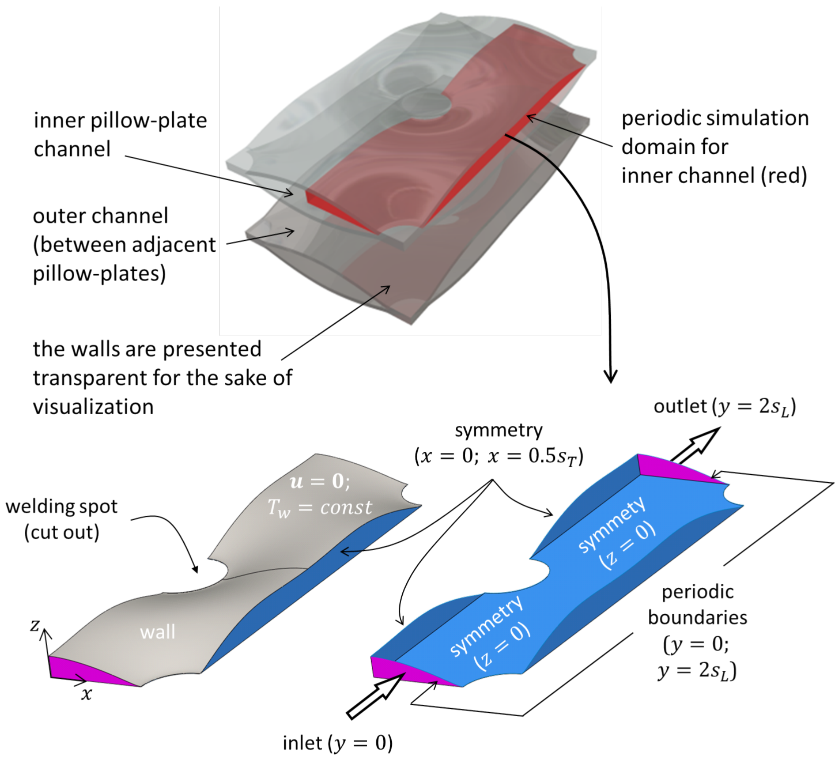

Figure 5.7: Periodic computational domain of the pillow-plate channel.

s_L, d_{SP} and δ_i presented in Tab. 5.3 are systematic variations of 72/42/3/10, e.g. s_T and s_L are interchanged or the inflation height δ_i is doubled.

5.2.1 CFD simulation

The CFD simulations were performed using the commercial solver STAR-CCM+ (see Sec. 3.4). The computational domain for the inner channel is illustrated in Fig. 5.7. The computational effort was reduced by exploiting all existing symmetries of the flow. A similar domain was used in [17]; however, in the present work the domain could be further reduced by utilizing the flow periodicity. This was accomplished by applying periodic boundary conditions at the inlet and outlet boundaries of the channel. In this way, the velocity field is repeated after twice the longitudinal pitch ($2s_L$), which offers the advantage of limiting the investigation to the (periodically) hydrodynamically developed region. In industrial-scale pillow-plate heat exchangers, such regions usually occupy a major part of the channels.

Thermally developed flow is characterized by a constant heat transfer coefficient in flow direction ($h = f(y) = const$). In STAR-CCM+, this is achieved by scaling the self-similar temperature profiles at the inlet and outlet boundaries (only), in such a way that the heat transfer coefficient at these boundaries is the same. At the walls, a no-slip boundary condition ($\mathbf{u} = \mathbf{0}$) was applied and a constant wall temperature ($T_w = const$) was assumed. The latter appears reasonable, because a major application area of PPHE is condensation, e.g. as top condensers in distillation columns, for which this boundary condition is nearly fulfilled.

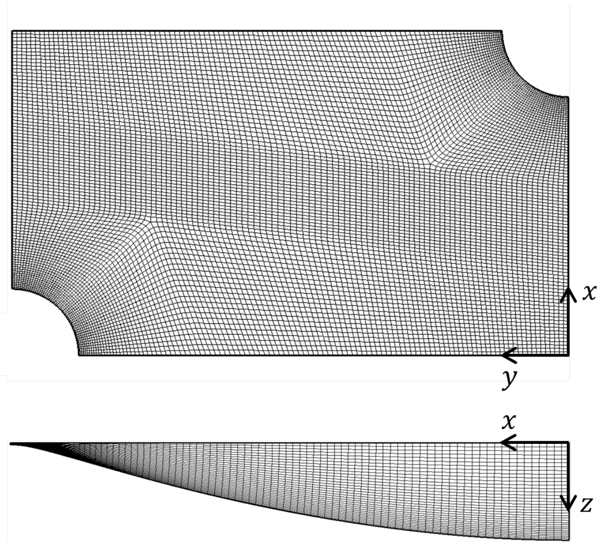

Figure 5.8: Example of structured body-fitted grid used in the simulations. The grid here is extra coarse for illustration purposes.

The flow considered was single-phase, incompressible, steady-state, three-dimensional and turbulent, with constant physical properties. Turbulence was described statistically by the Reynolds-Averaged-Navier-Stokes (RANS) equations (cf. Sec. 3.3.1). The Reynolds stresses were computed using the realizable $k - \epsilon$ model described in Sec. 3.3.2 and available in STAR-CCM+. It has been applied successfully to complex geometries, such as structured packings (e.g. [53, 54]) as well as plate [55] and shell-and-tube heat exchangers [56]. This choice was beneficial, as shown later in Sec. 5.2.3, where pressure loss and heat transfer coefficients obtained using this model agreed well with experiments.

Since flow separation was expected to occur in the pillow-plate channel, it was necessary to resolve the boundary layers appropriately. This was accomplished by using a two-layer formulation (cf. Sec. 3.3.3), which allows the application of the turbulence model also in the viscosity dominated region.

Figure 5.8 shows an example of the mesh used in this work for the simulation of fluid flow and heat transfer in the inner pillow-plate channels. It is a structured body-fitted mesh with hexahedral cells. This grid type is most suitable for wavy geometries, since the cells align with the geometry contours, e.g. in the vicinity of the welding spots (in the $x - y-$plane in Fig. 5.8) and close to the wavy channel wall. This leads to good cell quality, which shows substantially better numerical accuracy and convergence than block structured or even unstructured grids. A grid-independence study was considered in order to ensure an adequate grid resolution. This study was always performed for the highest Reynolds number ($Re = 8000$) in each geometry. It was assumed that the grid resolution sufficient for $Re = 8000$ would also be sufficient for the lower Reynolds numbers. Depending on the geometry, the total cell number could reach 15 million cells.

For properly resolving the boundary layers (cf. Sec. 3.3.3), the following steps were undertaken when constructing the grid:

- The distance between the wall and the grid node closest to it was estimated using the dimensionless wall coordinate z^+ (Eq. (3.41)) of the inner region of the turbulent boundary layer. The grid node adjacent to the wall had a value $z^+ < 1$.

- At least 3-4 cells are present in the viscous sub-layer ($0 \leq z^+ \leq 5$), in order to resolve this region properly, ensuring a smooth transition to the buffer layer.
- The cell thickness ($\Delta\tilde{z}_k$) increased linearly ("stretched") in direction normal to the wall. The stretching factor ($= \Delta\tilde{z}_{k+1}/\Delta\tilde{z}_k$) was set to a value of about 1.1.

Also the ratio of the length of cell edges in flow direction ($\Delta\tilde{x}_k$) to the thickness $\Delta\tilde{z}_k$ (cell aspect ratio: $\Delta\tilde{x}_k/\Delta\tilde{z}_k$) was kept low in the simulations, to avoid excessive numerical diffusion.

In the simulations of heat transfer with $Pr \gg 1$, the conduction layer is thinner than the viscous sub-layer (cf. Sec. 3.3.3). Hence, a smaller z^+ value for the grid node adjacent to the wall was used. For large Prandtl numbers, the thickness of the conduction layer ($z^+_{\vartheta,\delta}$) was approximately determined by the following relation [6]:

$$z^+_{\vartheta,\delta} = 15Pr^{-1/3} \tag{5.2}$$

5.2.2 Process parameters definitions

For the evaluation of thermo-hydraulic characteristics of the flow in pillow plates, several process parameters are introduced. The mean Reynolds number of the flow in the pillow-plate channel is defined using the following expression:

$$Re = \frac{u_{char} l_{char}}{\nu} \equiv \frac{u_m d_h}{\nu} \tag{5.3}$$

The characteristic velocity u_{char} is represented by the y-component of the mean velocity in the channel. As the characteristic length l_{char}, the hydraulic diameter of the channel determined by the methods proposed in Sec. 4.4 is taken.

The pressure loss coefficient is evaluated by the Darcy-Weisbach equation (see Eq. (3.27)):

$$\zeta_{\Delta p} = \frac{2 d_h \Delta p}{\rho u_m^2 2 s_L} \tag{5.4}$$

Pressure loss is calculated from the difference between the surface-averaged pressure values at the inlet and outlet boundaries. The hydraulic Fanning factor is determined using the surface-averaged wall shear stress:

$$\zeta_R = \frac{8\tau_w}{\rho u_m^2} \tag{5.5}$$

The form drag coefficient is obtained by subtracting Eq. (5.5) from Eq. (5.4):

$$\zeta_D = \zeta_{\Delta p} - \zeta_R \tag{5.6}$$

The Nusselt number is defined by,

$$Nu = \frac{h_m d_h}{\lambda} \tag{5.7}$$

where h_m represents the surface-averaged heat transfer coefficient:

$$h_m = \frac{\dot{q}_m}{T_w - T_m} \tag{5.8}$$

In Eq. (5.8), $\dot{q}_m$ is the heat flux in the direction normal to the wall and T_m is the adiabatic mean temperature in the channel evaluated under the assumption of constant physical properties as follows:

$$T_m = \frac{\int\limits_{A_{cs}} uT \, \mathrm{d}A}{\int\limits_{A_{cs}} u \, \mathrm{d}A}. \tag{5.9}$$

Here A_{cs} denotes the cross-sectional area. In order to consistently compare computed and measured heat transfer coefficients, T_m was used instead of the temperature T_{sym} at the channel axis (symmetry plane $(x, y, 0)$), since usually only T_m is experimentally accessible, especially in complex geometries.

5.2.3 Method validation

Figure 5.9 shows a comparison of the flow pattern in pillow plates obtained experimentally (cf. Sec. 5.1.1) and by CFD simulations for $Re = 1500$. The simulations are capable of accurately predicting the size and shape of the recirculation zones. This demonstrates that the CFD model is able to capture the complex fluid dynamics in the pillow-plate channel properly.

In Fig. 5.10(a), specific pressure loss determined by CFD simulations for two different pillow-plate geometries is compared with experimental values obtained in [52] and in this work using the experimental set-up housing the transparent pillow-plate channel, as described in Sec. 5.1.1 and 5.1.2. The numerical and experimental results agree well over the entire studied Reynolds numbers range ($1000 \leq Re \leq 8000$) for both geometries (72/42/3/10 and 72/42/6/10 (cf. Tab. 5.3)). The relative deviation is below 8%.

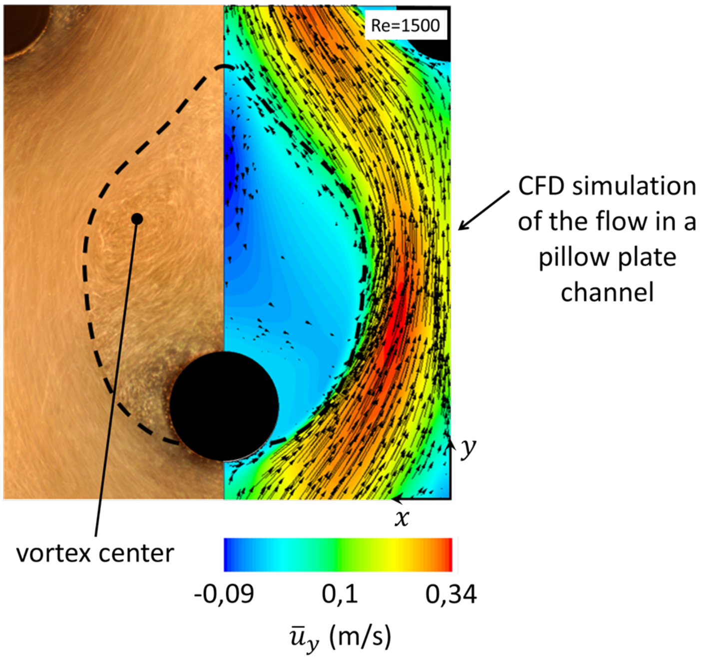

Figure 5.9: Comparison of flow patterns obtained by CFD and by flow visualization in the transparent channel (Sec. 5.1.1).

For the comparison of Nusselt numbers, a constant wall heat flux boundary condition ($\dot{q}_w = const$) was used instead of the constant wall temperature mentioned above. This was done, because in the experiments the pillow-plate wall was heated electrically (cf. [52]). Nusselt numbers determined using $\dot{q}_w = const$ are approximately 6% higher than those determined with $T_w = const$. For fully developed turbulent flow in pipes and other simple channel geometries, no difference in Nusselt numbers determined either with constant heat flux or constant temperature at the walls could be found (see, e.g., [57]); in contrast, in pillow plates, the deviation possibly originates from the recirculation zones, which are heated up more strongly when $\dot{q}_w = const$ applies. This is illustrated later in Fig. 5.12(a).

In Figs. 5.10(b) and 5.10(c), a comparison of simulated and experimentally determined Nusselt numbers is shown. Fig. 5.10(b) gives it for $Pr = 6$ and varied Reynolds number, whereas Fig. 5.10(c) for $Re = 4000$ and varied Prandtl number. In both figures, a good agreement is visible.

5.2.4 Results and discussion

Fluid dynamics and heat transfer in pillow plates

The presence of welding spots in pillow-plate channels and the waviness of the channel walls lead to a strong deflection of the flow and to the rise of pronounced secondary-flow effects, as shown in Fig. 5.11.

In the immediate vicinity of the spots, the channel is narrowest, leading to a large flow resistance. As the result, the fluid is directed away from the welding spots in radial direction, thus producing large regions of recirculating fluid behind them. The primary flow is strongly deflected by the welding spots and reciruclation zones and follows a nearly sinusoidal path.

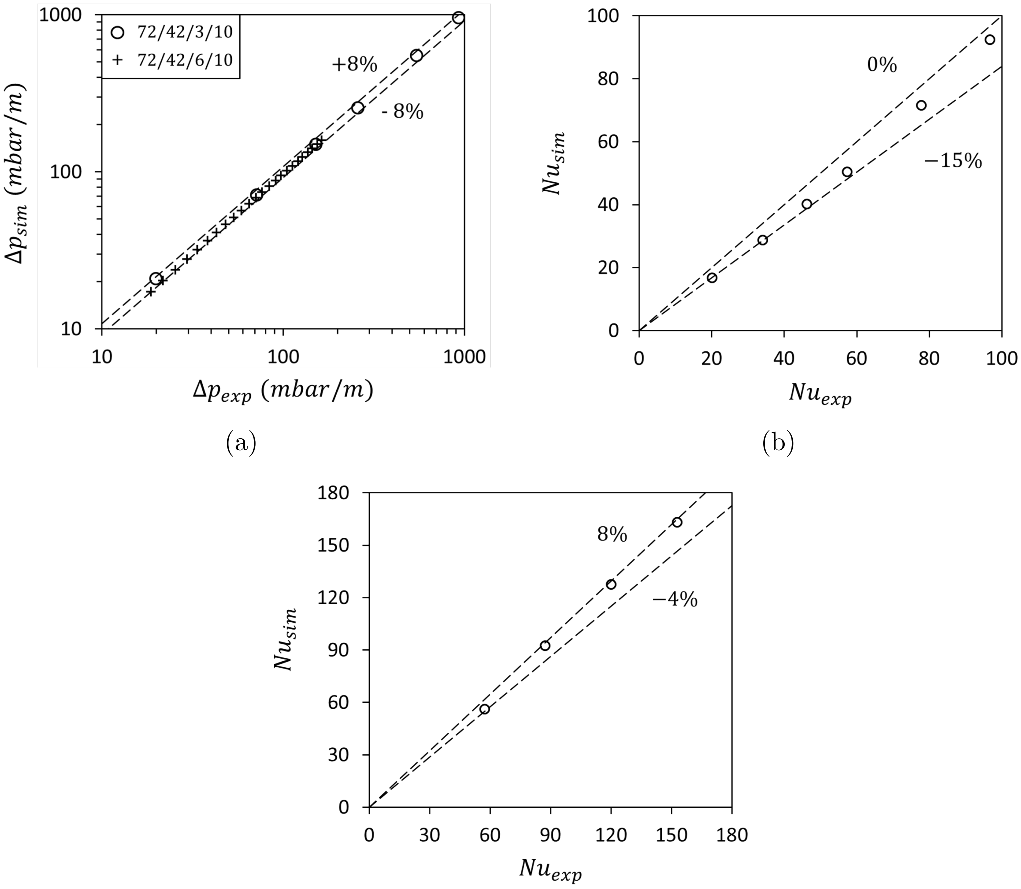

(a) (b)

(c)

Figure 5.10: Comparison of numerical and experimental results for turbulent pressure loss (a), Nusselt numbers for $Pr = 6$ and $Re = 1000; 2000; 4000; 6000; 8000$ (b), Nusselt numbers for $Re = 4000$ and $Pr = 5; 20; 50; 100$ (c).

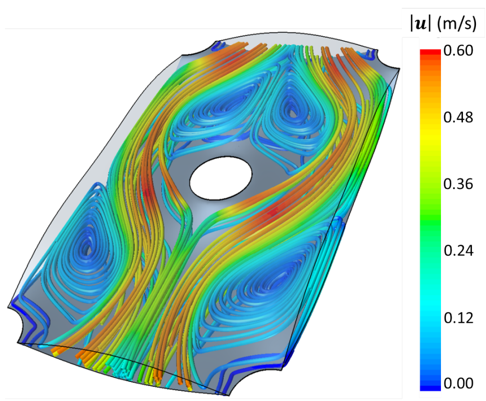

Figure 5.11: Illustration of the characteristic flow pattern in pillow plates represented by streamlines. The upper wall of the channel is transparent while the bottom wall is not for the sake of visualization.

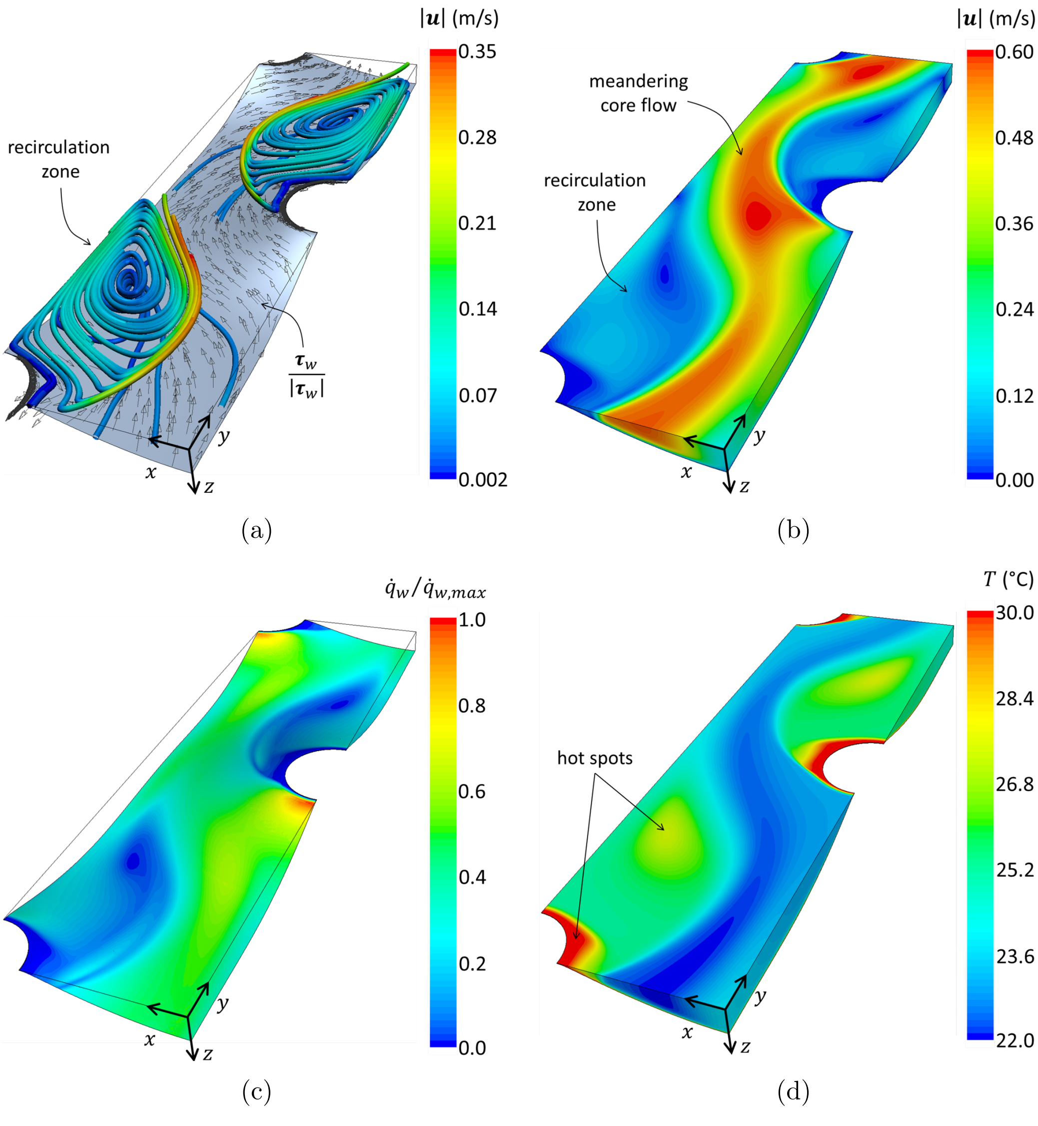

Figure 5.12: Vortex structures in the wake of the welding spots (a), developed velocity field (b), field of normalized wall heat flux (c) and temperature field (d) for turbulent flow in a pillow-plate channel for $Re = 2000$ and $T_w = 30°C = const$. Geometry: $s_T = 42$ mm, $s_L = 36$ mm, $d_{sp} = 10$ mm and $\delta_i = 6$ mm.

In Fig. 5.12(a), the steady vortices in the wake of the welding spots are shown in detail. They have a weak "tornado-type" character. Fluid near the wall is captured by the vortex core and transported normally to the wall, up to the symmetry plane ($z = 0$). The unit vectors of the wall shear stress ($\tau_\mathbf{w}/|\tau_\mathbf{w}|$) in Fig. 5.12(a) and the streamlines adjacent to the wall (blue) elucidate the inward fluid flow (near the wall) towards the recirculation zones.

Fig. 5.12(b) shows, based on the scalar velocity field, the characteristic *two-zone* flow pattern encountered in pillow plates. Zone 1 is represented by the meandering core flow and zone 2 by the recirculation areas. The size and shape of these zones depends on the pillow-plate geometry (e.g. welding spot pattern and inflation height) and is discussed further. Flow separation is caused by an adverse pressure gradient; it appears downstream of the stagnation point of the welding spot at an angle of approximately 50° (cf. Fig. 5.4). Furthermore, in Fig. 5.12(b), large velocity gradients are observed at the boundary between the meandering core and the recirculation zones, where the local velocity increases abruptly by a factor of about 11.

The influence of the flow phenomena shown in Fig. 5.12(b) on heat transfer is reflected by the field of the normalized wall heat flux in Fig. 5.12(c). Heat transfer in the recirculation zones is clearly poor; this results in hot spots in the temperature field shown in Fig. 5.12(d), especially at the eddy centers and in the immediate vicinity of the welding spots. Consequently, heat is transferred mainly in the meandering core region, where the local velocity is approximately twice the mean velocity in the channel flow. The periodic acceleration of the flow in stream-wise direction of the meandering core (visible in Fig. 5.12(b)) leads to a local increase of the wall heat flux (cf. Fig. 5.12(c)), caused by local reduction of the boundary layer thickness.

The simulations showed that the mean heat transfer coefficient in the pillow-plate channel with the geometry presented in Fig. 5.12, was proportional to $Re^{0.79}$. The exponent of the mean Reynolds number is mainly determined by the meandering core and is close to the value 0.8, which is typical for turbulent heat transfer in smooth pipes (see, e.g., [25]). Consequently, from the thermo-hydraulic point of consideration, the meandering region resembles a typical channel flow, which is bounded by the pillow-plate walls and the recirculation zones.

Furthermore, the simulations revealed that the heat transfer coefficient for the geometry shown in Fig. 5.12 is proportional to $Pr^{0.38}$, which is close to the exponent 1/3 typical for turbulent heat transfer in channels. Steimle [26] analyzed the exponents of the Reynolds and Prandtl numbers in correlations for turbulent forced convection heat transfer in numerous geometries and found that in most cases, the exponent of the Reynolds number is twice that of the Prandtl number, i.e. $Nu = C(Re^2 Pr)^n$. The factor C and the exponent n depend on the specific geometry. Considering the exponents for Re and Pr obtained from the simulations in this work, the expression of Steimle [26] also holds for pillow plates.

Influence of pillow-plate geometry on flow characteristics

The *two-zone* character of the flow pattern shown in Fig. 5.12 is characteristic for the flow in pillow-plates; however, depending on the particular pillow-plate geometry, the size and shape of the recirculation zones can vary. In the simulations three sub-categories of the characteristic flow pattern were observed, namely for pillow plates with $s_r > 1.56$ (longitudinal type), $s_r \leq 1$

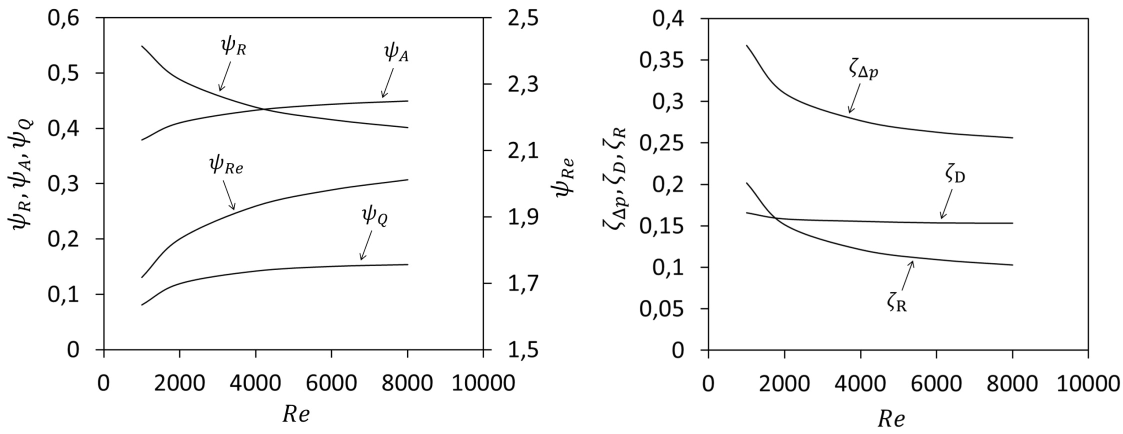

(a) (b)

Figure 5.13: Dimensionless two-zone variables (a) and friction coefficients (b) as functions of the Reynolds number for $Pr = 6$. Geometry: $s_T = 42$ mm, $s_L = 36$ mm, $d_{sp} = 10$ mm and $\delta_i = 3$ mm.

(transversal type) and $1 < s_r \leq 1.56$ (mixed type). Both the two-zone character of the flow and the differences between the flow patterns of these categories can be quantified with the help of the following parameters:

$$\psi_R = \frac{\zeta_R}{\zeta_{\Delta p}} \tag{5.10}$$

$$\psi_A = \frac{A_{RZ}}{A_{tot}} \tag{5.11}$$

$$\psi_Q = \frac{\dot{Q}_{RZ}}{\dot{Q}_{tot}} \tag{5.12}$$

$$\psi_{Re} = \frac{Re_{mc}}{Re_{tot}} \tag{5.13}$$

The parameter ψ_R is used to represent skin friction ζ_R; it gives the ratio of frictional losses to total pressure loss. The size of the recirculation zones is characterized by ψ_A, which is defined as the ratio of the wall area covered by the recirculation zones to the total area of the wall. The thermal activity of the recirculation zones is quantified by ψ_Q and is defined as the ratio of the rate of heat transferred only in the recirculation zones to the total rate of heat transferred normal to the wall. The parameter ψ_{Re} represents the ratio of the Reynolds number defined for the meandering core only ($Re_{mc} = u_{m,mc} d_{h,mc}/\nu$) and the mean Reynolds number in the pillow plate channel.

- **Heat and fluid flow characteristics of longitudinal-type pillow plates** ($s_r \geq 1.56$)

  The results presented in Fig. 5.12 are obtained for longitudinal-type pillow plates. They are characterized by recirculation zones, which have a "flame-like" shape and have a length close to s_L. Due to this shape, the primary flow is deflected significantly and follows a "meandering-like" path.

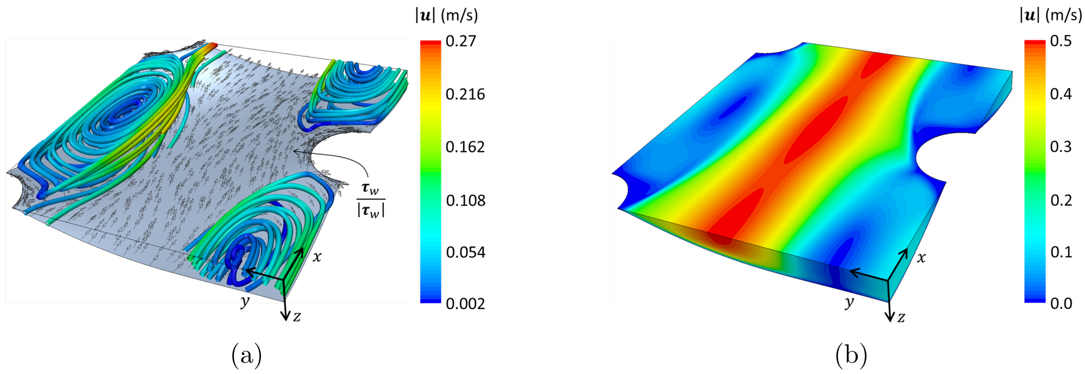

Figure 5.14: Vortex structures in the wake of the welding spots (a) and developed velocity field (b) for turbulent flow in transversal-type pillow plates for $Re = 2000$. Geometry: $s_T = 72$ mm, $s_L = 21$ mm, $d_{sp} = 10$ mm and $\delta_i = 6$ mm.

The profile of ψ_A in Fig. 5.13(a) shows that the flow pattern in pillow-plates with $s_r > 1.56$ is only weakly dependent on the Reynolds number. Thus, the area of the recirculation zones varies only slightly with Re and occupies approximately 45% of the total wall area. These regions cause the major portion of the form drag, which is responsible for more than 50% of pressure loss in the pillow-plate channel, as can be confirmed by the ψ_R profile in Fig. 5.13(a). The larger the Reynolds number is, the larger is the size of the recirculation zones and, hence, the contribution of form drag to the total pressure loss. Note that the form drag coefficient in longitudinal-type pillow plates is almost constant for all Reynolds numbers (Fig. 5.13(b)), so that the trend of the pressure loss coefficient is similar to the trend of the Fanning friction factor (cf. Fig. 5.13(b)).

The rate of heat transferred normal to the wall in the recirculation zones is only 15% of the total, even at the highest Reynolds number, although almost 50% of the wall area is covered by recirculation zones. This confirms the poor thermal activity in the recirculation zones and that, conversely, the meandering core dominates heat transfer.

- **Heat and fluid flow characteristics of transversal-type pillow plates** ($s_r \leq 1$)

The flow pattern shown in Fig. 5.14 is characteristic for transversal-type pillow plates with $s_r \leq 1$. In contrast to the longitudinal-type, the recirculation zones in transversal-type pillow plates extend to the next downstream welding spot and thus occupy a larger portion of the channel. The shape of the recirculation zones affect the flow path of the meandering core; the latter is deflected less significantly by the welding spots and follows a more linear path.

The flow pattern in transversal-type pillow plates is also largely independent of the Reynolds number, as can be seen from the ψ_A curve in Fig. 5.15(a). In contrast to longitudinal-type pillow plates, here the values of ψ_A show that the recirculation zones in transversal-type pillow plates are larger. However, the contribution of the form drag coefficient to the overall pressure loss coefficient is smaller than for longitudinal-type pillow plates and, moreover, smaller than the contribution of the Fanning friction factor ($\psi_R > 0.5$; cf. Fig. 5.15(b)). This is related to the shape of the recirculation zones,

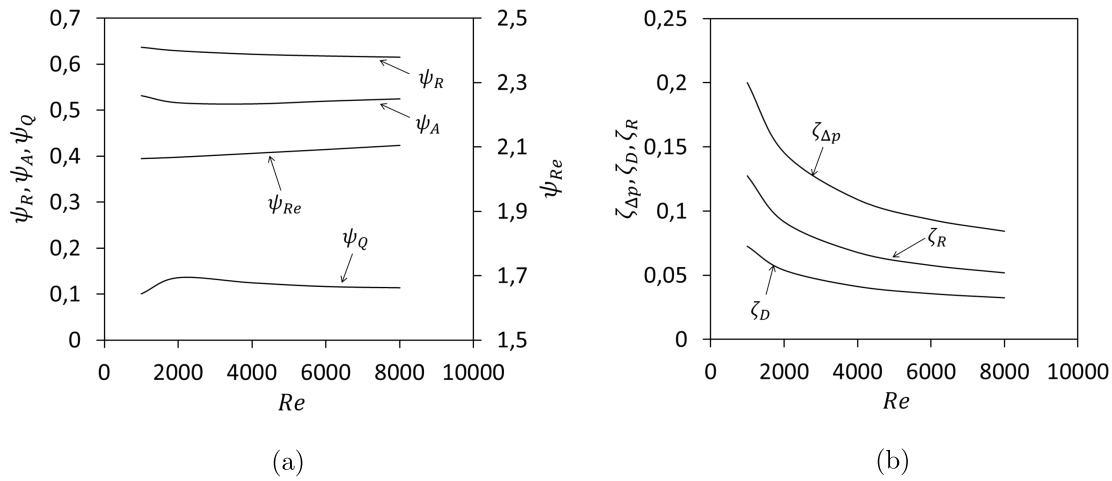

Figure 5.15: Dimensionless two-zone variables (a) and friction coefficients (b) as functions of the Reynolds number for $Pr = 6$. Geometry: $s_T = 72$ mm, $s_L = 21$ mm, $d_{sp} = 10$ mm and $\delta_i = 3$ mm.

which occupy less channel cross-section. As the consequence, the meandering core is less deflected and, hence, the resistance to flow is smaller.

The thermal activity of the recirculation zones in transversal-type pillow plates is poorer than in longitudinal type. Whilst the recirculation zones in the former are larger in size, the portion of heat transferred in these zones (ψ_Q) is similar to that of the longitudinal type. The mean Reynolds number in the meandering core is larger than in longitudinal-type pillow plates (cf. Fig. 5.15(a)), because of the more homogeneous velocity profile related to the larger channel cross-section.

- **Heat and fluid flow characteristics of mixed-type pillow plates** ($1 < s_r \leq 1.56$)

The flow patterns in longitudinal-type and transversal-type pillow plates are largely independent of the Reynolds number, i.e. ψ_A varies only slightly with Re. In mixed-type pillow plates, however, the flow pattern varies substantially with Re. As can be seen in Fig. 5.16, at small Reynolds numbers ($Re \leq 2000$) the flow pattern resembles that of longitudinal-type pillow plates. At larger Reynolds numbers ($Re > 2000$), the recirculation zone increases substantially in size until it reaches the next downstream welding spot.

The variation of the flow pattern with the Reynolds number can be followed by the trend of ψ_A in Fig. 5.17(a). Up to $Re = 4000$, ψ_A increases strongly and thereafter only weakly with the Reynolds number. A similar behavior of ψ_Q is visible, since this parameter is directly related to the size of the recirculation zones.

The dependency between the size of the recirculation zones, i.e. ψ_A, and form drag are shown in Fig. 5.17(b). Due to the strong increase in the size of the recirculation zones for $Re < 4000$, a large increase in the form drag coefficient ζ_D is observed. The variation of the pressure loss coefficient $\zeta_{\Delta p}$ with the Reynolds number shown in Fig. 5.17(b) is characteristic for mixed-type pillow plates. The profile of $\zeta_{\Delta p}$ in Fig. 5.15(b) can be understood from its definition: $\zeta_{\Delta p} = \zeta_R + \zeta_D$. The aforementioned increase of the form

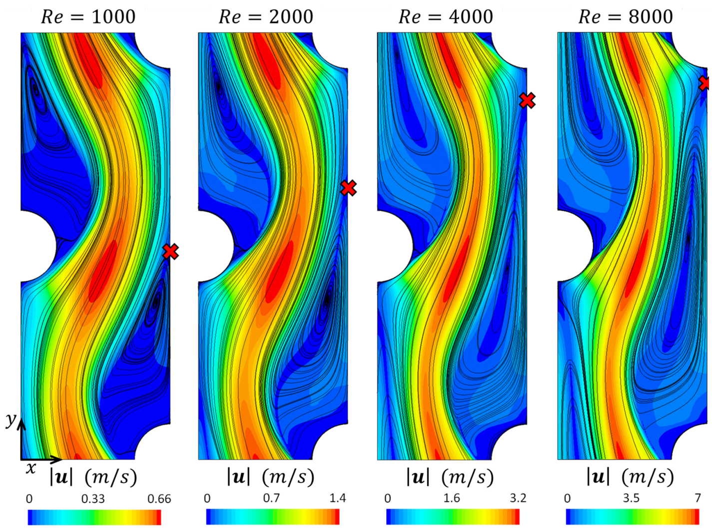

Figure 5.16: Developed velocity field of turbulent flow in mixed-type pillow plates for different Reynolds numbers (at symmetry plane $(x, y, 0)$). The red “x” indicates the end of the recirculation zone. Geometry: $s_T = 42$ mm, $s_L = 30$ mm, $d_{sp} = 10$ mm and $\delta_i = 3$ mm.

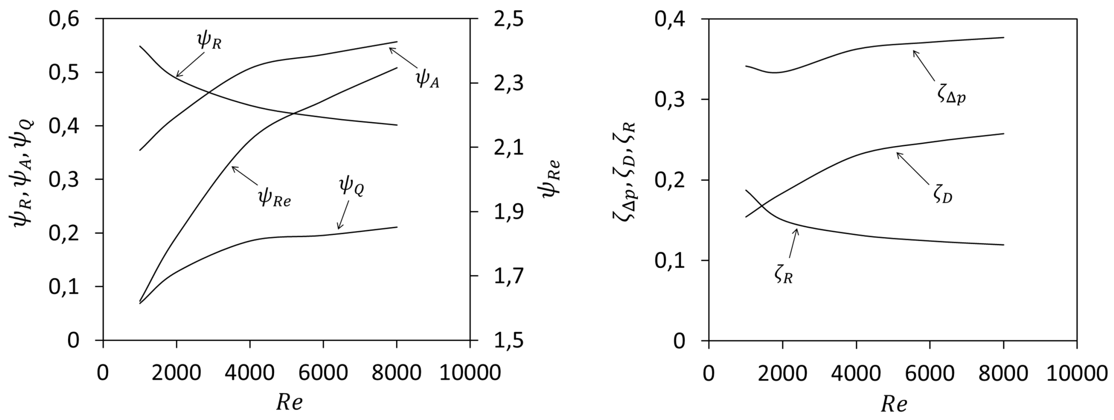

(a) (b)

Figure 5.17: Dimensionless two-zone variables (a) and friction coefficients (b) as functions of the Reynolds number for $Pr = 6$. Geometry: $s_T = 42$ mm, $s_L = 30$ mm, $d_{sp} = 10$ mm and $\delta_i = 3$ mm.

drag coefficient at small Reynolds numbers causes a sudden increase in $\zeta_{\Delta p}$, which then gradually becomes constant towards larger Re values.

Thermo-hydraulic efficiency of pillow-plates

The thermo-hydraulic efficiency is represented by the ratio between the benefit (the transferred heat) and the effort (the pumping power) required:

$$\epsilon = \frac{\dot{Q}}{\dot{W}} = \frac{hA_w\Delta T}{\dot{V}\Delta p} \tag{5.14}$$

The choice of characteristic geometrical parameters of pillow plates, e.g. the welding spot pattern and the channel height, strongly influences their thermo-hydraulic efficiency. When designing pillow plates, it is important to quantify this efficiency in order to (a) obtain the optimal geometry and (b) guarantee the most economical operation of the heat exchanger for a given task.

Eq. (5.14) is used to quantify the efficiency of the pillow-plate geometries investigated in this work. For a more convenient comparison with other geometries, the efficiency ϵ is normalized,

$$\epsilon^* = \frac{\epsilon}{\epsilon_{ref}} \tag{5.15}$$

so that it ranges from 0 to 1. Normalization is performed by dividing Eq. (5.14) by the efficiency of the geometry 42/72/6/10 (ϵ_{ref}) at $Re = 1000$. The latter showed the highest efficiency of all pillow plates investigated in this study.

Fig. 5.18(a) shows an example of the variation of ϵ^* with the Reynolds number for the geometry 42/72/6/10. All other pillow plate geometries demonstrated a similar trend.

The largest efficiency is obtained at the lowest Reynolds number $Re = 1000$; it decreases asymptotically thereafter. This is generally due to the different dependencies of the heat transfer coefficient and pressure loss on the Reynolds number. For example, the pillow plate 42/72/6/10 showed that $h \sim Re^{0.76}$ and that $\Delta p \sim Re^{1.63}$. Hence, compared to the heat transfer coefficient, pressure loss increases more significantly with the Reynolds number and thus decreases the efficiency.

Fig. 5.18(b) shows how the welding spot pattern and the channel height influence the efficiency. From left to right, i.e. from transversal-type towards longitudinal-type pillow plates, a minimum in the efficiency, attributed to the equidistant pattern $s_r = 1$, is observed. Hence, equidistant pillow plates show the smallest efficiency of all pillow plates studied. Considering that each welding spot represents a resistance to flow, in the case of $s_r = 1$, the number of welding spots per square meter is largest and so is the resistance to flow. In the case of longitudinal-type pillow plates, the efficiency is higher than for $s_r = 1$ (for the same s_T), because the number

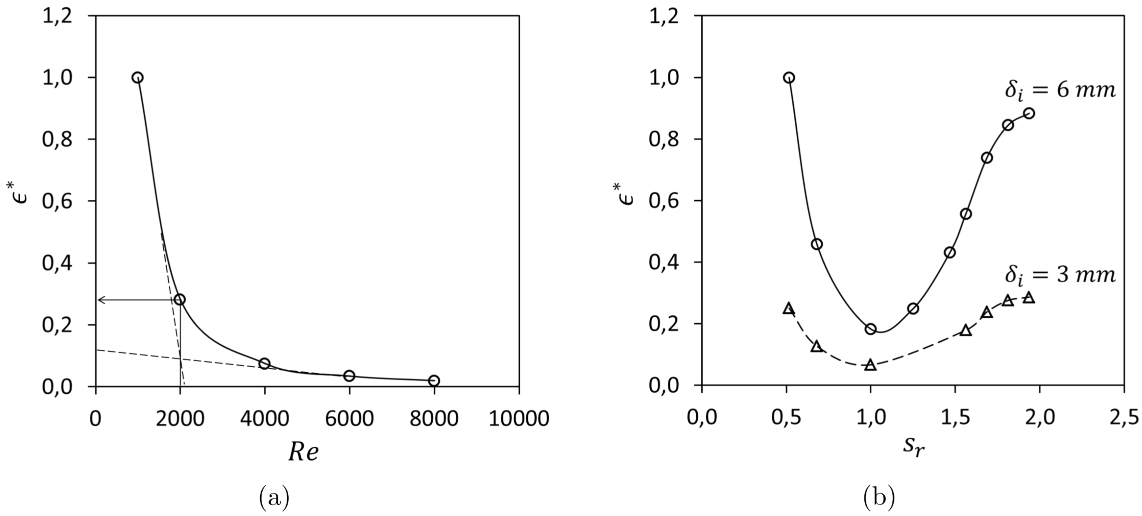

Figure 5.18: Thermo-hydraulic efficiency as a function of the Reynolds number for the tranversal type pillow-plate 42/72/6/10 (a), and as a function of s_r for $Re = 2000$ (b).

of welding spot rows in stream-wise direction is lower. For $s_r \gg 1$, the efficiency ϵ^* seems to approach a constant value. Hence, welding spot patterns, whose ratio s_r exceeds that of the typical triangular arrangement with $s_r > 1.9$, do not seem to yield further advantages.

On the other hand, approaching more "transversal" geometry (i.e. with decreasing s_r) results in better efficiency. This is because the portion of form drag ("bad pressure loss") to overall pressure loss is reduced compared to longitudinal-type pillow plates. Form drag increases overall pressure loss more significantly without contributing to heat transfer. For example, taking geometry 42/42/6/10, the heat transfer coefficient shows that $h \sim Re^{0.74}$ and that $\Delta p \sim Re^{1.9}$. The difference in the exponents of the Reynolds number for h and Δp is larger than for e.g. the transveral type pillow plate 42/72/6/10. Thus, the increase in Δp with Re compared to the increase of h with Re, is stronger than for pillow plates with smaller s_r. For $s_r \to 0$, the efficiency should asymptotically approach the value of a plane channel.

Furthermore, the efficiency grows with the channel height (see Fig. 5.18(b)). The latter increases the mean channel cross-section, and, consequently the mean stream velocity decreases at a constant Reynolds number. As the result, pressure loss is lower. In summary, the optimal design can be obtained with a pillow plate having a small s_r, a large channel height and operating at "lower" Reynolds numbers. Although the smallest Reynolds number results in the highest efficiency, it gives the smallest heat transfer coefficient. This means, that the heat exchanger will be large in size (large heat transfer area) to compensate for the small h, thus resulting in high equipment cost. A reasonable compromise between the thermo-hydraulic efficiency and heat transfer coefficient is achieved by setting the Reynolds number at the intersection between the two tangents, as illustrated in Fig. 5.18(a).

Geometry optimization

As discussed above, the recirculation zones observed in the wake of the welding spots increase pressure loss and are less effective for heat transfer compared to the meandering core. Conse-

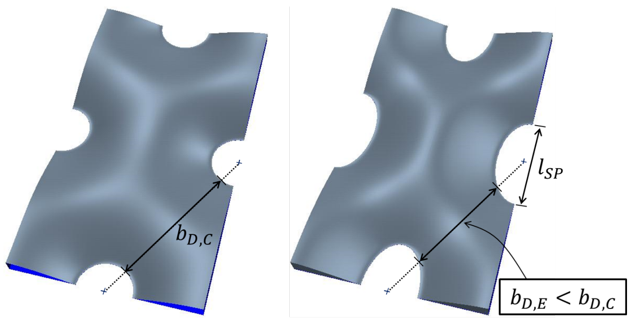

Figure 5.19: Pillow plate with round welding spots (a) and with elliptical welding spots (b).

Table 5.4: List of investigated pillow-plate geometries for the optimization study.

$2s_L$ mm	s_T mm	δ_i mm	d_{SP} mm	l_{SP}/d_{SP} mm	Comments Abbreviation	Abbreviation
72	42	6	10	1	-	72/42/6/10
72	42	6	10	2	-	72/42/6/D
72	42	6	7.07	2	$A_{round} = A_{oval}$	72/42/6/A
72	42	6	7.2	1	-	72/42/6/7.2
42	72	6	10	1	-	42/72/6/10
42	72	6	10	2	-	42/72/6/D
42	72	6	7.07	2	$A_{round} = A_{oval}$	42/72/6/A
42	72	6	7.2	1	-	42/72/6/7.2

quently, by reducing the size of these zones, an improvement of the thermo-hydraulic performance of pillow plates can be achieved. For this reason, the development of recirculation zones was investigated for oval-shaped welding spots, which are more streamlined.

Fig. 5.19 shows an example of two pillow-plate geometries, which have the same welding spot pattern and inflation height, but different welding spot shapes. In this example, the transversal welding spot diameters d_{SP} of both geometries are equal; however, the longitudinal diameter of the oval welding spots is two times the transversal diameter. This changes both the shape of the welding spots and the waviness of the channel walls (Fig. 5.19); hence, also the local cross-sectional areas of the channel is changed. Tab. 5.4 summarizes the pillow-plate geometries investigated in this optimization study.

The letter "D" at the end of the abbreviation in Tab. 5.4 denotes pillow plates with oval welding spots, which have the same transversal diameter as the round ones. Accordingly, the letter "A" represents pillow plates with oval welding spots, which have the same surface area as those with round spots.

The effect of the welding spot shape on the size of the recirculation zones in longitudinal type pillow plates is presented in Fig. 5.20. The use of oval welding spots clearly reduces the size of the secondary flow (cf. Fig. 5.20(b)(c)). Although the shape of these welding spots is more streamlined, they do not lead to a shift of the separation point. Rather the reduction in the size of the recirculation zones is caused by the channel waviness. The latter is notably different compared to a pillow plate with round welding spots. The width ($b_{D,E}$) for pillow plates with elliptical welding spots, as shown in Fig. 5.19, is smaller than $b_{D,C}$ for pillow plates with

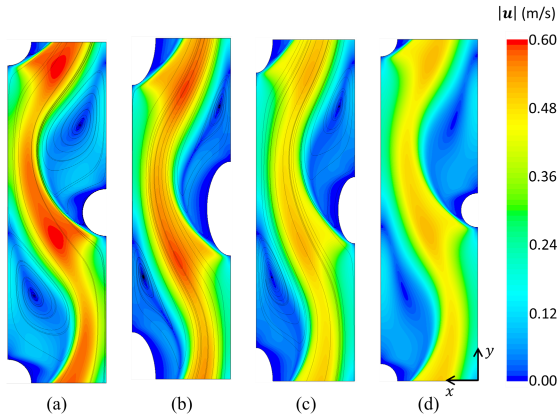

Figure 5.20: Developed velocity field in a pillow plate with the geometry 72/42/6/10 (a), 72/42/6/D (b), 72/42/6/A (c) and 72/42/6/7.2 (d).

round spots. This leads to an earlier redirection of the meandering core, due to the opposing action of the next (diagonally placed) downstream welding spot on the flow. Consequently, the recirculation regions are "squashed" and thus restricted in size. This results in the meandering core following a more linear path with less deflection, compared to behavior shown in Fig. 5.20(a).

In Fig. 5.21, the simulation results for the optimization of longitudinal-type pillow plates are summarized. As can be seen, the geometry 42/72/6/D brings a reduction in ψ_A by 23%, which indicates a significant decrease in the size of the recirculation zones. As a result, the portion of form drag on total resistance is also reduced (cf. increase in ψ_R), which leads to a decrease in pressure loss of up to 12%. On the other hand, the product hA_w drops by almost the same amount, thus reducing the improvement of the thermo-hydraulic efficiency ϵ^*. The product hA_w is more informative than just h, since the heat transfer area in 42/72/6/D is reduced by 5%, due to the larger surface of the oval welding spots compared to round ones. Therefore, the use of oval welding spots, which have the same surface area as the round ones in 42/72/6/10, was also investigated. The flow pattern in such pillow plates is seen in Fig. 5.20(c), and it is similar to that in Fig. 5.20(b). The geometry 42/72/6/A results in a significant reduction in pressure loss of up to 35%, while hA_w decreases by only 9%. The combined result is an improvement in efficiency ϵ by as much as 37%. Since the transversal diameter of the smaller oval welding spot in 42/72/6/A leads to a smaller form drag, the use of round welding spots with a smaller diameter than in 42/72/6/10 was also analyzed. The flow pattern of this case is shown in Fig. 5.20(d). The small-diameter round welding spots in 42/72/6/7.2 are even more efficient than the small oval welding spots (42/72/6/A). They lead to an efficiency improvement by as much as 43% (cf. Fig. 5.21).

Since the use of oval welding spots and small round ones improves the overall thermo-hydraulic performance of longitudinal-type pillow plates, their impact on transversal-type pillow plates was also studied. The results of this study are presented in Figs. 5.22 and 5.23.

In contrast to longitudinal-type pillow plates, the flow pattern in transversal-type pillow plates with oval welding spots does not change notably. The size of the recirculation zones is reduced (cf. Fig. 5.22(b)); but this time mainly due to the smaller distance l_R between successive welding

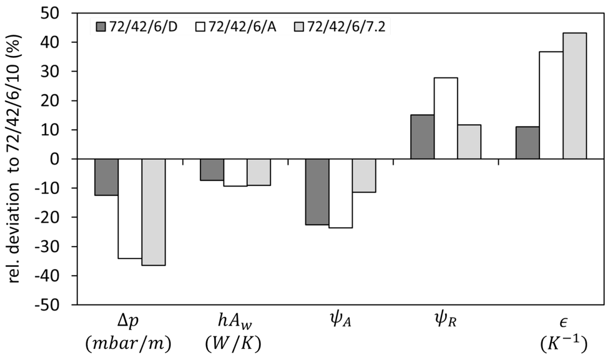

Figure 5.21: Thermo-hydraulic characteristics of longitudinal type pillow-plates with different welding spot geometries, compared to the reference pillow plate 72/42/6/10. The results are based on the same volume flow rate in all geometries.

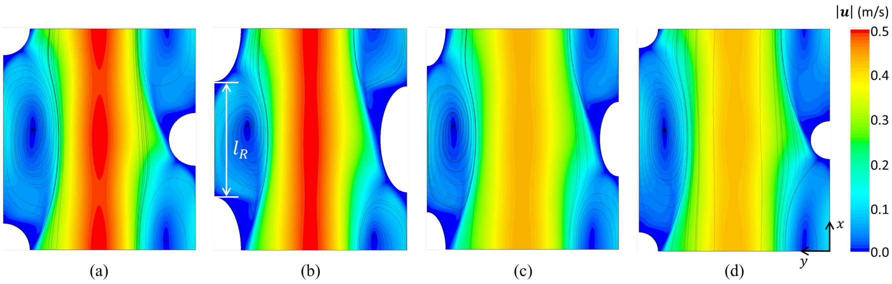

Figure 5.22: Developed velocity field in a pillow plate with the geometry 42/72/6/10 (a), 42/72/6/D (b), 42/72/6/A (c) and 42/42/6/7.2 (d).

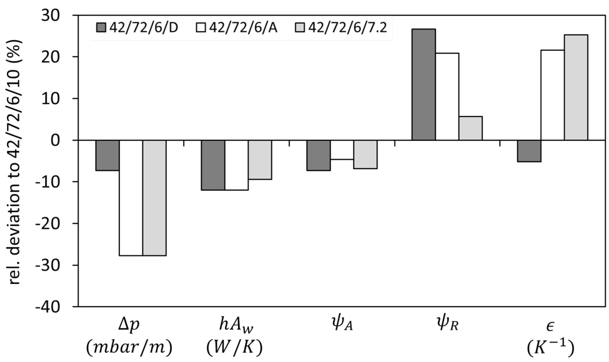

Figure 5.23: Thermo-hydraulic characteristics of transversal type pillow-plates with different welding spot geometries, compared to the reference pillow plate 42/72/6/10. The results are based on the same volume flow rate in all geometries.

spots.

The efficiency in the transversal-type geometry 42/72/6/D is reduced by 5%, compared to the reference geometry 42/72/6/10. On the other hand, by using oval welding spots with the same surface area as the round ones in 42/72/6/10, i.e 42/72/6/A, the thermo-hydraulic performance is improved by 22%. Similar to longitudinal-type pillow plates, the best improvement in transversal-type pillow plates is achieved by using small round welding spots (42/72/6/7.2), with an efficiency of up to 25% (cf. Fig. 5.23).

In summary, the use of oval welding spots or small round ones can significantly improve the thermo-hydraulic efficiency of pillow plates, especially of the longitudinal type. Oval-shaped welding spots are simple to manufacture when using automated laser welding technology.

5.3 Conclusions

This chapter focused on fluid dynamics and heat transfer in the inner channels of PPHE investigated both experimentally and by CFD simulations. Two different experimental facilities were used to validate the CFD simulations. The first one contained a unique experimental set-up encompassing a transparent pillow-plate channel. This facility provided the first flow visualization in pillow plates. A comparison with the flow pattern obtained by CFD showed that the simulations can reproduce the complex fluid dynamics in pillow-plate channels with a good accuracy. Both facilities were used to measure pressure loss in pillow plates, while the second experimental set-up was used to also measure heat transfer coefficients in pillow plates. The CFD simulations proved to accurately capture these quantities as well.

In the next step, a comprehensive CFD analysis of fluid dynamics and heat transfer in pillow plates was performed. The simulations showed that the fully developed turbulent flow in pillow plates is characterized by two distinctive regions, namely, (a) recirculation zones arising in the wake of the welding spots, and (b) the core flow, which is bounded by the walls and the recirculation zones. The latter produce form drag, which increases pressure loss in the channel. Depending on the geometry, three sub-categories of the characteristic flow pattern, a longitudinal-type, a transversal-type and a mixed-type could be identified. They differ mainly in the size and shape of the recirculation zones. While the characteristic flow pattern in longitudinal-type and transversal-type pillow plates is only weakly dependent on the Reynolds number, in mixed-type pillow plates, the recirculation zones increase significantly in size with growing Reynolds number.

Furthermore, the thermo-hydraulic efficiency of pillow plates was studied. The largest efficiencies were observed at the lowest Reynolds number; they decreased rapidly at larger Reynolds numbers. The lowest efficiencies were found for pillow plates, in which the longitudinal and transversal welding spot pitches were equal. The highest efficiencies were obtained for transversal-type pillow plates with the larger inflation height.

Finally, a geometry based optimization study for improving the thermo-hydraulic efficiency of pillow plates was performed. It was found that by using “oval-shaped” welding spots, which are more streamlined than round ones, the efficiency can be increased by as much as 37% for longitudinal-type pillow plates and by 22% for transversal-type pillow plates. Even greater improvements in the efficiency were found for reduced size of the welding spots.

6 Fluid dynamics and heat transfer in outer pillow-plate channels

Design of PPHE requires knowledge of overall heat transfer coefficients, and thus, fluid flow and heat transfer in the outer channels must be governed. The geometry of the channels between adjacent pillow plates differ from that of the inner channels, as illustrated in Fig. 2.4. While fluid in the inner channels is forced to flow around welding spots, they are missing in the outer channels. Therefore, the flow approximately follows a linear path and pressure loss in the outer channels is significantly lower. Furthermore, two additional geometrical parameters related to the outer channels can be varied, namely, the distance between the neighboring pillow plates δ_P and the relative shift between these plates. Thus, the development of generic design methods for the outer side requires a more extensive CFD study than for the inner side. In this work, the fluid dynamics and heat transfer in the outer channels is studied only for a single configuration of the characteristic geometry parameters of pillow plates.

6.1 CFD simulation

CFD simulations for the outer channel were carried out, again, using the commercial solver STAR-CCM+. In Fig. 6.1, the computational domain for the outer pillow-plate channel is illustrated.

In contrast to the flow in the inner channels, here, the flow was largely transient and periodic. This made the use of flow symmetry planes not possible for the outer channels, as was done for the inner channels (cf. Fig. 5.7). As a result, the domain for the outer channels is larger. Nevertheless, it was possible to reduce the computational effort by utilizing the flow periodicity, both for the inlet ($y = 0$) and for the outlet ($y = 2s_L$) as well as for the side boundaries ($x = -0.5s_T$ and $x = 0.5s_T$). Periodicity for $x = -0.5s_T$ and $x = 0.5s_T$ was used by directly mapping these boundaries, while for the inlet and outlet, it was done in such a way that the velocity field was repeated after twice the longitudinal pitch ($2s_L$). This offers the advantage of

A part of the material presented in this chapter has been published in Piper et al. [4].

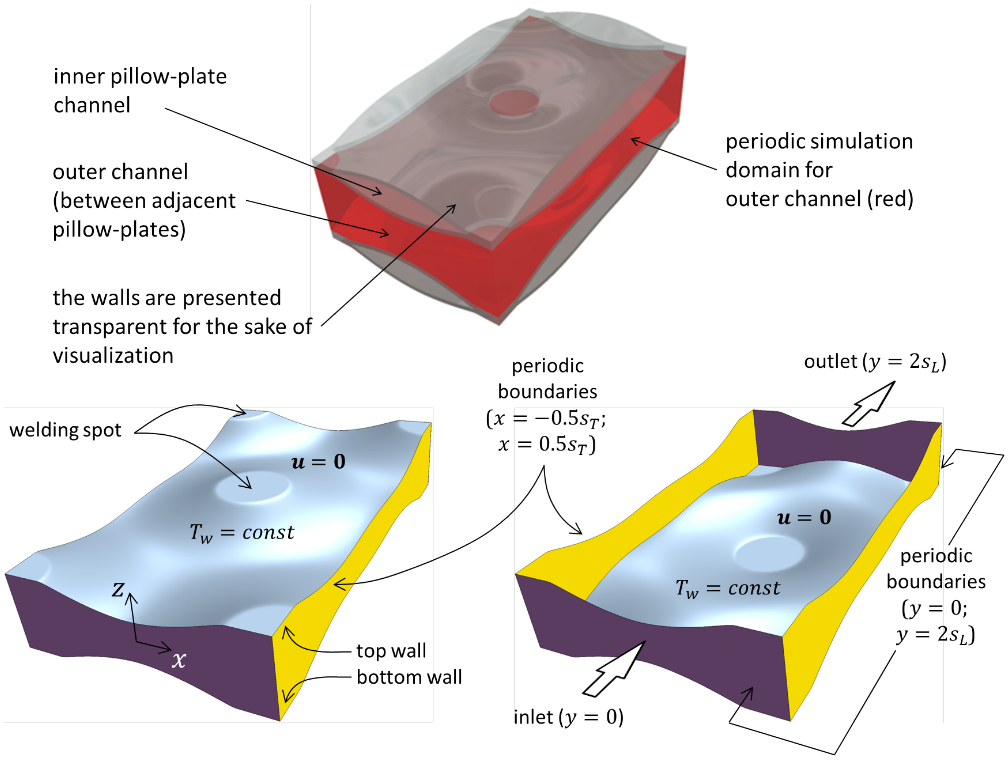

Figure 6.1: Periodic computational domain of the outer pillow-plate channel with staggered welding spots.

reduced calculations within the (periodically) hydrodynamically developed region, which usually occupies the major part of the channels in industrial-scale pillow-plate heat exchangers.

The type of boundary conditions used for the energy equation were similar to those described in Sec. 5.2.1. Constant temperature walls were used in the simulations for both the inner and outer channel. As a matter of fact, the use of this boundary condition is common practice, although, in reality, the wall temperature is not constant; rather, it varies spatially, in line with thermal coupling between the inner and outer channel. Such coupling can be captured if conjugated heat transfer models are used. However, the computational expense in this case is very high. Nevertheless, it is expected that the deviation between heat transfer coefficients determined with constant temperature wall boundary condition and the condition in reality, is marginal.

The flow in the outer channels was considered under similar assumptions as for the inner channels (cf. Sec. 5.2.1), namely: single-phase, incompressible, three-dimensional, turbulent and with constant physical properties. Turbulence was described by the EB-$k-\varepsilon$ model (Sec. 3.3.4) instead of the less computationally expensive realizable $k-\varepsilon$ model used for inner channels. Both models provided similar results for the inner channel, however, for the outer channel the EB-$k-\varepsilon$ model was superior, as will be discussed later in Sec. 6.3. In contrast to the realizable $k-\varepsilon$ model, the EB-$k-\varepsilon$ model accounts for turbulence anisotropy in shear layers, which makes it more capable of accurately predicting boundary layer separation and re-attachment over smooth curved surfaces, which are met in the outer pillow plate channel.

For the simulation of the outer channel, a structured body-fitted grid, shown in Fig. 6.2 was used. This grid type is ideal for wavy surfaces, since the cells align with the geometry contours,

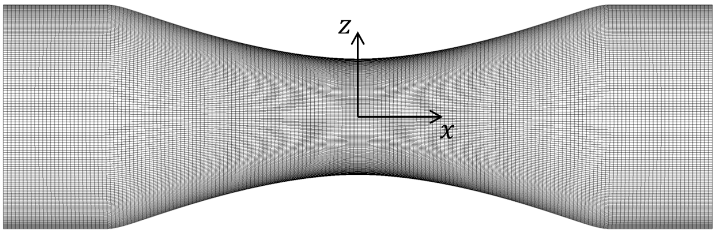

Figure 6.2: Example of structured body-fitted grid used in the simulations of the outer pillow plate channel. View on the (x,0,z)-plane.

and this property leads to high-quality cells favorable for numerical accuracy and convergence. Satisfactory resolution of the boundary layers was achieved with the same techniques as presented in Sec. 5.2.1.

6.2 Experimental set-up

The experimental facility used to measure pressure loss between two adjacent pillow plates is shown in Fig. 6.3. Water is directed from a feed tank (FT) to the test channel (PP) by means of a centrifugal pump (P). The mass flow of water is measured downstream of the pump using a Coriolis flow sensor (Emerson Micro Motion® CMF050) and is adjusted by the manual valve (V). Subsequently, water flows in the channel between two adjacent pillow plates (PP) and is then collected again in the feed tank (FT). The test channel (PP) was built by two adjacent pillow plates. The constant distance between the pillow plates was achieved by two 12 x 12 mm stainless steel rods placed on the flat edges of the pillow plates. When considering the additional sealing strips, the maximum channel height δ_P of the channel was equal to 13 mm. The fluid was distributed at the channel inlet via the distributor (D1) and collected at the channel outlet D2. The channel had a length of 1000 mm and a width of 270 mm. The pillow plates used in the experiments have industrially relevant characteristic dimensions: $s_T = 42$ mm, $2s_L = 72$ mm, $d_{SP} = 12$ mm and $\delta_i = 7$ mm. They were manufactured from austenitic stainless steel plates of material 1.4541, with a surface finishing of quality 2B (DIN EN 10088-2), which had a typical mean roughness $R_a \approx 0.1 - 0.5$ μm. This surface is technically smooth, hence the effect of surface roughness on frictional losses is assumed to be negligible.

For the measurement of pressure loss in the wavy channel, two bore holes with a diameter of 2 mm were drilled through the center of the welding spots of one of the pillow plates. Burrs created from the drilling were fully removed to eliminate measuring uncertainty caused by flow disturbances around the burrs. Bushings were then brazed onto these welding spots in order to accommodate hose sockets (cf. Fig. 6.3), which were used to attach the pressure measuring lines. Brazing was used instead of welding in order to reduce heat input into the heat affected zone, which could cause a deformation of the pillow plate at the welding spot. The measuring ports were placed far enough from the inlet and outlet and the channel edges. In this way, only the fully developed flow region was considered and the influence of edge effects could be reduced. Moreover, the distance between the measuring ports was large (429 mm = $12s_L$), thus reducing measuring uncertainty. Pressure loss was measured using a digital differential pressure sensor

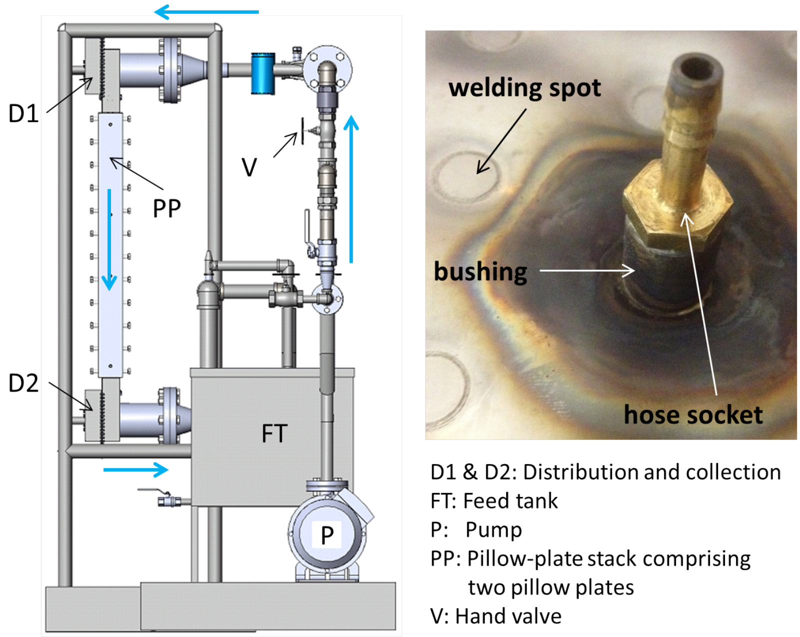

Figure 6.3: Experimental facility used for the pressure loss measurements in outer pillow-plate channel.

(Emerson Rosemount® 3051 CD3), while the experiments were performed under isothermal conditions ($T = 25°C$).

6.3 Method validation

Figure 6.4 shows a comparison of measured and calculated (with CFD) pressure loss values in the outer pillow-plate channel. Two sets of data are shown, namely, those obtained using the realizable $k - \varepsilon$ model and those using the EB-$k - \varepsilon$ model. As mentioned in Sec. 6.1, both models yielded similar results for the inner channels, however, for the outer channel the realizable $k - \varepsilon$ model leads to an underprediction of pressure loss by as much as 20%, while the EB-$k - \varepsilon$ model agrees quite well with the experiments (deviation $< 5\%$). For this reason, the EB-$k - \varepsilon$ model was adopted for all simulations of the outer pillow-plate channel.

6.4 Results and discussion

In the outer pillow-plate channel, the cross-section varies periodically and significantly in stream-wise direction. The channel is narrowest, where the inflation height of the pillow plates is largest (hill-to-hill); it is widest in the vicinity of the welding spots (trough-to-trough). As a result, the flow is accelerated and slowed down periodically. This leads to an adverse pressure gradient and causes boundary layer separation.

Fig. 6.5 shows an example-result of the CFD simulation of the flow in the outer pillow-plate channel. The fields shown here represent time-averaged values of the transient simulations. They

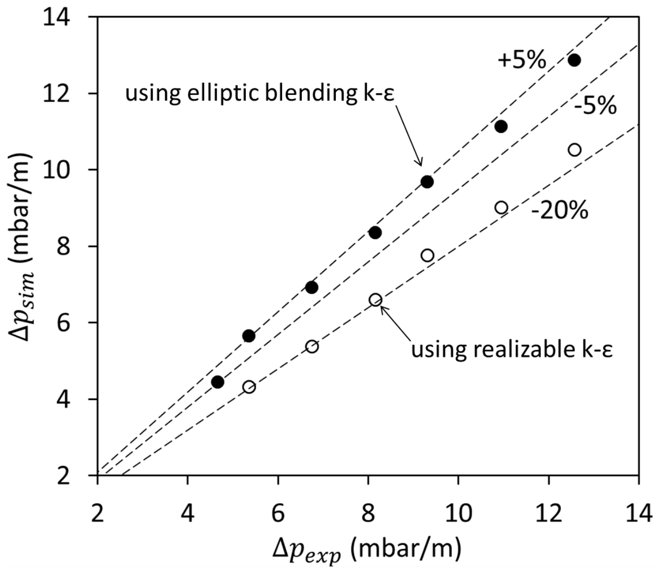

Figure 6.4: Parity plot of numerical and experimental results for pressure loss in the outer pillow-plate channel for $7000 \leq Re \leq 14000$ and $Pr = 6$. Black circles – simulations with the elliptic blending $k-\varepsilon$ model; white circles – simulations with the realizable $k-\varepsilon$ model.

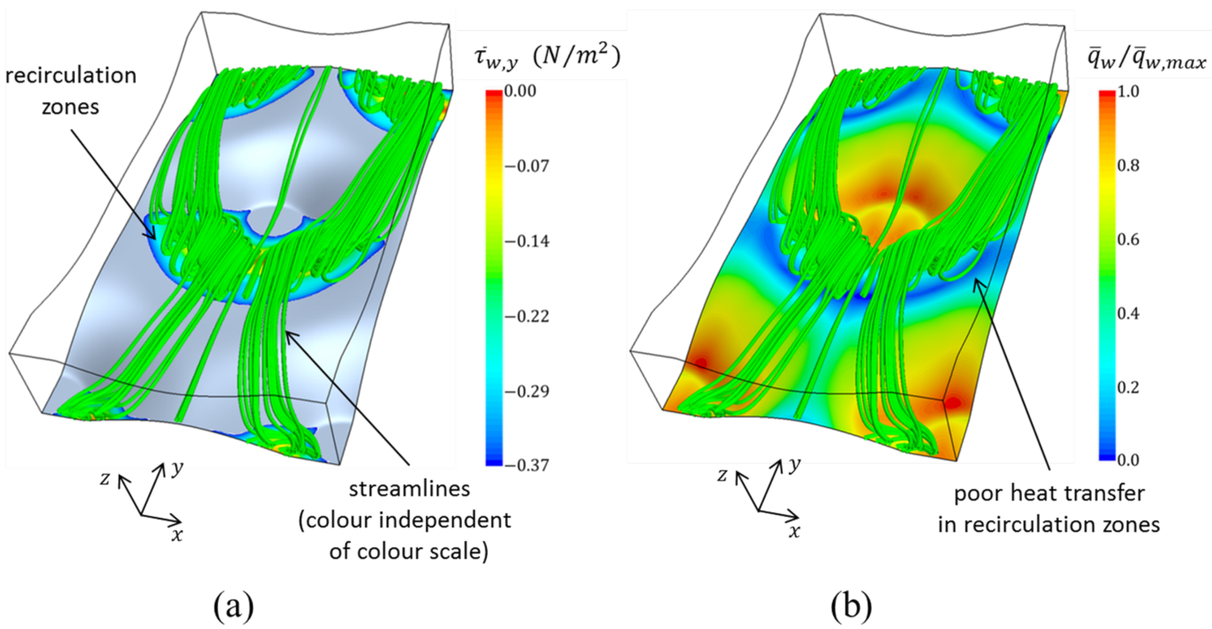

Figure 6.5: Illustration of characteristic vortex structures (represented by streamlines) arising in the vicinity of the welding spots in the outer pillow-plate channel ($Re = 5000$). Size of recirculation zones is represented by $\tau_{w,y} \leq 0$ (a). The effect of fluid flow on heat transfer is represented by the 2D-field of the normalized wall heat flux (b).

have been averaged over 10 periodic cycles in time. In Fig. 6.5 “tornado-like” vortex structures arising upstream of the welding spots can be seen. The size of these vortices can be evaluated more clearly by the regions of negative wall shear stress in Fig. 6.5(a), indicating recirculation of the flow. The fluid located in the vortices is transported spirally outwards away from the troughs; it is then directed diagonally into the next downstream trough. The recirculation zones cause form drag, which contributes approximately 50% of the Darcy friction factor. These zones occupy roughly 30% of the wall area, making them less effective for heat transfer, as can be seen in Fig. 6.5(b). After boundary layer re-attachment, the flow is re-accelerated out of a trough. This leads to steep temperature gradients and thus to high heat transfer rates.

6.5 Conclusions

The flow in the outer channels differs significantly from that in inner channels, mainly because the fluid is not forced to flow around the welding spots. Moreover, boundary layer separation in the outer channels occurs over the smooth curved surface of the pillow plates. Failure to accurately predict the location of boundary layer separation and reattachment would result in the a wrong estimation of the size and shape of the recirculation regions and, hence, of pressure loss and heat transfer. Therefore, the use of more advanced eddy viscosity models, which consider turbulence anisotropy, is necessary. The turbulence model used in this work was the elliptic-blending $k - \varepsilon$ model, which was able to predict pressure loss in turbulent flow in the outer channels of PPHE with a maximum relative deviation of 5%, compared to the experiments performed in this work.

The CFD simulations show, that boundary layer separation occurs upstream of the welding spots, leading to large but flat recirculation zones, which occupy roughly 30% of the wall area. These zones are the main cause of form drag, which contributes approximately 50% of the Darcy friction factor.

7 Design methods for PPHE

The development of accurate design methods for pillow-plate heat exchangers represents the main goal of this work. The data on fluid dynamics and heat transfer in PPHE necessary for the development of these methods were obtained largely by CFD simulations (cf. Secs. 5 and 6). A more comprehensive CFD study was accomplished for the inner channels, and thus, their design equations are more generic.

7.1 Design methods for the inner channels of PPHE

For the determination of heat transfer coefficients, two different approaches are presented. The first approach is based on the method typically suggested in literature, whereby the well-known Dittus-Boelter type power law function (cf. [16]) for the Nusselt number is applied and fitted to numerical data obtained in Sec. 5.2. The second approach is based on the characteristic flow pattern in pillow plates suggested in Sec. 5.2.

7.1.1 Design equation for pressure loss

Pressure loss is commonly represented by the dimensionless Darcy friction factor $\zeta_{\Delta p}$, which is defined by Eq. (5.4). Often, $\zeta_{\Delta p}$ is a function of the Reynolds number and is represented by a curve with asymptotic behavior, as shown in Fig. 7.1. This curve is valid for turbulent forced convection in a typical pillow-plate channel. The characteristic flow in such a pillow-plate channel is shown in Fig. 7.2.

Such a curve can be approximated with a power-law function:

$$\zeta_{\Delta p} = n_1 Re^{n_2} \tag{7.1}$$

A part of the material presented in this chapter has been published in Piper et al. [58].

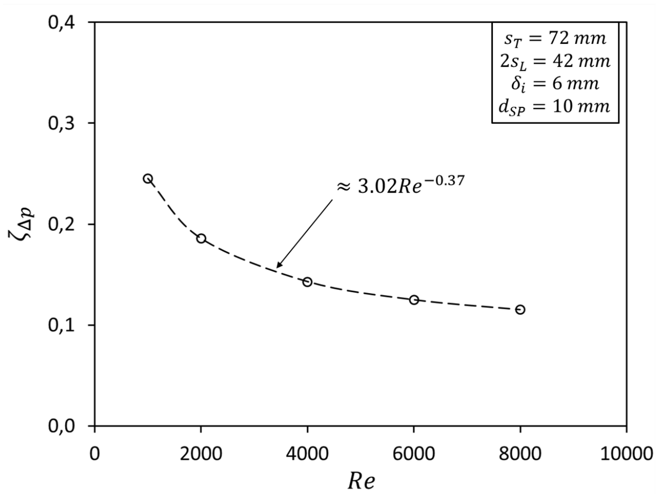

Figure 7.1: Darcy friction factor $\zeta_{\Delta p}$ as a function of the Reynolds number for turbulent, single-phase flow in a longitudinal-type pillow plate (cf. Sec. 5.2).

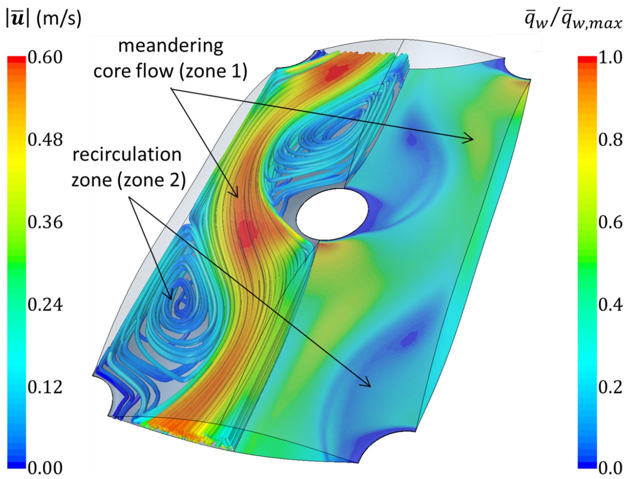

Figure 7.2: Characteristic flow pattern in pillow-plate channels represented by streamlines colored by the velocity magnitude (left half) and by the normalized wall heat flux 2D-field (right half).

This asymptotic behavior can be explained if different contributions of the two constitutes of the Darcy friction factor, namely the friction drag coefficient and the form drag coefficient, are considered. While the coefficient of form drag depends only weakly on Re in most pillow plate geometries (cf. Sec. 5.2), the friction drag coefficient shows an asymptotic trend resulting in an asymptotic behavior of $\zeta_{\Delta p}$ (cf. Eq. (7.1) for $n_2 < 1$).

The trend shown in Fig. 7.1 does not correspond to all welding spot arrangements. In mixed-type pillow plates (cf. Sec. 5.2), the recirculation zones grow in size with the Reynolds number, thus strongly influencing the form drag coefficient. This results in a complex dependency between the Darcy friction factor and Reynolds number (Figs. 5.16, 5.17 and 7.3). Therefore, a more complex description for $\zeta_{\Delta p} = f(Re)$ than by Eq. (7.1) is necessary.

Equation (7.1) has two adjustable parameters, which represent functions of the pillow-plate geometry parameters s_T, s_L, d_{SP} and δ_i. These can be used to build the following dimensionless

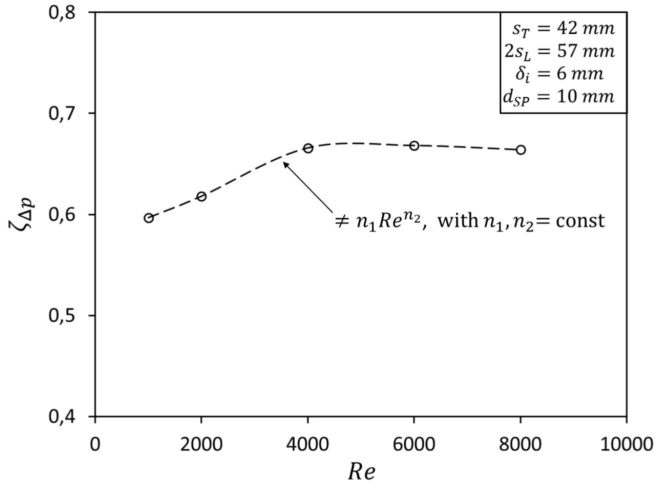

Figure 7.3: Darcy friction factor $\zeta_{\Delta p}$ as a function of the Reynolds number for turbulent, single-phase flow in a mixed-type pillow plate (cf. Sec. 5.2).

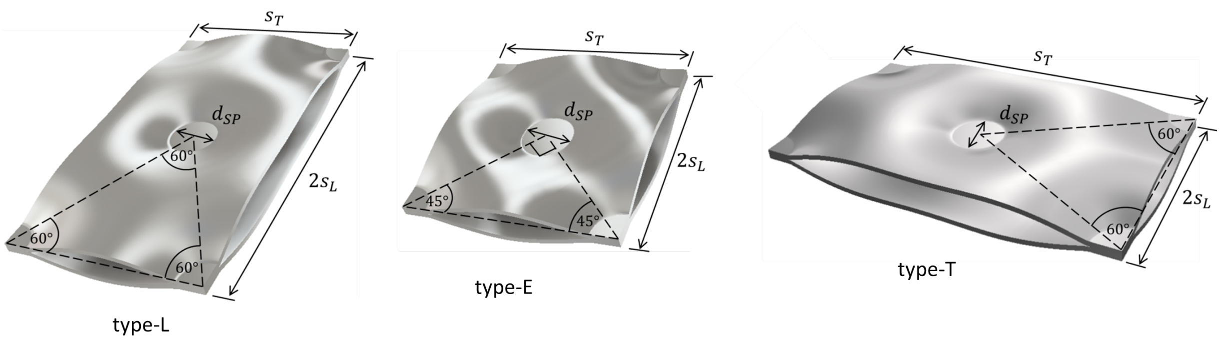

Figure 7.4: Main types of welding spot arrangements of pillow plates.

combinations:

$$a = \frac{2s_L}{s_T} \tag{7.2}$$

$$b = \frac{d_{SP}}{s_T} \tag{7.3}$$

$$c = \frac{\delta_i}{s_T} \tag{7.4}$$

The range of possible variation of a, b and c is very broad. Therefore, in this work, the investigation was limited to a practically relevant range, which includes the three main types of welding spot arrangements of pillow plates available on the market. These arrangements are represented by type-L ($a = \sqrt{3}$), type-E ($a = 1$) and type-T ($a = 1/\sqrt{3}$) patterns shown in Fig. 7.4. Patterns with other ratios are hardly encountered in industry. In Sec. 5.2, a similar classification was used and related to the flow patterns observed in the pillow-plate channels, namely, type-L corresponds to “longitudinal-type” pillow plates ($s_r = (a - b)/(1 - b) \geq 1.56$), while type-T and type-E correspond to “transversal-type” ($s_r \leq 1$).

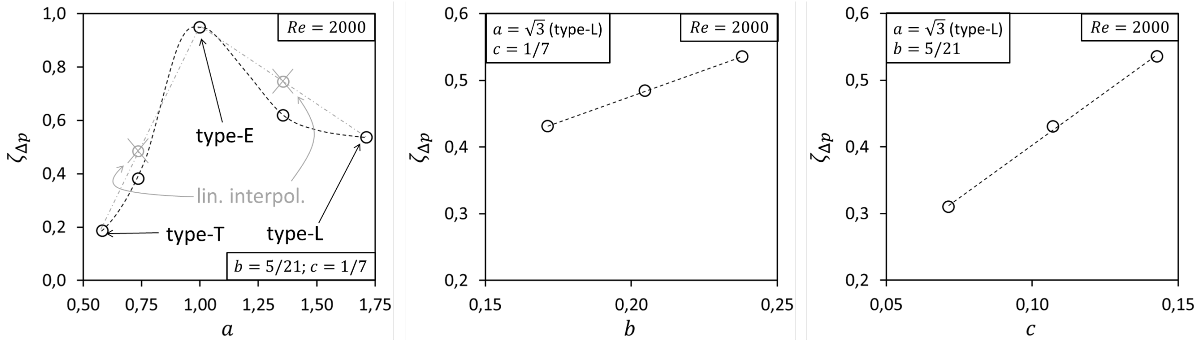

Figure 7.5: Influence of the dimensionless welding spot arrangement (left), welding spot diameter (middle) and inflation height of the pillows (right), on the Darcy friction factor in pillow-plate channels. The results are shown for some representative sets of geometrical parameters.

The influence of the characteristic geometry parameters on the Darcy friction factor (obtained from the CFD simulations presented in Sec. 5.2) was analyzed using Fig. 7.5, where $\zeta_{\Delta p}$ is plotted against a (Fig. 7.5 (left)), b (Fig. 7.5 (middle)) and c (Fig. 7.5 (right)).

It is visible that the geometry parameters have a large influence on $\zeta_{\Delta p}$, which results in a strong variation of the values of n_1 and n_2 in Eq. (7.1). Fig. 7.5 (left) shows that the relation between $\zeta_{\Delta p}$ and the welding spot pattern is quite complex. There is a maximum in $\zeta_{\Delta p}$ for type-E welding spot patterns when $2s_L = s_T$. Furthermore, an approximation of the value of $\zeta_{\Delta p}$ for mixed-type pillow plates ($a \approx 0.75$ and $a \approx 1.37$) by interpolating linearly between the values for pillow-plates with a triangular (type-L and type-T) and equidistant welding spot pattern is not recommended (cf. Fig. 7.5). This can lead to a deviation of up to 75%, compared to the value of $\zeta_{\Delta p}$ from CFD simulations. As was demonstrated in Sec. 5.2, triangular welding spot patterns lead to the highest thermo-hydraulic efficiency, while type-E patterns provide the largest heat transfer coefficient at equal pumping power. Mixed-type geometries do not seem to offer any specific advantages. In order to reduce complexity of the design equations developed in this work, mixed-type geometries were excluded from considerations.

The dependence of $\zeta_{\Delta p}$ on the welding spot diameter (Fig. 7.5 (middle)) and on the inflation height of the pillows (Fig. 7.5 (right)) is almost linear. Consequently, an approximation of $\zeta_{\Delta p}$ for intermediate values of b and c by linear interpolation is possible. The adjustment parameters n_1 and n_2 in Eq. (7.1) were estimated by plotting $\zeta_{\Delta p}$ (evaluated from CFD simulations presented in Sec. 5.2) over the Reynolds number for different geometry parameters a, b and c. As mixed-type geometries were not considered, no continuous function for $\zeta_{\Delta p}$ with the welding spot arrangement was developed. Moreover, a continuous function would lead to complex mathematical expressions, which are rather difficult for practical use. Instead, separate design equations were developed for triangular (type-L and type-T) patterns and for equidistant (type-E) patterns. These equations are discussed in the following sections.

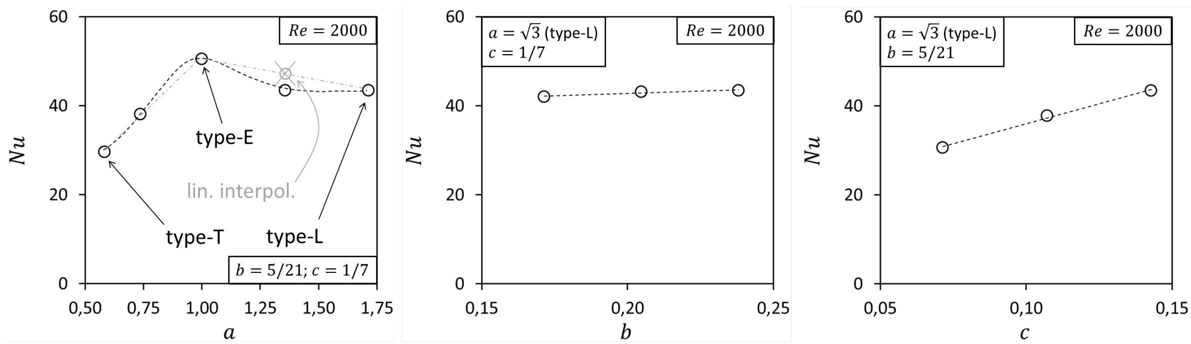

Figure 7.6: Influence of the dimensionless welding spot arrangement (left), welding spot diameter (middle) and inflation height of the pillows (right), on the Nusselt number in pillow-plates channels. The results are shown for some representative sets of geometrical parameters.

7.1.2 Design methods for heat transfer

In this work, two different approaches for the thermal design of pillow plates were developed and tested. The first approach is based on a simple Dittus-Boelter type power-law function, while the coefficients of this expression are determined by regression analysis using the heat transfer coefficients obtained from the detailed CFD simulations presented in Sec. 5.2. This is the most common procedure in literature to represent heat transfer coefficients. However, as already mentioned in Chap. 3.2, there is still some scepsis concerning the validity of Dittus-Boelter type correlations.

In order to overcome the drawbacks of Dittus-Boelter type functions, a second approach was developed, which is based on the analysis of the characteristic flow pattern in pillow-plate channels. This approach has a stronger connection to the actual flow structure in pillow-plate channels and it can be extended to other complex flows. Such methods could not easily be developed in the past; today, available advanced CFD methods are capable of providing detailed flow information, which opens the path for new modeling strategies.

Following the analysis performed with Fig. 7.5 for pressure loss, in Fig. 7.6, the Nusselt number was plotted over characteristic geometry parameters of pillow plates. The conclusions drawn from the analysis of Fig. 7.6 are qualitatively similar to those from Fig. 7.5. However, compared to $\zeta_{\Delta p}$, a linear interpolation of Nu for intermediate welding spot patterns ($a \approx 0.75$ and $a \approx 1.37$) leads to a smaller deviation (less than 12%). Furthermore, the influence of the welding spot diameter b on Nu is marginal (Fig. 7.6 (middle)).

The power-law approach

Following Dittus-Boelter [16], the Nusselt number can be represented by a power-law type equation (cf. Eq. (3.23)):

$$Nu = n_3 Re^{n_4} Pr^{n_5} \tag{7.5}$$

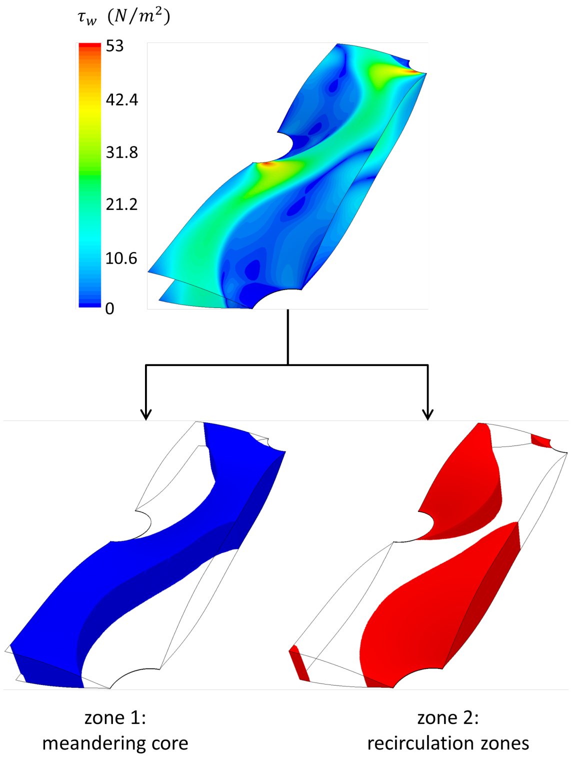

Figure 7.7: Basic idea to represent the characteristic flow pattern in pillow-plate channels into two separate zones.

In Eq. (7.5), the parameters n_3, n_4 and n_5 are functions of the pillow-plate geometry and need to be fitted to the numerical data provided by CFD in Sec. 5.2. Equation (7.5) is simple and easy to use, however, as already mentioned above, it lacks physical background.

Development of the flow-pattern oriented approach: the "2-zone-model"

CFD simulations presented in Sec. 5.2 show that the flow in pillow-plate channels can be subdivided into characteristic zones, namely, a meandering core flow (zone 1), which dominates heat transfer, and recirculation zones (zone 2), which are formed in the wake of the welding spots (cf. Fig. 5.12). Heat transfer is poor in zone 2. This can be seen by the normalized wall heat flux shown in Fig. 5.12. Consequently, the meandering core flow is the main contributor to heat transfer in pillow-plate channels. The identification of these two characteristic zones led to the development of a flow pattern oriented model for the prediction of heat transfer coefficients. The basic idea of this model is shown in Fig. 7.7.

Boundary layers in zone 1 are turbulent and hydro-dynamically and thermally fully developed. For this type of a boundary layer, numerous Nusselt correlations have been developed in the past (e.g. Petukhov and Popov [31], Colburn [59] and Dittus and Boelter [16]), as already mentioned in Chap. 3.2. Hence, by subdividing the flow pattern into two different regions it is possible to apply existing, robust correlations, e.g. the correlations for turbulent forced convection heat transfer in pipes, to zone 1. The recirculation regions (zone 2) can be accounted for by a correction factor.

The meandering core is separated from the total flow in a post-processing stage of the CFD simulations. Figure 7.7 shows schematically the results of the partitioning. The "virtual boundary" between the two zones coincides with the location of the shear layer between zones 1 and 2. This boundary is found using the scalar 2D-field of the wall shear stress $|\tau_w|$ (Fig. 7.7). In the meandering core, $|\tau_w|$ is largest and in the recirculation zones it approaches zero. In the shear layer between the two zones, $|\tau_w|$ varies strongly.

- **Modeling of the meandering core flow (zone I)**

  As mentioned above, the boundary layers in zone 1 are fully turbulent (for $1000 \leq Re \leq 8000$) and hydro-dynamically and thermally fully developed. For this type of boundary layer, Petukhov and Popov [31] suggested a semi-empirical Nusselt correlation (cf. Eq. (3.26)):

$$Nu = \frac{(\zeta_f/8)\, RePr}{1.07 + 12.7\sqrt{(\zeta_f/8)}\left(Pr^{2/3} - 1\right)} \tag{7.6}$$

  Eq. (7.6) was originally developed for turbulent forced convection heat transfer in pipes and it is up to date the most successful and widely used Nusselt correlation for this type of flow. Eq. (7.6) is a heat transfer analogy; it is based on the assumption that the mechanisms of momentum transfer and heat transfer are similar in fully developed turbulent boundary layers. For this reason, it is possible to predict heat transfer coefficients only from knowledge of frictional losses. Compared to purely empirical formulations, such as by Dittus and Boelter [16], Steimle [26] or Colburn [59], which are mostly based on fitting heat transfer data to power law expressions, Eq. (7.6) provides higher accuracy and a larger range of validity. Although Eq. (7.6) was suggested for flow in pipes, it is generally applicable to flow in any geometry, where regions of hydro-dynamically and thermally fully developed turbulent boundary layers exist.

  In order to apply Eq. (7.6) to the meandering core for the prediction of heat transfer coefficients, zone 1 was simplified to an equivalent "tube" geometry (Fig. 7.8). The tube diameter was set equal to the hydraulic diameter of zone 1 ($d_{tube} = d_{h,z1}$). The length of the tube was chosen to be equal to the arc-length of the sine-curve $s(x)$. This curve describes the shape of the meandering core.

  The analogy of Petukhov and Popov [31] is applied to zone 1 by employing the hydraulic diameter $d_{h,z1}$, the Reynolds number Re_{z1} and the friction factor ζ_{z1} of zone 1 in Eq. (7.6):

$$Nu_{z1} = \frac{(\zeta_{f,z1}/8)\, Re_{z1}Pr}{1.07 + 12.7\sqrt{(\zeta_{f,z1}/8)}\left(Pr^{2/3} - 1\right)} \tag{7.7}$$

  With Eq. (7.7), heat transfer coefficients can be determined for the meandering core. The parameters $d_{h,z1}$, Re_{z1} and ζ_{z1} were obtained from the CFD simulations presented in Sec. 5.2.

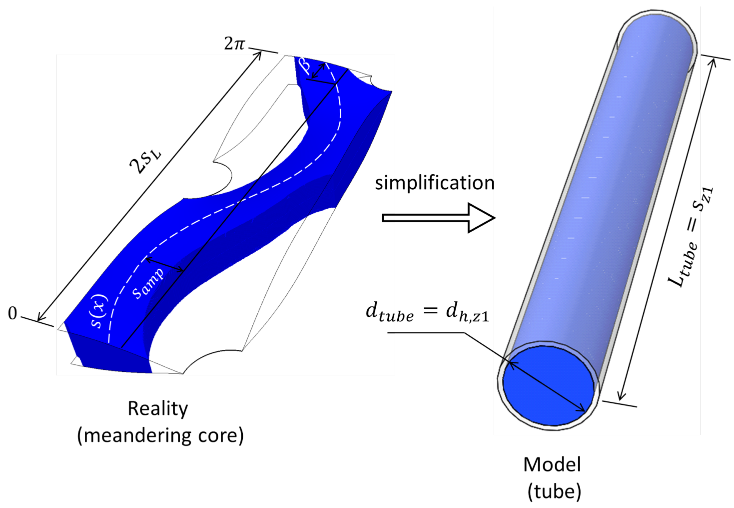

Figure 7.8: Illustration of the simplification of the meandering core flow into an analogous "model tube".

The mean hydraulic diameter of zone 1 was evaluated by:

$$d_{h,z1} = \frac{4V_{z1}}{A_{w,z1}} \tag{7.8}$$

Eq. (7.8) represents a volumetric hydraulic diameter (cf. Eq. (4.1)), which is a function of the fluid volume V_{z1} and the wetted wall area $A_{w,z1}$ in zone 1. The mean stream velocity in this zone is determined by:

$$u_{m,z1} = \frac{\dot{V}_{z1}}{A_{cs,z1}} \tag{7.9}$$

In Eq. (7.9), $\dot{V}_{z1}$ is the volumetric flow rate in zone 1 and $A_{cs,z1}$ is the mean cross-sectional area. It was assumed that $\dot{V}_{z1}$ is equal to the total volumetric flow rate V_{tot} in the pillow-plate channel, since fluid in the recirculation zones is "trapped" there and, consequently, does not exchange mass with the meandering core. Using Eq. (7.8) and Eq. (7.9), the mean Reynolds number in zone 1 can be calculated as follows:

$$Re_{z1} = \frac{u_{m,z1} d_{h,z1}}{\nu} \tag{7.10}$$

Finally, the mean friction factor in zone 1 was evaluated using a Blasius-type power law function [22]:

$$\zeta_{f,z1} = n_6 Re^{n_7} \tag{7.11}$$

The coefficient n_6 and the exponent n_7 are functions of the welding spot pattern and the inflation height; they were fitted to the simulated friction factors in zone 1 obtained in Sec. 5.2.

- **Modeling of the total channel**

As shown above, the meandering core can be modeled using Eq. (7.7). However, Eq. (7.7) is only applicable to this region. To complete the 2-zone model a link between zone 1 and the total channel is required together with a model for the recirculation zones. Such a link was established by an energy balance over the surface of the channel walls:

$$\dot{Q}_{tot} = \dot{Q}_{z1} + \dot{Q}_{z2} \tag{7.12}$$

Equation (7.12) states that the total heat flow rate $\dot{Q}_{tot}$ transferred to the channel surface is equal to the sum of heat flow rates transferred to the surfaces covered by the meandering core $\dot{Q}_{z1}$ and by the recirculation zones $\dot{Q}_{z2}$. Equation (7.12) can be rearranged into the following equation,

$$\dot{Q}_{tot}\,(1 - \psi_Q) = \dot{Q}_{z1} \tag{7.13}$$

by introducing the dimensionless variable ψ_Q (Eq. (5.12)), which represents the ratio of heat transferred in the recirculation zones to the total heat flow rate. The heat flow rates $\dot{Q}_{tot}$ and $\dot{Q}_{z1}$ can also be determined using Newton's law of cooling:

$$\dot{Q}_{tot} = h_{tot} A_{w,tot} \Delta T_{tot} \tag{7.14}$$
$$\dot{Q}_{z1} = h_{z1} A_{w,z1} \Delta T_{z1} \tag{7.15}$$

The term ΔT_{tot} in Eq. (7.14) represents the mean temperature difference between the bulk and wall temperatures, while ΔT_{z1} is the mean temperature difference between the bulk and wall temperatures in zone 1 only. Since the meandering core mainly contributes to heat transfer in the pillow-plate channel, it was assumed that the following relationship is valid:

$$\Delta T_{tot} \approx \Delta T_{z1} \tag{7.16}$$

The approximation in Eq. (7.16) could be verified by the CFD simulations. Furthermore, the relationship between the total surface area of the channel and the surface area covered by zone 1 is:

$$A_{w,z1} = A_{w,tot}\,(1 - \psi_A) \tag{7.17}$$

where the dimensionless variable ψ_A (Eq. (5.11)) in Eq. (7.17) is used to evaluate the size of the recirculation zones. Using Eqs. (7.13) to (7.17), the heat transfer coefficient in the total channel h_{tot} can be determined based on the heat transfer coefficient in zone 1:

$$h_{tot} = h_{z1}\left(\frac{1 - \psi_A}{1 - \psi_Q}\right) \tag{7.18}$$

As mentioned above, ψ_Q reflects the contribution of the recirculation zones to heat transfer in the pillow-plate channel. It was evaluated by CFD.

The variables ψ_A and ψ_Q are functions of the welding spot pattern, the inflation height and the Reynolds number. However, as shown in Sec. 5.2, they depend only weakly on the Reynolds number. Hence, simplified functions were derived for ψ_A and ψ_Q, which depend on geometrical parameters only.

- **Determination of Re_{z1} based on Re_{tot}**

The mean Reynolds number in zone 1 can be determined based on the mean Reynolds number for the total channel. The former is determined by Eq. (7.10) and the latter by Eq. (5.3). Dividing Eq. (7.10) by Eq. (5.3) leads to:

$$\frac{Re_{z1}}{Re_{tot}} = \frac{u_{m,z1} d_{h,z1}}{u_m d_h} \tag{7.19}$$

In order to evaluate $u_{m,z1}$, it was assumed that $\dot{V}_{z1}$ is equal to the total volumetric flow rate $\dot{V}_{tot}$ in the pillow-plate channel, as mentioned above. This assumption leads to:

$$\dot{V}_{z1} = u_{m,z1} A_{cs,z1} = u_m A_{cs,tot} = \dot{V}_{tot} \tag{7.20}$$

The ratio of the mean stream velocities $u_{m,z1}/u_m$ in Eq. (7.19) is evaluated by:

$$\frac{u_{m,z1}}{u_m} = \frac{A_{cs,tot}}{A_{cs,z1}} \tag{7.21}$$

The mean cross-sectional area of the total channel $A_{cs,tot}$ is determined using Eq (4.2) ($A_{cs,tot} = \overline{A}_{cs,tot}$, over-bar omitted here for better readability). For $A_{cs,z1}$, it is important to differentiate between transversal-type and longitudinal-type pillow plates (see Sec. 5.2.4). For the latter, the meandering core is deflected more strongly around the welding spots (Fig. 7.8). As a result, the length of the flow path of zone 1 is longer compared to transversal-type pillow plates. In order to evaluate this length, it was assumed that the shape of the meandering core can be approximated by a sine-curve:

$$s(x) = s_{amp} \sin\left(\frac{x\pi}{s_L} + \beta\right) \tag{7.22}$$

In Eq. (7.22), s_{amp} represents the amplitude and β the phase shift. The length of the flow path of zone 1 is evaluated by the arc-length s_{z1} of the sine-curve:

$$s_{z1} = \int\limits_{0}^{2s_L} \sqrt{1 + s'(x)^2} dx \tag{7.23}$$

The ratio of the arc-length to the longitudinal pitch is given by:

$$s^* = \frac{s_{z1}}{2s_L} \tag{7.24}$$

Consequently, for transversal-type pillow plates $s^* = 1$ and for longitudinal-type pillow plates $s^* > 1$. The cross-sectional area of the meandering core can then be determined by:

$$A_{cs,z1} = \frac{V_{z1}}{2s_L s^*} \tag{7.25}$$

With Eq. (4.2) and (7.25), Eq. (7.21) can be rearranged as follows:

$$\frac{u_{m,z1}}{u_m} = \frac{V_{tot}}{V_{z1}} s^* \tag{7.26}$$

The ratio of the hydraulic diameters in Eq. (7.19) can be evaluated using Eq. (7.17):

$$\frac{d_{z1}}{d_h} = \frac{4V_{tot}/A_{w,z1}}{4V_{z1}/A_{w,tot}} = \frac{V_{z1}}{V_{tot}} \left(\frac{1}{1 - \psi_A}\right) \tag{7.27}$$

Finally, Eq. (7.19) can be rearranged to:

$$\frac{Re_{z1}}{Re_{tot}} = \frac{s^*}{1-\psi_A} \tag{7.28}$$

With Eq. (7.28), the Reynolds number in zone 1 can be calculated using the Reynolds number for the total channel.

Modeling of variable physical properties

This section is common for both design approaches. When physical properties vary significantly within the boundary layer due to their strong temperature dependence, the heat transfer rate is affected. In such cases, the correction proposed by Sieder and Tate [60] is commonly applied:

$$Nu_T = Nu\left(\frac{Pr}{Pr_w}\right)^{0.11} \tag{7.29}$$

Eq. (7.29) is used for turbulent heat transfer in liquids in channel flow, where Pr is the Prandtl number evaluated for the bulk temperature, while Pr_w represents the Prandtl number determined at the wall temperature. The exponent 0.11 is common for pipe flow.

The influence of variable physical properties on the heat transfer coefficient in pillow-plate channels was evaluated based on a CFD study. In this work, the same technique as in Sec. 5.2 was applied, yet the dynamic viscosity $\mu = f(T)$, the thermal conductivity $\lambda = f(T)$ and the specific heat capacity $c_p = f(T)$ of water were specified as polynomial functions of temperature using the data obtained from the database Refprop [61]. In the simulations, the ratio T_w/T_B was varied between 1.023 and 1.087. The results of these simulations were then used to test the applicability of Eq. (7.29) for pillow plates.

Figure 7.9 shows relative deviations between heat transfer coefficients calculated with Eq. (7.18) and Eq. (7.29) and those obtained by CFD simulations. As can be seen, this deviation rises significantly, when Eq. (7.18) is applied (dash line). In contrast, Eq. (7.29) works well for pillow plates, with the almost constant relative deviation $< 2\%$ (solid line).

7.1.3 Adjustment of correlation parameters and method validation

The adjusted parameters n_1 to n_7, ψ_A, ψ_Q, $d_{h,z1}$ and s^* in the design equations for pressure loss and heat transfer were obtained by regression analysis, using the Darcy friction factors and Nusselt numbers from the CFD simulations shown in Sec. 5.2.

Within the variation range of a, b and c considered in the present work, it was found that the dependence of the Darcy friction factors and the Nusselt numbers on the geometry parameters b and c is nearly linear. Hence, it was possible to adapt simple linear functions for the adjustment parameters mentioned above to approximate the numerical data.

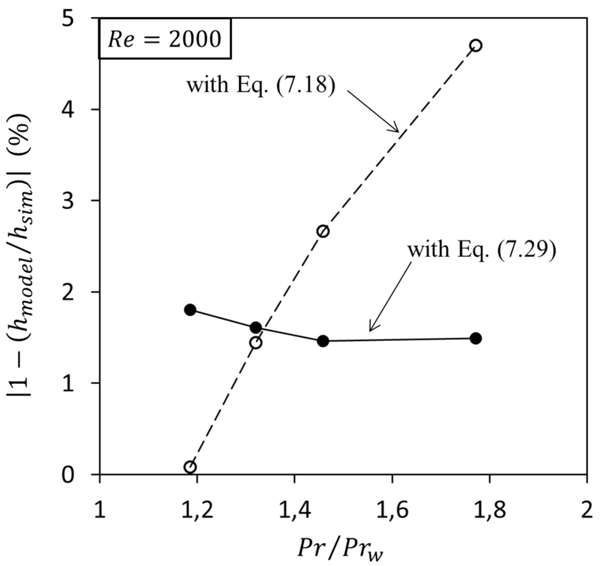

Figure 7.9: Relative deviation of heat transfer coefficients determined using Eq. (7.18) or (7.29) from heat transfer coefficients evaluated by CFD simulations, plotted against the Prandtl number ratio Pr/Pr_w.

Furthermore, the effect of the welding spot diameter on the Darcy friction factor and heat transfer coefficient was investigated for different welding spot arrangements a, while keeping inflation height c constant. The qualitative relation $\zeta_{\Delta p} = f(b)$ and $h = f(b)$ was assumed to be similar for all inflation heights. However, this has not yet been verified by CFD or experiment.

The hydraulic diameter and the mean stream velocity in the pillow-plate channel were determined by the following expressions:

$$d_h = 1.06 d_{h0} \tag{7.30}$$

$$u_m = 0.94 u_{m0} \tag{7.31}$$

where d_{h0} and u_{m0} denote the hydraulic diameter and the mean stream velocity in pillow-plate channels determined using the methods proposed in Chapt. 4. The marginal deviations between d_h and d_{h0} and between u_m and u_{m0} arise from the difference in the determination of the inner channel volume V_{tot} in Chapt. 4 and in the simulations in Sec. 5.2. In the latter, a small extrusion (0.05 mm) of the welding spot was necessary in order to generate a high quality mesh in the vicinity of the welding spots, where the channel becomes very narrow. Such an extrusion is also observed in reality as a result of the welding process; however, it is small and has no significant effect on the flow.

Table 7.1: Coefficients n_1 and n_2 in Eq. (7.1) used for the prediction of pressure loss. The validity range for the Reynolds number is $1000 \leq Re \leq 8000$.

	$\zeta_{\Delta p} = n_1 Re^{n_2}$		
	$a \approx 0.58$ $\begin{pmatrix} 0.1 \leq b \leq 0.14 \\ 0.042 \leq c \leq 0.083 \end{pmatrix}$	$a \approx 1$ $\begin{pmatrix} 0.17 \leq b \leq 0.24 \\ 0.071 \leq c \leq 0.143 \end{pmatrix}$	$a \approx 1.71$ $\begin{pmatrix} 0.17 \leq b \leq 0.24 \\ 0.071 \leq c \leq 0.143 \end{pmatrix}$
n_1	$8.74b + (17c + 0.73)$	$-15.3b + (1.4c + 5.4)$	$1.35b + (2.8c + 0.92)$
n_2	-0.38	$1.725b + (1.11c - 0.66)$	$0.3b + (0.53c - 0.29)$

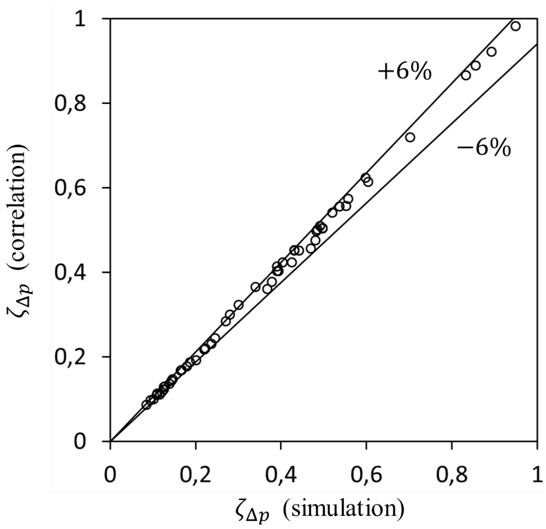

Figure 7.10: Comparison of Darcy friction factors obtained by simulation in Sec. 5.2 and by Eq. (7.1) with coefficients from Tab. 7.1.

Parameters of $\zeta_{\Delta p}$

The best fit functions used to approximate the parameters n_1 and n_2 in Eq. (7.1) for the Darcy friction factor in pillow-plate channels are presented in Tab. 7.1. Validation results for the design equation for pressure loss is shown in Fig. 7.10.

As can be seen in Fig. 7.10, pressure loss in pillow-plate channels can be predicted with good accuracy using the proposed equations, with a maximum relative deviation of $\pm 6\%$.

Parameters of the power-law correlation

The best fit functions used to approximate the parameters n_3, n_4 and n_5 for the power-law model (Eq. (7.5)) are presented in Tab. 7.2.

The exponent n_5 of the Prandtl number is generally a function of the characteristic geometry parameters of the pillow plate. However, it was found that n_5 varies with a, b and c only weakly ($\approx 0.38 - 0.42$). Hence, an average value $n_5 = 0.4$ was adopted. This assumption leads to a deviation of only $\pm 5\%$ compared to the Nusselt numbers calculated using the exact value of n_5.

Table 7.2: Coefficients n_3 to n_5 used in Eq. (7.5) for the prediction of heat transfer coefficients. The validity range for the Reynolds number is $1000 \leq Re \leq 8000$ and for the Prandtl number $1 \leq Pr \leq 150$.

	$Nu = n_3 Re^{n_4} Pr^{n_5}$		
	$a \approx 0.58$ $\begin{pmatrix} 0.1 \leq b \leq 0.14 \\ 0.042 \leq c \leq 0.083 \end{pmatrix}$	$a \approx 1$ $\begin{pmatrix} 0.17 \leq b \leq 0.24 \\ 0.071 \leq c \leq 0.143 \end{pmatrix}$	$a \approx 1.71$ $\begin{pmatrix} 0.17 \leq b \leq 0.24 \\ 0.071 \leq c \leq 0.143 \end{pmatrix}$
n_3	$0.0775b + (0.38c + 0.005)$	$0.03b + (0.76c - 0.032)$	$-0.163b + (0.711c + 0.022)$
n_4	0.75	$-1.12c + 0.905$	$0.29b + (-c + 0.8)$
n_5	0.4	0.4	0.4

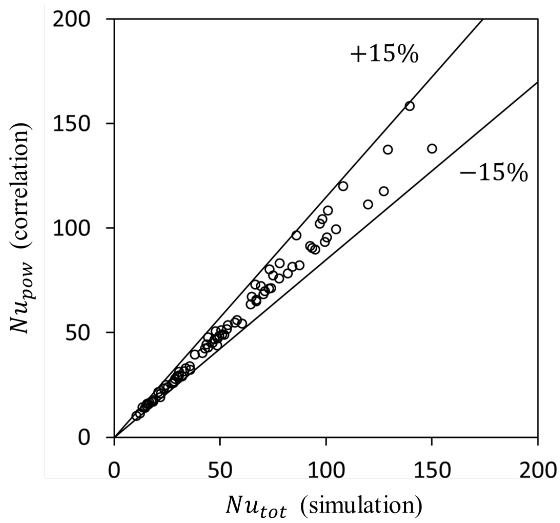

Figure 7.11: Comparison of Nusselt numbers obtained by simulation in Sec. 5.2 with those determined using the power-law model summarized in Tab. 7.2.

A validation of the power-law correlation using heat transfer coefficients evaluated by the CFD simulations, is shown in Fig. 7.11.

The simulated Nusselt numbers are predicted with a relative deviation of $\pm 15\%$.

Parameters of 2-zone model

The best fit functions used to approximate the parameters n_6, n_7, ψ_A, ψ_Q and $d_{h,z1}$ of the two-zone model are presented in Tab. 7.3.

The exponent n_7 of the Fanning friction factor in zone 1 proved to be independent of b and c for any fixed welding spot arrangement a. Since the meandering core is hardly deflected in transversal-type ($a \approx 0.58$) and equidistant-type ($a \approx 1$) geometries, the factor s^* was set equal to 1. It is important to mention, that for small Prandtl numbers ($Pr < 5$), the Nusselt correlation presented in [31] is more accurate than that given by Eq. (7.7). A validation of the two-zone model is shown in Fig. 7.12.

Table 7.3: Equations and model adjustment parameters required within the 2-zone model for the prediction of heat transfer coefficients. The validity range for the Reynolds number is $1000 \leq Re \leq 8000$ and for the Prandtl number $1 \leq Pr \leq 150$.

$$\zeta_{f,z1} = n_6 Re^{n_7}$$

$$Re_{z1} = Re\left(\frac{s^*}{1-\psi_A}\right)$$

$$Nu_{z1} = \frac{(\zeta_{f,z1}/8)\, Re_{z1} Pr}{1.07 + 12.7\sqrt{(\zeta_{f,z1}/8)}\left(Pr^{2/3}-1\right)} \quad ^{a}$$

$$h = h_{z1}\left(\frac{1-\psi_A}{1-\psi_Q}\right)$$

	$a \approx 0.58$ $\begin{pmatrix} 0.1 \leq b \leq 0.14 \\ 0.042 \leq c \leq 0.083 \end{pmatrix}$	$a \approx 1$ $\begin{pmatrix} 0.17 \leq b \leq 0.24 \\ 0.071 \leq c \leq 0.143 \end{pmatrix}$	$a \approx 1.71$ $\begin{pmatrix} 0.17 \leq b \leq 0.24 \\ 0.071 \leq c \leq 0.143 \end{pmatrix}$
n_6	$4.36c + 1.14$	$2.52c + 0.24$	$4.62c + 0.6$
n_7	-0.44	-0.3	-0.34
ψ_A	$0.94b + 0.4$	$0.75b + 0.46$	$0.81b + 0.263$
ψ_Q	$2.16b + (4.23c - 0.352)$	$0.75b + (1.54c - 0.014)$	$0.46b + (1.17c - 0.042)$
$d_{h,z1}$	$-11.22b + (113c + 1.82)$	$-18.31b + (35.42c + 4.8)$	$-8.1b + (60c + 2.1)$
s^*	1	1	1.0761

[a] If $Pr < 5$, $Nu_{z1} = \frac{(\zeta_{f,z1}/8) Re_{z1} Pr}{1+3.4\zeta_{f,z1}+\left(11.7+1.8Pr^{-1/3}\right)\sqrt{(\zeta_{f,z1}/8)}\left(Pr^{2/3}-1\right)}$ [31]

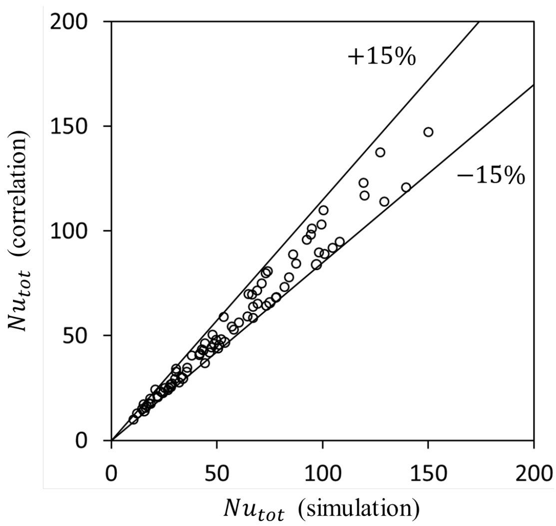

Figure 7.12: Comparison of Nusselt numbers obtained by simulation in Sec. 5.2 with those determined using the 2-zone model summarized in Tab. 7.3.

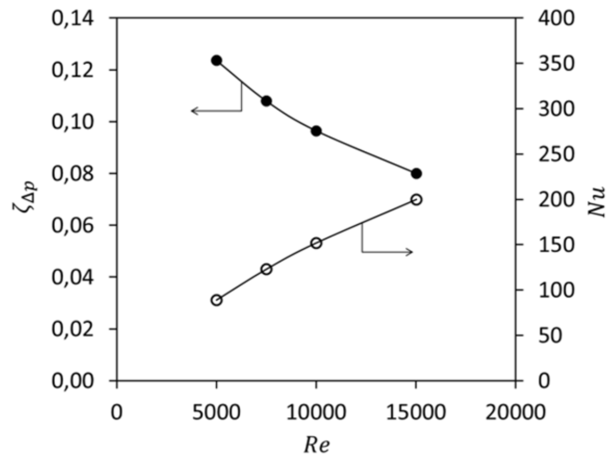

Figure 7.13: Plot of the Darcy friction factor and Nusselt number in the outer pillow plate channel as a function of the Reynolds number.

As can be seen, the two-zone model predicts the simulated Nusselt numbers in pillow-plate channels with a good accuracy. The maximum relative deviation is $\pm 15\%$.

7.2 Design methods for the outer channels of PPHE

Using the CFD simulations, functional dependence of the Darcy friction factor $\zeta_{\Delta p}$ and the Nusselt number Nu for $5000 \leq Re \leq 15000$ could be obtained. They are shown in Fig. 7.13.

The best fit for the Darcy friction factor for the outer channel is represented by

$$\zeta_{\Delta p} = 3.46 Re^{-0.39} \tag{7.32}$$

with a maximum deviation of 2%. The best fit for the Nusselt number for the outer channel is give by

$$Nu = 0.091 Re^{0.74} Pr^{1/3} \tag{7.33}$$

also with a maximum deviation of 2%. Actually, Eq. (7.33) was obtained for $Pr = 6$. The exponent of the Prandtl number was then assumed to be 1/3, because it is a typical value for turbulent boundary layers in forced convection heat transfer (see, e.g., Dittus-Boelter equation in [16]).

7.3 Conclusions

In this chapter, new design equations for the determination of pressure loss and heat transfer coefficients describing turbulent forced convection in the inner and outer channels of pillow-plate heat exchangers were developed. The equations for the inner channels cover a wide range of Reynolds numbers, Prandtl numbers and variations of the characteristic geometry parameters. The equations for the outer channels are strictly valid for one set of characteristic geometry parameters of pillow plates.

For the determination of heat transfer coefficients in the inner channels, two different methods are presented. The first is based on a simple Dittus-Boelter type power-law function for the Nusselt number. The second model is based on the characteristic flow pattern in pillow-plate channels. It is denoted the 2-zone model, since the original flow pattern is broken down into two simpler flows, which are then modeled separately. Results of both methods were then compared to Nusselt numbers obtained by the CFD simulations, with relative deviations in the range of $\pm 15\%$.

Furthermore, the equation of Sieder and Tate [60], which is commonly used for the determination of Nusselt number under the condition of variable physical properties, was tested for heat transfer in pillow-plate channels. It was shown that this equation is applicable for pillow plates.

A better accuracy can be achieved with the 2-zone model when the dependency of the recirculation zones from the Prandtl number is considered. The separation of the flow pattern in two zones within this model can be advantageous, when coupled problems covering the outer pillow-plate channels are considered, e.g. condensation or falling film evaporation.

8 Concluding remarks

In this work, fluid dynamics and heat transfer in pillow-plate heat exchangers (PPHE) were studied using experiments and comprehensive CFD simulations. The latter formed the bulk of this work, whereas the experiments were mainly used for validation purposes and for the investigation of flow regimes not easily resolvable with CFD (e.g. transitional flow regime).

The experimental study was performed using two different experimental facilities with the goal of validating the numerical model both qualitatively and quantitatively. The first one focused on flow visualization. It encompassed a transparent pillow-plate channel, which enabled a comparison between the flow patterns observed experimentally and obtained by CFD simulations. The results from the first facility showed that CFD is capable of accurately capturing the flow pattern in pillow-plate channels. Both facilities were used to measure pressure in pillow plates, whereas the second experimental set-up was used to also measure heat transfer coefficients in pillow plates. The CFD simulations proved to accurately capture these quantities as well.

The realistic description of the fluid dynamics in PPHE using CFD methods, requires an accurate reconstruction of the wavy pillow-plate channels. This was achieved by forming simulations based on Finite-Element-Analysis (FEA), using the commercial solver ABAQUS. A validation of the method was carried out by comparing the simulated wavy profiles of the pillow plates with those of a real pillow plate, measured using a contour gauge. The deviation between the simulation and the measurement was less than 4%. The numerical results were then used to develop simple equations for the accurate determination of the geometrical design parameters: mean hydraulic diameter, mean cross-sectional area and heat transfer area for the inner channel of a pillow plate and for the channel between adjacent pillow plates. The simulation results also show that the surface area enlargement caused by the surface waviness is marginal compared to a plane surface ($2 - 7\%$).

In the next step, a thorough CFD analysis of fluid dynamics and heat transfer in pillow plates was carried out, using the commercial solver STAR-CCM+. The numerical results were validated successfully against experiments. Two different test facilities were used to validate the CFD simulations, one to visualize the flow in a unique transparent pillow-plate channel, and another one, to perform measurement of pressure loss and heat transfer coefficients in a pillow plate.

The simulations showed that the fully developed turbulent flow in pillow plates is characterized by two distinctive regions, namely (a) recirculation zones arising in the wake of the welding spots and (b) the core flow, which is bounded by the walls and the recirculation zones. The latter flow represents a primary effect while the former is secondary. The secondary flow produces form drag, which increases pressure loss in the channel. Depending on the geometry, three subcategories of the characteristic flow pattern, a longitudinal-type, transversal-type and mixed-type pillow plates, could be identified. They differ mainly in the size and shape of the recirculation zones. While the characteristic flow pattern in longitudinal-type and transversal-type pillow plates is only weakly dependent on the Reynolds number, in mixed-type pillow plates, the recirculation zones increase significantly in size with rising Reynolds number.

Furthermore, the thermo-hydraulic efficiency of pillow plates was investigated. The largest efficiencies were observed at the lowest Reynolds number and decreased rapidly at larger Reynolds numbers. This effect is caused by the fact that, with increasing Reynolds number, pressure loss grows more rapidly than the heat transfer coefficient. The lowest efficiencies were observed for pillow plates, in which the longitudinal and transversal welding spot pitches were equal, whereas the highest efficiencies were obtained for transversal-type pillow plates with the larger inflation height.

A geometry based optimization study for improving the thermo-hydraulic efficiency of pillow plates was performed. It was found, that by using “oval-shaped” welding spots, which are more streamlined than round ones, the efficiency can be increased by as much as 37% for longitudinal-type pillow plates and by 22% for transversal-type pillow plates. Even greater improvements in the efficiency were found for reduced-size welding spots.

The flow in the inner channel is largely determined by the geometry of the channel walls, and boundary layer separation depends mainly on the geometry, yet only weakly on the Reynolds number. However, in the outer channel, boundary layer separation occurs over the smooth curved surface of the pillow plates. Most linear eddy viscosity models are unable to accurately predict boundary layer separation and re-attachment in such cases and, hence, tend to underpredict or overpredict pressure loss and heat transfer rate. For this reason, the elliptic blending $k-\varepsilon$ model was adopted for the outer channel. This model is more advanced, and it was capable of predicting the measurements of pressure loss within a maximum deviation range of $\pm 5\%$. The CFD simulations showed that boundary layer separation occurs upstream of the welding spots, leading to large but flat-shaped recirculation zones, which occupy roughly 30% of the wall area. These zones are the main cause of form drag, which contributes approximately 50% of the Darcy friction factor.

The results of the numerical studies for the inner and outer pillow-plate channels were then accumulated for the development of new design equations for the determination of pressure loss and heat transfer coefficients describing turbulent forced convection in PPHE. The outer channel was studied based on one set of characteristic geometrical parameters only. Correspondingly, design correlations for this one geometry were developed, whereas for the inner channels more generic design equations were derived.

Two different design methods were developed in this thesis for the determination of heat transfer coefficients in the inner channels. The first is based on a Dittus-Boelter type power-law function for the Nusselt number. The second model is based on the characteristic flow pattern in pillow-plate channels, whereby this pattern is broken down into two simpler flows, which are then modeled separately. Both methods showed good agreement to the Nusselt numbers obtained by the CFD simulations.

The results of this thesis clearly show the potential of CFD methods to be used as virtual experiments for the development of accurate design methods for new heat exchangers, such as PPHE. Consequently, these methods can successfully be used in future work to deliver the remaining data required to obtain generic design methods for the outer channels of PPHE, thus providing engineers with the necessary tools for optimally designing and rating PPHE.

References

[1] https://www.destatis.de/DE/PresseService/Presse/Pressemitteilungen/2015/10/PD15_400_435.html. (Accessed: 2017-05-15).

[2] R. K. Shah and D. P. Sekulić. *Fundamentals of Heat Exchanger Design.* John Wiley and Sons, 2003.

[3] A. Michel and A. Kugi. Accurate low-order dynamic model of a compact plate heat exchanger. *Int. J. Heat Mass Transfer*, 61:323–331, 2013.

[4] M. Piper, J. M. Tran, and E. Y. Kenig. A CFD study of the thermo-hydraulic characteristics of pillow-plate heat exchangers. In *Proceedings of the ASME Summer Heat Transfer Conference, Washington DC, USA*, 2016.

[5] H. D. Baehr and K. Stephan. *Heat and Mass Transfer.* Springer-Verlag, 2011.

[6] P. A. Davidson. *Turbulence - An Introduction for Scientists and Engineers.* Oxford University Press, New York, 2004.

[7] H. Ferziger and M. Perić. *Numerische Strömungsmechanik.* Springer-Verlag, 2008.

[8] E. Laurien and H. Oertel. *Numerische Strömungsmechanik.* Vieweg + Teubner Verlag, 2011.

[9] J. M. Tran, M. Piper, and E. Y. Kenig. Experimental investigation of convective heat transfer and pressure drop in pillow plates under single-phase through-flow condition. *Chem. Ing. Tech.*, 87(3): 226–234, 2015.

[10] *VDI Wärmeatlas.* Springer Verlag, 10th edition, 2006.

[11] H.K. Versteeg and W. Malalasekera. *An Introduction to Computational Fluid Dynamics.* Pearson Education, 2007.

[12] L. H. Grenell. Sheet metal fabrications. *US-Patent US3053514A*, 1949.

[13] http://www.athco-engineering.dk/index.php/products/heat-exchangers/pillow-plates/. (Accessed: 2018-03-28).

[14] https://www.omegathermoproducts.nl/en/products-and-heat-exchangers/products/pillow-plate/. (Accessed: 2018-03-28).

[15] J. Mitrovic and R. Peterson. Vapor condensation heat transfer in a thermoplate heat exchanger. *Chem. Eng. Technol.*, 30(7):907–919, 2007.

[16] F. W. Dittus and L. M. K. Boelter. Heat transfer in automobile radiators of the tubular type. *Int. Comm. Heat Mass Transfer*, 12(1):3–22, 1985.

[17] J. Mitrovic and B. Maletic. Numerical simulation of fluid flow and heat transfer in thermoplates. *Chem. Eng. Technol.*, 34(9):1439–1448, 2011.

[18] B. Maletic. *Modelling and numerical analysis of fluid flow and heat transfer in thermoplates.* PhD thesis, University of Paderborn, 2009.

[19] H. Kuhlmann. *Strömungsmechanik.* Pearson Studium, 2007.

[20] H. Marschall. *Towards the Numerical Simualtion of Multi-Scale Two-Phase Flows.* PhD thesis, Technische Universität München, 2011.

[21] R. B. Bird, W. E. Stewart, and E. N. Lightfoot. *Transport Phenomena.* John Wiley and Sons, 2 edition, 2002.

[22] H. Schlichting and K. Gersten. *Boundary-Layer Theory.* Springer, 8 edition, 2000.

[23] B. Nusselt. Wärmeübergang in rohrleitung. *Forsch.-Arb. Ing.-Wes.*, (89), 1910.

[24] S. Kakac, R. K. Shah, and W. Aung. *Handbook of single-phase convective heat transfer.* John Wiley and Sons, 1987.

[25] H. Kraussold. Die Wärmeübertragung an Flüssigkeiten in Rohren bei turbulenter Strömung. *Forschung*, 4(1):39–44, 1933.

[26] F. Steimle. *Der allgemeine Zusammenhang zwischen Wärmeübergang und Druckabfall turbulenter Strömungen und seine Auswirkung auf die Formulierung von Funktionen der Nusselt-Zahl.* Verlag C. F. Müller Karlsruhe, 1970.

[27] S. W. Churchill. Progress in the thermal sciences: AIChE Institute Lecture. *AIChE J.*, 46: 1704–1722, 2000.

[28] B. S. Petukhov. *Turbulent heat transfer in tubes with variable fluid properties, In Heat exchangers: design and theory sourcebook, N. H. Afgan and E. U. Schlünder.* McGraw-Hill, 1974, pp. 239-263.

[29] V. Gnielinski. On heat transfer in tubes. *Int. J. Heat Mass Transfer*, 63:134–140, 2013.

[30] J. G. Knudsen and D. V. Katz. *Fluid Dynamics and Heat Transfer.* McGraw-Hill, New York, 1958.

[31] B. S. Petukhov and V. N. Popov. Theoretical calculation of heat exchange in turbulent flow in tubes of an incompressible fluid with variable physical properties. *High Temp.*, 1(1):69–83, 1963.

[32] M. Wolfshtein. The velocity and temperature distribution in one-dimensioal flow with turbulence augmentation and pressure gradient. *Int. J. Heat Mass Transfer*, 12(3):301–318, 1969.

[33] T. H. Shih, W. W. Liou, A. Shabbir, Z. Yang, and J. Zhu. A new $k-\epsilon$ eddy viscosity model for high Reynolds number turbulent flows. *Computers Fluids*, 24(3):227–238, 1995.

[34] F. Billard and D. Laurence. A robust $k-\varepsilon-v^2/k$ elliptic blending turbulence model with improved predictions in near-wall, separated and boyant flows. *Int. J. Heat Fluid Fl.*, 33(1):45–58, 2012.

[35] W. P. Jones and B. E. Launder. The prediction of laminarization with a two-equation model of turbulence. *Int. J. Heat Mass Transfer*, 15:301–314, 1972.

[36] P. A. Durbin. On the $k - \varepsilon$ stagnation point anomaly. *Int. J. Heat Fluid Flow*, 17:89–90, 1996.

[37] H. Reichardt. Vollständige Darstellung der Geschwindigkeitsverteilung in glatten Leitungen. *ZAMM*, 31:208–219, 1951.

[38] B. A. Kader. Temperature and concentration profiles in fully turbulent boundary layers. *Int. J. Heat Mass Transfer*, 24(9):1541–1544, 1981.

[39] V. C. Patel, W. Rodi, and G. Scheuerer. Turbulence models for near-wall and low reynolds number flows - a review. *AIAA Journal*, 23(9):1308–1319, 1985.

[40] P. A. Durbin. Near-wall turbulence closure modeling without damping functions. *Theoret. Comput. Fluid Dynamics*, 3:1–13, 1991.

[41] W. Rodi. Experience with two-layer models combining the $k - \epsilon$ model with one-equation model near the wall. *AIAA*, pages 91–216, 1991.

[42] F.S. Lien, W. L. Chen, and M. A. Leschziner. In *Proc. 3rd Symp. on Engineering Turbulence Modelling and Measurements*, 1996.

[43] H. C. Chen and V. C. Patel. Near-wall turbulence models for complex flows including separation. *AIAA Journal*, 26(6):641–648, 1988.

[44] E. R. Van Driest. On turbulent flow near a wall. *J. Aero. Sci.*, 23:1007–1011, 1956.

[45] T. Jongen. *Simulation and modeling of turbulent incompressible flows.* PhD thesis, Lausanne EPFL, 1998.

[46] *Star CCM+ Documentation*, release 10.02 edition, 2015.

[47] H. Jasak. *Error analysis and estimation for the finite volume method with application to fluid flows.* PhD thesis, Imperial College London, 1996.

[48] M. Piper, A. Olenberg, J. M. Tran, and E. Y. Kenig. Determination of the geometric design parameters of pillow-plate heat exchangers. *Appl. Therm. Eng*, 91(1):1168–1175, 2015.

[49] `http://www.3ds.com/products-services/simulia/portfolio/abaqus/overview/`. (Accessed: 2014-09-10).

[50] S. P. Timoshenko. *The Theory of Plates and Shells.* McGRAW-HILL, 1964.

[51] M. Piper, A. Zibart, J. M. Tran, and E. Y. Kenig. Numerical investigation of turbulent forced convection heat transfer and fluid flow in pillow plates. *Int. J. Heat Mass Transfer*, 94:516–527, 2016.

[52] J. M. Tran, S. Sommerfeld, M. Piper, and E. Y. Kenig. Investigation of pillow-plate condensers for the application in distillation columns. *Chem. Eng. Res. Des.*, 99:67–74, 2015.

[53] A. Lautenschleger, A. Olenberg, and E. Y. Kenig. A systematic CFD-based method to investigate and optimise novel structured packings. *Chem. Eng. Sci.*, 122:452–464, 2015.

[54] S. A. Owens, M. R. Perkins, and R. B. Eldridge. Computational fluid dynamics simulation of structured packings. *Ind. Eng. Chem. Res.*, 52:2032–2045, 2013.

[55] S. Jain, A. Joshi, and P. K. Bansal. A new approach to numerical simulation of small sized plate heat exchangers with chevron plates. *J. Heat Transfer*, 129:291–297, 2007.

[56] Q. Wang, Q. Chen, G. Chen, and M. Zeng. Numerical investigation on combined multiple shell-pass shell-and-tube heat exchanger with continuous helical baffles. *Int. J. Heat Mass Transfer*, 52:1214–1222, 2009.

[57] W. Kays, M. Crawford, and B. Weigand. *Convective Heat and Mass Transfer*. McGraw-Hill, 2005.

[58] M. Piper, A. Zibart, and E. Y. Kenig. New design equations for turbulent forced convection heat transfer and pressure loss in pillow-plate channels. *Int. J. Therm Sci*, 120:459–468, 2017.

[59] A. P. Colburn. A method for correlating forced convection heat transfer data and a comparison with fluid friction. *Int. J. Heat Mass Transfer*, 7(12):1359–1384, 1964.

[60] E. N. Sieder and G. E. Tate. Heat transfer and pressure drop of liquids in tubes. *Ind. Eng. Chem.*, 28(12):1429–1435, 1936.

[61] `https://www.nist.gov/srd/refprop`. (Accessed: 2016-02-01).